Thin-Metal-Film-Based Transparent Conductors: Material Preparation, Optical Design, and Device Applications

Cheng Zhang,* Chengang Ji, Yong-Bum Park, and L. Jay Guo*

Transparent conductors are essential elements in an array of optoelectronic devices. The most commonly used transparent conductor – indium tin oxide (ITO) suffers from issues including poor mechanical flexibility, rising cost, and the need for annealing to achieve high conductivity. Consequently, there has been intensive research effort in developing ITO-free transparent conductors over the recent years. This article gives a comprehensive review on the development of an important ITO-free transparent conductor, that is based on thin metal films. It starts with the background knowledge of material selection for thin-metal-film-based transparent conductors and then surveys various techniques to fabricate high-quality thin metal films. Then, it introduces the spectroscopic ellipsometry method for characterizing thin metal films with high accuracy, and discusses the optical design procedure for optimizing transmittance through thin-metal-film-based conductors. The review also summarizes diverse applications of thin-metal-film-based transparent conductors, ranging from solar cells and organic light emitting diodes, to optical spectrum filters, low-emissivity windows, and transparent electromagnetic interference coatings.

1. Introduction and Background

Transparent conductors are one of the essential elements in various optoelectronic devices such as solar cells, photodetectors, light emitting diodes, flat panel displays, touch screens, and smart windows.[1–3] An ideal transparent conductor is characterized by high visible transmittance, good electrical conductivity over large areas, low haze, and robust performance stability. Recently, with the emergence of new applications such as wearable electronics and bendable smartphones, the transparent conductors are also desired to be mechanically strong and flexible.

So far, the most widely used transparent conductor is indium tin oxide (ITO), which exhibits both high visible transmittance and low electrical resistance. Besides, ITO can be prepared using an array of deposition techniques including evaporation, sputtering, pulsed laser deposition, and solution processing.[4] However, ITO suffers from a well-known issue of poor mechanical flexibility and is prone to cracks under strain or bending,[5] which severely restricts its usage in flexible devices. In addition, to obtain high-quality ITO films with good optical transparency and low sheet resistance, many deposition techniques require a high deposition temperature or an additional postdeposition annealing treatment, which is unfortunately incompatible with flexible substrates. Moreover, there is concern about the rising cost and sustainability of ITO, as the indium element has limited supply on earth and is usually obtained as a byproduct during the extraction of other metals.[6,7]

While there are ongoing researches to improve the optoelectronic properties and mechanical flexibilities of ITO on flexible substrates by investigating the underlying mechanism,[8,9] adjusting its deposition procedure,[10–12] or exploiting hybrid structures incorporating ITO and other conductive materials,[13–18] more intensive research efforts have been devoted to developing flexible transparent conductors based on ITO-free materials, such as conductive polymers,[19–21] carbon-based materials,[22–25] patterned metal grids,[26–33] metal nanowires,[34–42] and thin metal films.[43–48] Though conductive polymers and carbon-based materials improve the mechanical flexibility of transparent conductors, their relatively low conductivity could limit the conductors' electrical performance.[21,25,49,50] Metal grids and nanowires offer advantages of high transmittance and low sheet resistance. However, light scattering by these structures can induce significant haze and they are usually fabricated through precise patterning or complicated chemical synthesis processes, which could constrain their usage in low-cost and large-scale device applications.[26,27,34,51] In comparison, thin metallic films exhibit unique advantages including excellent mechanical flexibility and simple fabrication procedure. Indeed, they can be deposited over large-area flexible substrates with minimum defect (thus low haze) and at a low cost, through a roll-to-roll manufacturing process. For more than a decade, there has been

Prof. C. Zhang
School of Optical and Electronic Information and Wuhan
National Laboratory for Optoelectronics
Huazhong University of Science and Technology
Wuhan, Hubei 430074, China
E-mail: cheng.zhang@hust.edu.cn
Dr. C. Ji,[+] Dr. Y.-B. Park, Prof. L. J. Guo
Department of Electrical Engineering and Computer Science
University of Michigan
Ann Arbor, MI 48109, USA
E-mail: guo@umich.edu

(iD) The ORCID identification number(s) for the author(s) of this article can be found under https://doi.org/10.1002/adom.202001298.

[+]Present address: Ningbo Inlight Technology Co., Ltd., Ningbo, Zhejiang 315500, China

active research effort in the community to constantly improve the optoelectronic performance (transmittance, conductivity, stability, etc.) of thin-metal-film-based transparent conductors by optimizing their structures and fabrication procedures, and to explore thin-metal-film-based transparent conductors' applications in diverse optoelectronic devices such as solar cells and light emitting diodes.

Here, we aim to systematically summarize the recent development of thin-metal-film-based transparent conductors in terms of material selection and preparation, optical structure design, as well as optoelectronic device applications. A few review articles on thin metal films can be found in the literature, with a large focus on thin film growth techniques and flexible device applications.[43,45] In this review, we choose to use a different strategy and will start from material selection for thin-film-based transparent conductors by considering the electrical resistivities and optical refractive indices of common metals, followed by surveys on various fabrication methods for high-quality thin metal films. We will then discuss the ellipsometry characterization technique for thin metal films, which is highly relevant to the topic here, but rarely covered by previous review articles. Afterward, we will give a brief tutorial on the optical design of thin-metal-film-based transparent conductors and demonstrate strategies to unlock the conductors' full potential by maximizing the optical transparency of a dielectric–metal–dielectric stack. Finally, we will discuss various applications of thin-film-based transparent conductors, which include both their typical applications in photovoltaic and light emitting devices, and emerging applications in see-through or colored solar panels, low-emissivity windows, electromagnetic shielding coatings, etc.

2. Material Selection for Thin-Metal-Film-Based Transparent Conductors

2.1. Electrical Resistivity

2.1.1. Electrical Resistivity of Bulk Metal

The electrical resistivity, ρ, of different metals are listed in **Table 1**.[52,53] Among them, silver (Ag), copper (Cu), and gold (Au) exhibit the lowest electrical resistivity, showing their good potential for conductor applications.

It is worth noting that the resistivity values listed in Table 1 are only valid for bulk metals or metal films with thicknesses of a few hundred nanometers. For a thin metal film, its resistivity is not only determined by the intrinsic property of the constituent metal, but also largely affected by other factors such as film thickness, surface morphology, defect density, etc. In the following section, we will introduce two classical resistivity scaling models to describe the behavior of electron transport inside thin metal films. Such models can be used as a theoretical baseline to estimate the sheet resistance as well as figure of merit (FoM) of a thin-metal-film-based transparent conductor.
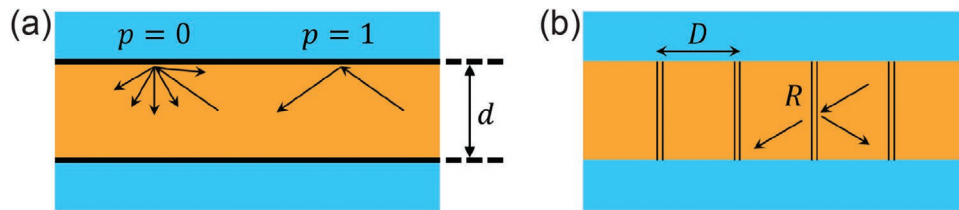
2.1.2. Electrical Resistivity of a Thin Metal Film

For a thick metal film, scattering of conduction electrons at its boundaries can be ignored as the metal thickness is usually much larger than the electron's mean free path. For example, the aforementioned mean free path values for Ag, Cu, and Au at room temperature are calculated to be ≈53, 39, and 38 nm, respectively.[54] By contrast, for a thin metal film, its boundaries are significantly closer with a distance comparable to or even smaller than the electron's mean free path, and therefore, scattering will play a significant role in affecting the film's resistivity. There are two major scattering processes inside a thin metal film: i) surface scattering (evidenced by the thickness dependence of the resistivity for a thin metal film) and ii) grain boundary scattering (evidenced by the grain size dependence of the resistivity for a thin metal film).

Surface Scattering: One widely accepted model for describing the scattering at the film surface is the Fuchs–Sondheimer (FS) model.[55,56] This model is based on the Boltzmann transport theory and attributes the increase of resistivity for a thin metal film to the diffusive scattering of conduction electrons at the film's surface. To describe such a surface scattering process, the specular scattering coefficient, p, is introduced (**Figure 1**a). Here $p = 0$ corresponds to a completely diffusive scattering process, while $p = 1$ corresponds to a specular scattering process. A conduction electron that is diffusely scattered loses the additional momentum it has gained from the external electric field and leaves the surface along a random direction, leading to an increase in the film's resistivity. By contrast, an electron that is specularly scattered does not change its momentum in the direction parallel to the film surface, and therefore, does not contribute to the increase in resistivity. Based on the FS model, the resistivity of a thin metal film is related to the bulk resistivity, ρ_i, as follows

$$\rho_{FS} = \rho_i \left[1 - \left(\frac{3}{2k}\right)(1-p) \int_1^\infty \left(\frac{1}{t^3} - \frac{1}{t^5}\right) \frac{1 - \exp(-kt)}{1 - p \cdot \exp(-kt)} dt \right]^{-1} \quad (1)$$

where $k = d/l_0$. Here, d is the film thickness and l_0 is the electron's mean free path. The parameter k incorporates the thickness dependence of resistivity into the FS model, and "normalizes" the film thickness with respect to the electron mean free path. The specular scattering coefficient, p, takes

Table 1. Electrical resistivity (ρ) at 20 °C for various metals[52,53].

Material	Resistivity, ρ [Ω m] at 20 °C
Silver (Ag)	1.59×10^{-8}
Copper (Cu)	1.70×10^{-8}
Gold (Au)	2.44×10^{-8}
Aluminum (Al)	2.82×10^{-8}
Tungsten (W)	5.60×10^{-8}
Nickel (Ni)	6.99×10^{-8}
Iron (Fe)	1.00×10^{-7}
Platinum (Pt)	1.10×10^{-7}
Chromium (Cr)	1.25×10^{-7}
Titanium (Ti)	4.20×10^{-7}

ADVANCED
SCIENCE NEWS
www.advancedsciencenews.com

ADVANCED
OPTICAL
MATERIALS
www.advopticalmat.de

Figure 1. Schematic representation of a) the surface scattering process described by the FS model and b) the grain boundary scattering process described by the MS model. (The figure is plotted based on figures 2.5 and 2.6 of ref. [61].)

values between 0 and 1, and can be used as a parameter to fit the experimental data. It is worth noting that the FS model does not explicitly include the surface roughness value of a thin film. To overcome this limitation, researchers have tried to incorporate surface roughness values into the specular scattering coefficient so that p is not a purely fitting parameter to fit the empirical data, but can be calculated based on the roughness value of a scattering surface.[57–60]

Grain Boundary Scattering: One widely used model for describing the scattering at the grain boundaries inside a thin metal film is the Mayadas–Shatzkes (MS) model.[62] This model is an extension of the Boltzmann transport theory, and includes the effect of collision between conduction electrons and the grain boundaries inside a polycrystalline metal film. The MS model assumes that only the grain boundaries perpendicular to the surface direction will collide with the conduction electrons, leading to an increase in the resistivity. These perpendicular grain boundaries are treated as potential barriers using the Dirac delta function where electrons get scattered during their transportation through these boundaries.[63] Such a scattering process is described by the reflection coefficient, R, whose value ranges from 0 to 1 (Figure 1b). R can be treated as a varying parameter to fit the experimental data, where $R = 0$ corresponds to the case where an electron completely transmits through the grain boundary (causing no increase in resistivity), while $R = 1$ corresponds to the case where an electron is completed reflected back by the grain boundary (resulting in an increase in the resistivity). Based on the MS model, the resistivity of a thin metal film is related to the bulk resistivity, ρ_i, as follows

$$\begin{cases} \rho_{MS} = \rho_i \left[1 - \frac{3}{2}\alpha + 3\alpha^2 - 3\alpha^3 \ln\left(1+\frac{1}{\alpha}\right) \right]^{-1} \\ \alpha = \frac{l_0}{D}\frac{R}{1-R} \end{cases} \quad (2)$$

where l_0 is the electron's mean free path and D is the grain size. The effects of grain size, grain boundary scattering, and electron's mean free path are conveniently incorporated into the parameter α.

2.2. Optical Transmittance

Consider a general scenario where a light beam of free-space wavelength, λ_0, passes through a thin metal film of thickness d, and complex refractive index $n_{metal}(\lambda_0) = n(\lambda_0) + ik(\lambda_0)$. For the ease of description, the film is located in a Cartesian coordinate system where the bottom surface of the film is in the
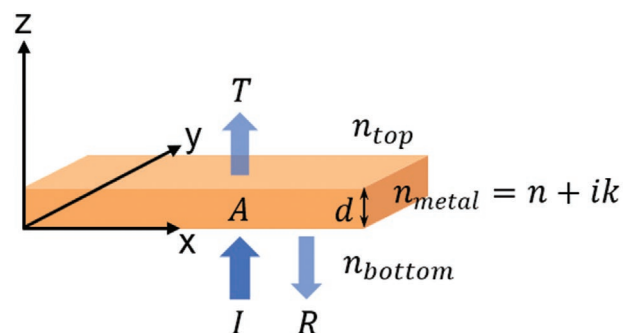
$z = 0$ plane (**Figure 2**). The complex refractive indices of the media atop and beneath the metal film are n_{top} and n_{bottom}, respectively. Light is normally incident onto the film along the $+z$-direction. The absorbed light intensity by this thin metal film, A, can be expressed as

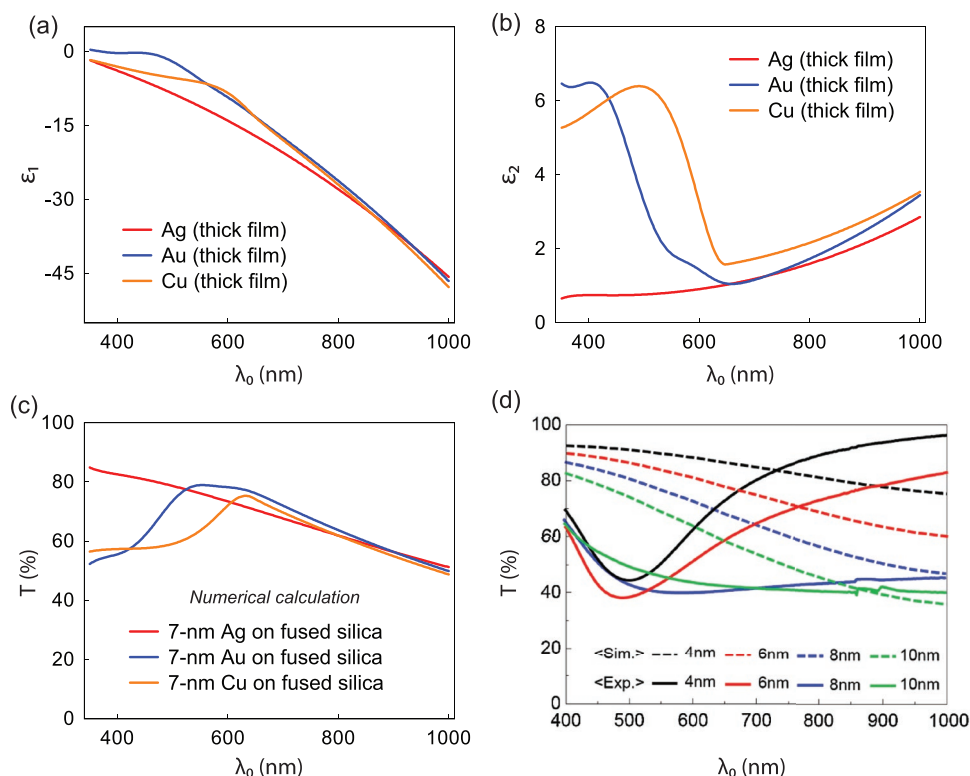$$A = \frac{4\pi nk}{\lambda_0} \int_0^d \left(|E(z)|\right)^2 dz \quad (3)$$

where $E(z)$ is the electric field inside the metal film at position z. According to Equation (3), a few strategies can be utilized to reduce the optical absorption by a thin metal film and enhance its transmittance, which include: i) choosing a metal with a low product of $n \cdot k$; ii) employing a metal film as thin as possible; iii) reducing the magnitude of electric field inside the metal film. Moreover, the intensity of transmitted light, T, is closely related with the intensity of incident light, I, the intensity of reflection light, R, and the intensity of absorbed light, A. In other words, $T = I - R - A$. This leads to the 4th strategy: iv) suppressing the reflection from a thin metal film (or a thin-metal-film-based structure).

We will now examine the 1st strategy: choosing a metal with a low product of nk. The complex relative permittivity of a material, $\varepsilon_{metal} = \varepsilon_1 + i\varepsilon_2$, is related to its complex refractive index as

$$\begin{cases} \varepsilon_1 = n^2 - k^2 \\ \varepsilon_2 = 2nk \end{cases} \quad (4)$$

Figure 2. Schematic illustration of a thin metal film with a complex refractive index $n_{metal} = n + ik$. The film is located in a Cartesian coordinate system in which the bottom surface of the film is in the $z = 0$ plane. The complex refractive indices of media on top of and beneath the film are n_{top} and n_{bottom}, respectively. Incident light of intensity I propagates along the $+z$-direction. The intensities of transmitted light, reflected light, and absorbed light are T, R, and A, respectively.

ADVANCED
SCIENCE NEWS
www.advancedsciencenews.com

ADVANCED
OPTICAL
MATERIALS
www.advopticalmat.de

Figure 3. a,b) Real (a) and imaginary (b) part of the relative permittivity of thick Ag, Au, and Cu films.[70] c) Calculated transmission spectra through 7 nm thick Ag, Au, and Cu films on fused silica substrates. The associated relative permittivity values used in the calculation are based on those of the thick films from (a, b). d) Total transmittance of the glass/Ag films as a function of Ag thickness (dotted line: simulation, solid line: experimental results). Adapted with permission.[71] Copyright 2015, Society of Photo-Optical Instrumentation Engineers (SPIE).

According to Equation (4), the 1st strategy now suggests employing a metal with a low ε_2 in the wavelength range of interest. The real and imaginary parts of the complex relative permittivity, ε_1 and ε_2, of thick Ag, Cu, and Au[70] are plotted in **Figure 3**a,b, respectively. Among them, Ag exhibits the lowest ε_2 across the visible and near-infrared (near-IR) region. Indeed, because Ag has the lowest electrical resistivity among all metals, and at the same time, best optical properties in the visible and near-IR spectral range (Figure 3c), it is therefore the most widely employed material for thin-metal-film-based transparent conductors. Compared to Ag, Au and Cu exhibit a similar electrical resistivity and moderate optical properties in the visible and near-IR regimes, while at the same time, have advantages over Ag in terms of environmental stability or lower material cost.[64] Consequently, there are also studies on Au-film- or Cu-film-based transparent conductors. Finally, it is worth noting that Al and Ni are also exploited for transparent conductor applications in some cases.[65–67] Although their conductivity and optical transparency are not as great as those of the aforementioned metals, they exhibit a low percolation threshold (good for ultrathin film formation)[68] and great stability (especially after an oxide protection layer is formed over the film surface).[69]

Based on the 2nd strategy, the thinner the metal film, the higher its optical transmittance. This is illustrated in Figure 3d, where the optical transmittance through a thin layer of Ag (deposited on glass substrate) of different thicknesses is numerically calculated.[71] The films are treated as perfectly smooth layers and the refractive indices of Ag at different film thicknesses are assumed to be identical. As the film thickness reduces from 10 to 4 nm, there is a continuous increase in the overall transmittance over the visible and near-IR range (400–1000 nm). In addition, the authors have also experimentally measured the transmittance through Ag films with associated thicknesses, but observed dramatically different results (which will be explained below). On one hand, there is no longer a monotonical improvement in the overall transmittance in the wavelength range of study as the film thickness reduces. On the other hand, transmission dips appear in the measured spectra, which are not predicted by the numerical calculation.

Several factors contribute to the significant discrepancy between the calculated and measured transmittance. Thin metal films (e.g., thickness < 20 nm) are usually characterized by a higher density of defects and less-than-ideal surface morphology with large surface roughness. This leads to its higher optical loss and lower electrical conductivity compared to a thick film. As the film thickness goes down, its optical loss and electrical resistivity usually increase. When the thickness further gets reduced (e.g., <10 nm), the metal film can be discontinuous and nonconductive. The resultant isolated metallic islands absorb light of specific frequencies due to the induced localized surface plasmon

ADVANCED
SCIENCE NEWS
www.advancedsciencenews.com

ADVANCED
OPTICAL
MATERIALS
www.advopticalmat.de

resonances (LSPRs), leading to the dips in the measured spectra shown in Figure 3d. Therefore, although the 2nd strategy suggests using a metal film as thin as possible, cautions need to be taken to make sure that the film's optical property, surface morphology, and electrical conductivity are not compromised as the film thickness reduces. Various methods have been developed to fabricate high-quality ultrathin metal films with smooth surface morphologies and good optoelectronic properties, and we will discuss these methods in Section 3.

The 3rd and 4th strategies are usually implemented by proper optical design of transparent conductors. One common method is to adjust the refractive indices of optical media surrounding the thin metal film (e.g., n_{top} and n_{bottom} shown in Figure 2), which could either affect the electric field distribution inside the metal film, or reduce the optical reflection from the whole structure. The media beneath and on top of the metal film can be a single-layered material, multiple-layered materials, or materials with graded indices. We will give a detailed discussion on this aspect in Section 5.

2.3. Figure of Merit

The main criteria to select a thin metal film for transparent conductor applications are the material's electrical resistivity and optical transparency (over the visible and near-infrared regimes for most applications). In a majority of cases, the transparent conductors are desired to have an electrical resistance as low as possible, and at the same time, an optical transmittance as high as possible. However, the electrical resistance and optical transmittance of a thin metal film are usually interrelated to each other, which unfortunately excludes the possibility of obtaining maximized transmittance and conductivity simultaneously. To evaluate the performance of a transparent conductor, two different FoMs have been suggested.

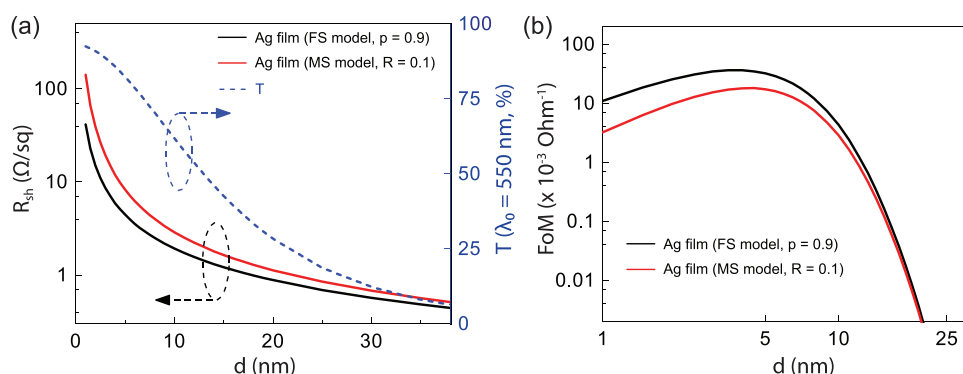Fraser and Cook defined the FoM as[72]

$$\text{FoM} = \frac{T}{R_{sh}} \tag{5}$$

Here, T is the optical transmittance (either a value for a single wavelength or an averaged value over a certain wavelength range), and R_{sh} is the sheet resistance. Haacke later on suggested another way of defining the FoM[73]
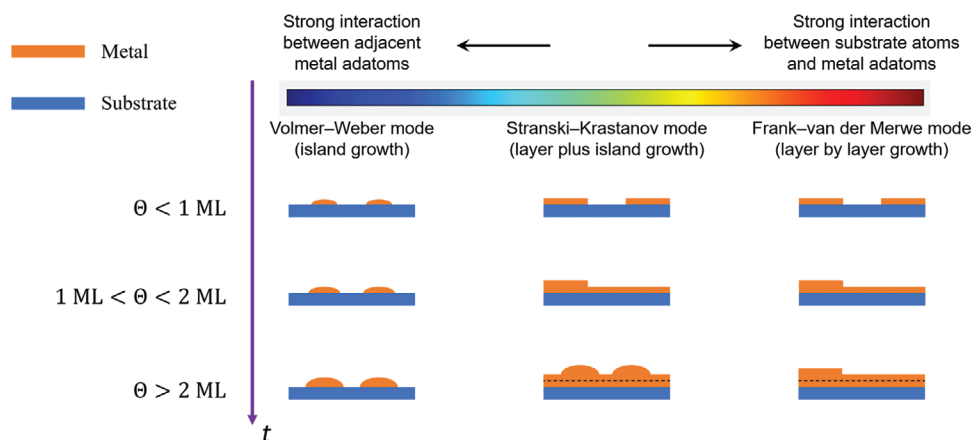
$$\text{FoM} = \frac{T^{10}}{R_{sh}} \tag{6}$$

where T and R_{sh} have the same meaning as those in Fraser and Cook's definition. Haacke's FoM gives more weight over the conductor's optical transmittance and has been widely used in recent studies of transparent conductors.

Here, we show how theoretical resistivity models can be used to calculate FoMs. As shown in **Figure 4**, we plot the theoretical sheet resistance and Haacke's FoM values calculated for Ag films (of different thickness values) considering either the FS or MS model with fitting parameters of close-to-ideal values. Hypothetically, if one can obtain epitaxial Ag films which are free of grain boundary scattering and with minimal diffusive surface scattering, such films can be modeled via the FS model (roughly assuming $p \approx 0.9$). Similarly, if the Ag films only consist of grain boundary scattering with minimal reflections at grain boundaries, they can be modeled via the MS model (roughly assuming $R \approx 0.1$).

Figure 4 shows the thickness-dependent sheet resistance, optical transmittance (at $\lambda_0 = 550$ nm), and FoM values for the aforementioned close-to-ideal thin Ag films. The sheet resistance values are calculated based on either the FS or MS model, and the optical transmittance values are calculated using the "Johnson Christy" Ag refractive indices.[74] For simplicity, the refractive index is assumed to be identical when the film thickness changes. Although such analysis might be oversimplified, it still provides important indications. As the film thickness increases, both the optical transmittance and the electrical resistance quickly drop down. The highest FoM is obtained when the film thickness is around 5 nm. This suggests that obtaining ultrathin (<10 nm) metal films with low defect density is essential for maximizing the performance of transparent conductors. In the following section, we will discuss different ways to prepare high-quality ultrathin metal films.

Figure 4. a) Left axis: calculated sheet resistance (R_{sh}) as a function of the Ag film thickness based on the FS or MS model assuming $p = 0.9$ and $R = 0.1$, respectively. Right axis: calculated optical transmittance at 550 nm as a function of the Ag film thickness. b) Calculated Haacke's FoM for a Ag-film-based transparent conductor as a function of the Ag layer thickness.

ADVANCED
SCIENCE NEWS
www.advancedsciencenews.com

ADVANCED
OPTICAL
MATERIALS
www.advopticalmat.de

Figure 5. Schematic illustration of the initial states of metal film growth over a substrate. Θ is the substrate surface coverage in number of monolayer (ML). (This figure is plotted based on figure 4 of ref. [75].)

3. Fabrication of High-Quality, Ultrathin Metal Films

3.1. Kinetics of Thin Metal Film Growth

Metal film growth on a substrate generally follows several stages in a sequence, namely nucleation, coalescence, and thickness growth.[75] Fabricating metal films by physical vapor deposition (e.g., thermal/e-beam evaporation, sputtering) starts with a heterogeneous nucleation, i.e., the condensation of adatoms (atoms that lie on a crystal surface) onto a substrate that is composed of atoms which are different from those in the physical vapor phase. The condition and structure of the substrate surface, as well as various parameters during the deposition process (e.g., vacuum condition, deposition rate, residual gases, etc.) will affect the properties of the deposited metal films.

Depending on the strength of surface energy of the substrate (γ_s), surface energy of the metal (γ_m), and metal/substrate interface energy ($\gamma_{m/s}$), one of the following three nucleation modes can occur (**Figure 5**). They are i) Frank–van der Merwe mode (layer by layer growth): layers of material grow on top of one another. Interaction between adjacent substrate atoms and metal adatoms is stronger than that between adjacent metal adatoms. ii) Volmer–Weber mode (island growth): isolated 3D metallic islands form on the substrate. Interaction between adjacent metal adatoms is stronger than that between metal adatoms and substrate atoms. iii) Stranski–Krastanov mode (layer plus island growth): one or two monolayers of material form first, followed by individual islands on top. This is a situation between i) and ii), and involves a change of interaction energies between these atoms.

Consider the case of Volmer–Weber growth mode where isolated metallic islands are formed on the substrate. Contact angle of a liquid nucleus on a substrate, φ, is related to the surface energy of the substrate (γ_s), the surface energy of the metal (γ_m), and the metal/substrate interface energy ($\gamma_{m/s}$) by the Young's equation (Equation (7) and **Figure 6**).[75]
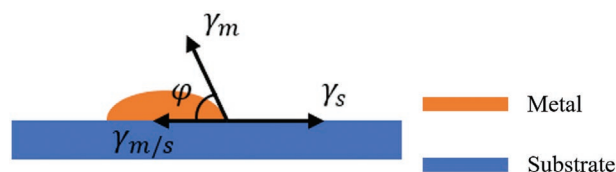
$$\gamma_s = \gamma_{m/s} + \gamma_m \cos \varphi \qquad (7)$$

For the Frank–van der Merwe mode (layer by layer growth), the contact angle equals 0° and the metal fully wets the substrate. This requires that $\gamma_s \geq \gamma_{m/s} + \gamma_m$. Under this mode, a continuous metal film is formed whose thickness is simply related to the volume of the deposited metal. On the contrary, under the Volmer–Weber mode (island growth), $\varphi > 0$. This indicates that $\gamma_s < \gamma_{m/s} + \gamma_m$. The adhesion energy, E_{adh}, is defined as the energy to separate the metal/substrate interface in vacuum. It is given by[76]

$$E_{adh} = \gamma_m + \gamma_s - \gamma_{m/s} \qquad (8)$$

Based on Equation (8), when $E_{adh} < 2\gamma_m$, the Volmer–Weber mode dominates the initial stages of metal film growth. Consequently, the metal will not wet on the substrate. In other words, because the metal atoms adhere weakly with the substrate (low E_{adh}), they instead exhibit a larger tendency to cluster with each other and form metallic islands.

Adhesion energies have been measured using the contact angle method for liquid metals on various substrates.[77] **Table 2** lists the values of E_{adh}, γ_s, and γ_m of different liquid metals on SiO_2 substrate.[78,79] Although these values are measured in the case of liquid metals, they provide a good estimation for the case of solid metals.[77] It can be seen that metals that are good candidates for transparent conductors (e.g., Ag, Au, and Cu) all have $E_{adh} < 2\gamma_m$. Consequently, the growth of these metal films typically follows the Volmer–Weber mode and isolated metallic islands, instead of continuous metallic

Figure 6. Contact angle of a liquid nucleus on a substrate, φ, is related to the surface energy of the substrate (γ_s), the surface energy of the metal (γ_m), and the metal/substrate interface energy ($\gamma_{m/s}$) by the Young's equation. (This figure is plotted based on figure 5 of ref. [75].)

Table 2. The adhesion energy on oxide substrate (E_{adh}) and the surface energy (γ_m) of different liquid metals, as well as the surface energy of the oxide substrate (γ_s).[78,79]

Material	E_{adh} [mJ m^{-2}]	γ_m [mJ m^{-2}]	γ_s [mJ m^{-2}]
Silver (Ag)	174	814–926	
Copper (Cu)	474	1233	
Gold (Au)	227–246	1125	307–605
Aluminum (Al)	844	844	
Nickel (Ni)	803–942	1883	
Iron (Fe)	913	1673	

layers, are formed on the substrate in the early stage of film growth. As the deposition continues, these islands extend and eventually connect with each other, forming a conductive network for the electrons (coalescence process). Such a transition from isolated islands to a continuous macroscopic network can be characterized by a percolation threshold thickness, which is typically 10–20 nm.

Beyond the percolation threshold, the metal film exhibits significantly improved electrical conductivity and reduced optical loss. However, transmittance through the film is inevitably sacrificed primarily due to the high optical reflection by the thick metal, making it unsuitable for transparent conductor applications. Therefore, it is crucial to modify the kinetics of metal film growth and suppress the Volmer–Weber growth mode, such that the percolation threshold is reduced, and continuous metal films are obtained with ultrathin thicknesses and good optoelectronic properties. We will discuss several methods for fabricating high-quality, ultrathin metal films in the subsequent section.

3.2. Approaches for Preparing High-Quality, Ultrathin Metal Films

In order to obtain high-quality ultrathin metal films with smooth surface morphology and good optoelectronic property, we need to inhibit their intrinsic Volmer–Weber growth mode and reduce the associated percolation threshold. Toward this goal, researchers have explored an array of techniques. In the subsequent sections, we will discuss these strategies categorized as follows: dielectric wetting layer, metal wetting layer, metal doping, molecular surfactant, and polymer surfactant. In addition, we will also discuss the impact of deposition conditions on the growth of ultrathin metal films.
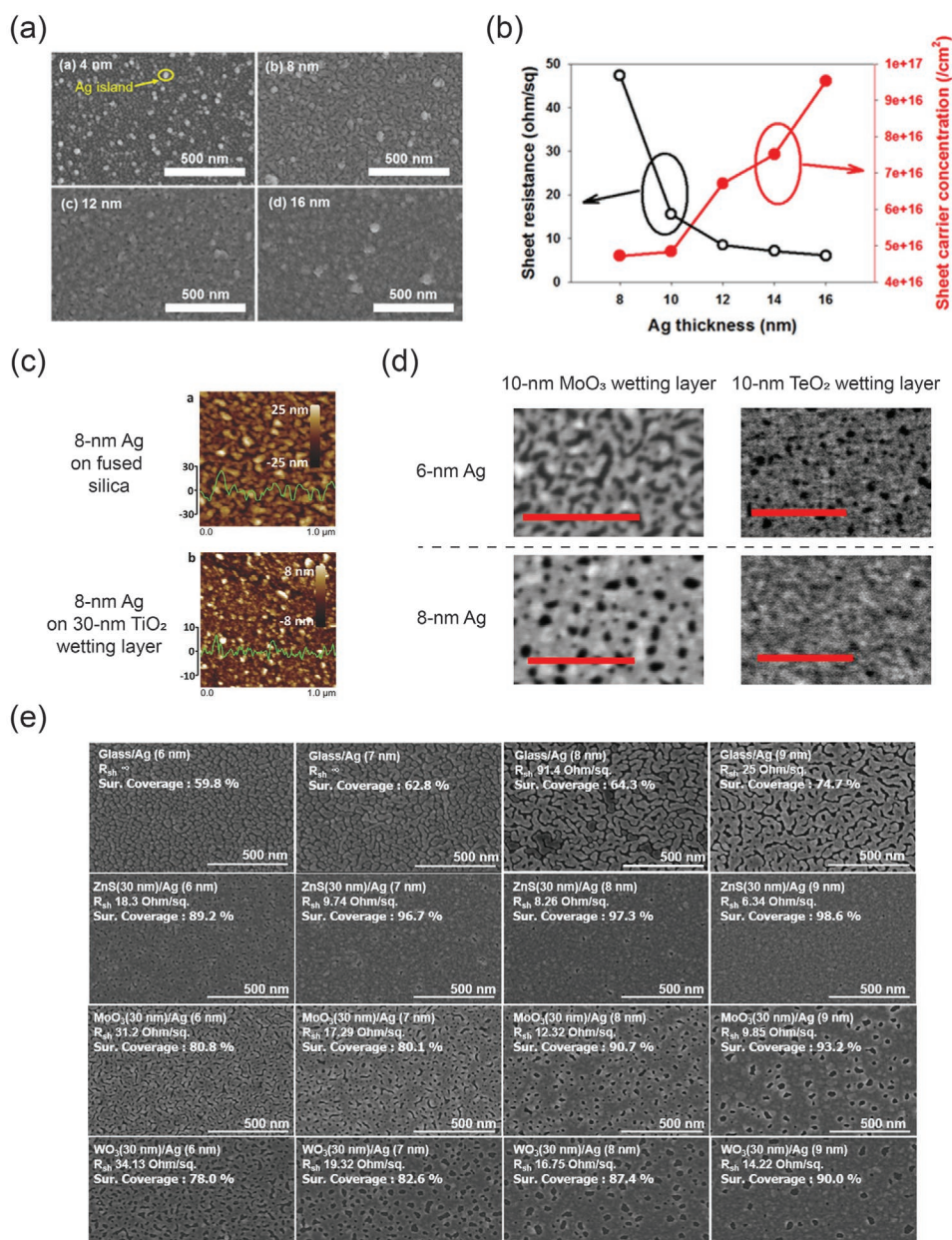
3.2.1. Dielectric Wetting Layer

As discussed in Section 3.1, the weak adhesion of metal adatoms with common transparent substrates (e.g., SiO$_2$) leads to the island film growth. Therefore, it is both straightforward and reasonable to consider that when a layer of dielectric material (which is also transparent) is deposited onto

the substrate first, the subsequently deposited metal atoms might have a better adhesion with the dielectric layer, and the metal's island growth mode is suppressed. Although in many cases, the surface energy of the candidate metal (γ_m) could still be larger than the metal/dielectric adhesion energy (E_{adh}), and therefore, a complete wetting (when $E_{adh} > 2\gamma_m$) will not occur, employing a layer of dielectric will still contribute to an increase in E_{adh} and alleviate the intrinsic island growth mode.

Various dielectric films (most of which are oxide films), that are transparent in the visible and near-IR range, have been experimentally demonstrated for promoting ultrathin metal film growth. Examples include zinc oxide (ZnO),[80–82] metal-doped ZnO (e.g., Al-doped ZnO,[83–85] In-doped ZnO,[86,87] Mg-doped ZnO,[88] Ga-doped ZnO,[89] etc.), titanium dioxide (TiO$_2$),[90–93] tungsten trioxide (WO$_3$),[94] indium tin oxide (ITO),[18] molybdenum trioxide (MoO$_3$),[95–98] niobium pentoxide (Nb$_2$O$_5$),[99] tellurium dioxide (TeO$_2$),[100,101] zinc sulfide (ZnS),[102–104] and aluminum nitride (AlN).[105] ZnO has been a popular oxide wetting layer by its high optical transparency in the visible and near-IR regime, as well as good electrical conductivity (especially when doped with another metal element). Lee et al. studied the surface morphology of Ag layers (with thickness varying from 4 to 16 nm) deposited on a 50 nm thick Mg-doped ZnO (Mg$_{0.28}$Zn$_{0.72}$O) layer (**Figure 7**a).[88] As the Ag layer thickness increases from 4 to 16 nm, the film evolves from an isolated-island one (4 nm) to a percolated film with certain surface defects (8 and 12 nm), and finally, to a continuous and smooth film (16 nm). At the same time, the sheet resistance of the entire electrode (50 nm thick Mg$_{0.28}$Zn$_{0.72}$O/Ag of varying thicknesses/50 nm thick Mg$_{0.28}$Zn$_{0.72}$O) goes down as the Ag film gets thicker (Figure 7b). TiO$_2$ is also a popular candidate for wetting layers by its lossless nature in the visible and near-IR range. Moreover, its high refractive index ($n > 2.0$ over the visible range) makes it a favorable material for electrode using the dielectric–metal–dielectric (DMD) structure (we will discuss this aspect in detail in Section 5). Ghosh et al. showed that an 8 nm thick Ag film on fused silica substrate exhibits a discontinuous and island-like surface morphology with a large root-mean-square (RMS) roughness of 6.5 nm (Figure 7c, top panel). With the help of a 30 nm thick TiO$_2$ wetting layer, the 8 nm thick Ag film is instead continuous and exhibits a significantly improved surface morphology with a RMS roughness of 2.2 nm (Figure 7c, bottom panel).[91]

There are studies on the wetting effect of different dielectric films.[88,100,103,106] Barrows et al. observed a reduced percolation threshold for Ag films deposited on a TeO$_2$ layer than on a MoO$_3$ layer (Figure 7d).[100] Kim and co-workers investigated the surface morphology of Ag films on different types of substrates (Figure 7e), including bare glass and glasses coated with dielectric wetting layers (ZnS, MoO$_3$, and WO$_3$).[103] On one hand, Ag films deposited on all these wetting layers exhibit improved surface morphology and reduced percolation threshold compared to film deposited on bare glass. On the other hand, Ag film on the ZnS layer shows the best surface morphology and the lowest electrical resistance at a given film thickness. The authors believe that the different wetting strength is due to the difference in the surface energy of
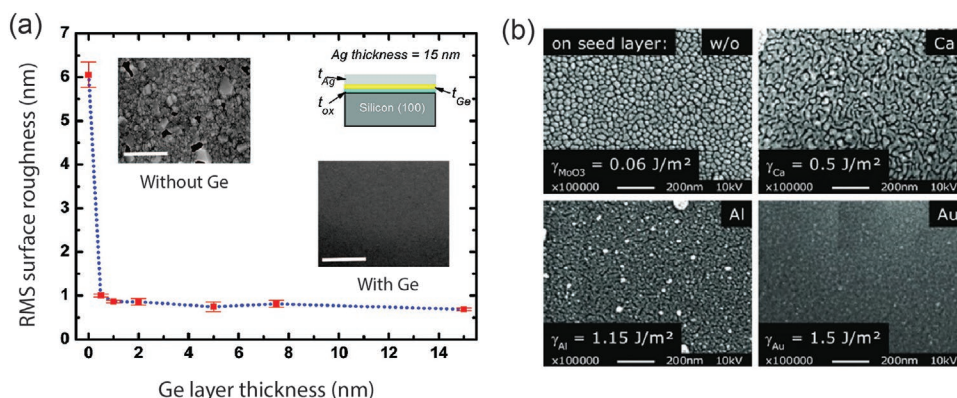
Figure 7. a) Scanning electron microscopy (SEM) images of (a) 4, (b) 8, (c) 12, and (d) 16 nm thick Ag layers on the $Mg_{0.28}Zn_{0.72}O$ wetting layer. b) Sheet resistance and sheet carrier concentration of the $Mg_{0.28}Zn_{0.72}O$ (50 nm)/Ag/$Mg_{0.28}Zn_{0.72}O$ (50 nm) multilayers. The Ag layers have different thicknesses varying from 8 to 16 nm. The conductivity of the multiplayer structure is provided dominantly by the sandwiched Ag layer. Reproduced with permission.[88] Copyright 2016, American Chemical Society. c) Atomic force microscopy (AFM) images and typical cross-section profiles of an 8 nm thick Ag film on fused silica substrate (top panel), and an 8 nm thick Ag film on a 30 nm thick TiO_2 wetting layer (bottom panel). In contrast to the discontinuous and rough morphology of Ag film on fused silica, the Ag film on TiO_2 is instead continuous and exhibits a much smoother surface morphology. Adapted with permission.[91] Copyright 2015, Wiley-VCH. d) SEM images of 6 nm thick (top panel) and 8 nm thick (bottom panel) Ag films on a 10 nm thick MoO_3 (left panel) and TeO_2 (right panel) wetting layer. There is a reduced percolation threshold and improved surface morphology for Ag films deposited on a TeO_2 layer than on a MoO_3 layer. The scale bar is 200 nm. Adapted with permission.[100] Copyright 2016, Elsevier. e) SEMs of Ag films (of varying thicknesses) deposited on bare glass and glasses coated with dielectric wetting layers (ZnS, MoO_3, and WO_3). The Ag film on the ZnS layer shows the best surface morphology and the lowest electrical resistance at a given film thickness. The deposition rate of Ag is kept at 0.2 nm s^{-1}. Reproduced with permission.[103] Copyright 2015, Wiley-VCH.

the oxide layers. ZnS has the highest surface energy among all three dielectric films, which effectively inhibits the surface diffusion of Ag atoms and suppresses their 3D island-like growth. Note that although these comparative studies

provide a good guideline for researchers to choose dielectric wetting layers, the conclusion cannot be simply taken for granted. The deposition process of the dielectric and metal layers is affected by various factors, which could influence

**ADVANCED
SCIENCE NEWS**

www.advancedsciencenews.com

**ADVANCED
OPTICAL
MATERIALS**

www.advopticalmat.de

Figure 8. a) Measured averaged RMS surface roughness as a function of Ge wetting layer thickness. The Ag thickness is kept at 15 nm. Insets are SEM images of Ag films with and without the Ge wetting layers. Adapted with permission.[107] Copyright 2008, American Chemical Society. b) SEM images of 7 nm thick Ag films deposited over MoO_3 layers coated without any wetting layer and with wetting metals of different surface energies (γ). Adapted with permission.[117] Copyright 2013, Wiley-VCH.

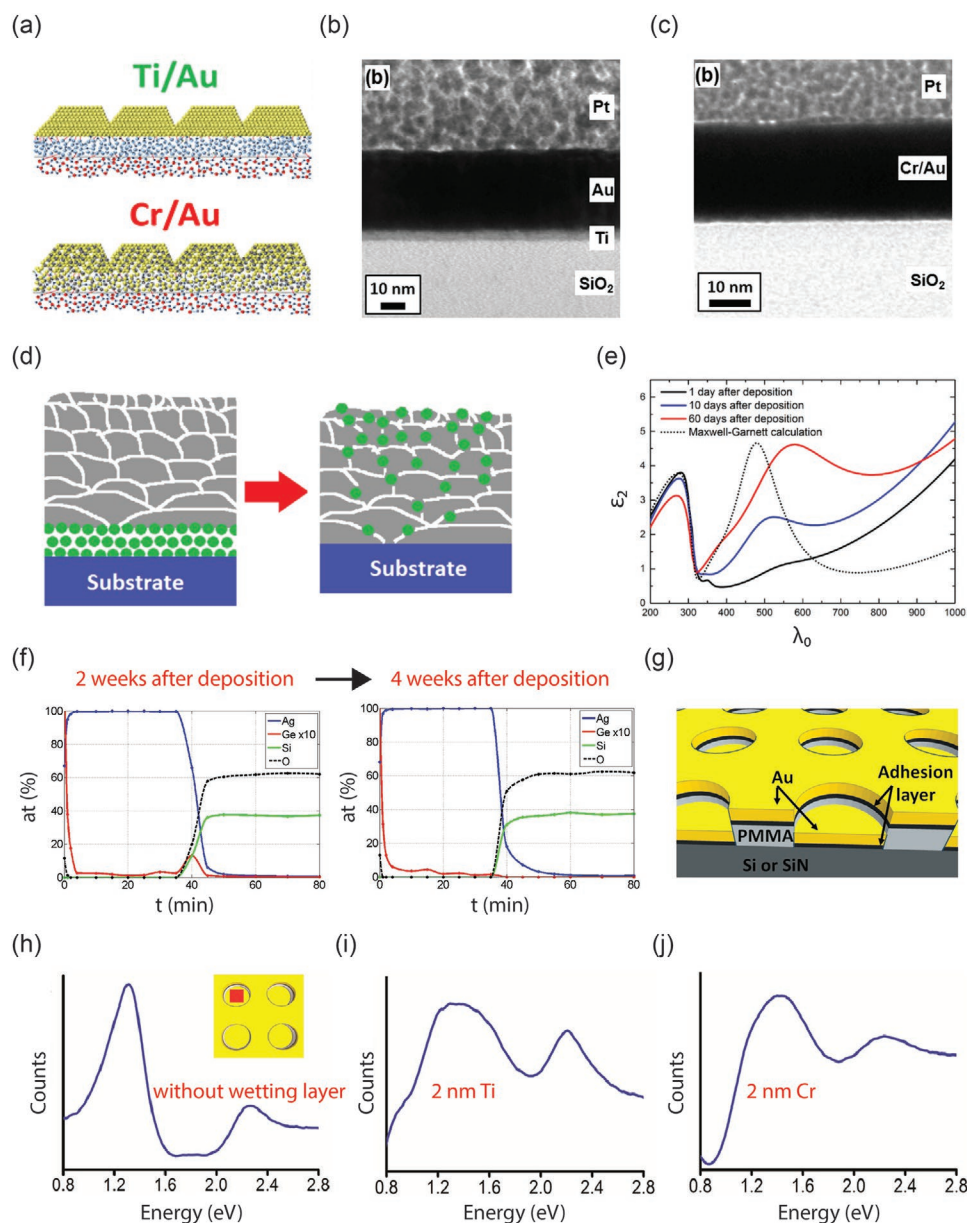their physicochemical properties and lead to the different wetting behaviors between them.

3.2.2. Metal Wetting Layer

Similar to the "dielectric wetting layer" approach, putting a thin metal layer on the substrate prior to depositing the candidate metal has been reported to provide benefits such as improving the morphology of the candidate metal film, reducing the percolation threshold for continuous film formation, as well as enhancing the adhesion of the metal film to the substrate. Commonly employed wetting metals for thin Ag films include Ge,[107–110] Ni,[111,112] Cr,[113,114] Ti,[112] Al,[115,116] Au,[117,118] Cu,[119] and Ca.[117] Popular metals used for wetting thin Au films include Ti,[120,121] Nb,[122] Cr,[123] and Al.[115] It is worth noting that thin Ti and Cr layers are also commonly used as adhesion layers to enhance the adhesion of Au or Ag films (or nanostructures) with the substrate.

Logeeswaran et al. explored the effect of Ge wetting layers on the morphology of thin Ag films (with a nominal thickness between 10 and 20 nm) on a SiO_2/Si substrate (Si substrate with an $\approx$2–4 nm thick native oxide layer).[107] **Figure 8**a plots the averaged RMS surface roughness of a 15 nm thick Ag films deposited on the SiO_2/Si substrates with Ge layers of different thicknesses. A significant reduction of the film's RMS roughness is observed when the thickness of Ge layer increases from 0 to 0.5 nm. Then, the roughness values quickly saturate at $\approx$0.6 nm as the thickness of Ge layer continues to increase. The insetted scanning electron microscopy (SEM) images show obvious surface morphology differences between Ag films with and without the Ge wetting layer. The wetting effect of Ge can be understood from its relative high surface energy than that of SiO_2. Representative surface energy values of Ag, Ge, and SiO_2 are 814–926, 1320–1710, and 307–605 mJ m^{-2}, respectively.[124] Adding a thin layer of Ge on top of SiO_2 increases the "overall" surface energy of the substrate (γ_s), and therefore, provides a favorable nucleation surface for the Ag adatoms. This strategy can be effective even though the deposited Ge layer

is still in the form of isolated islands (such as for a Ge wetting layer of only 0.5 nm thickness). Similar phenomena were observed in a study where Schubert et al. characterized the surface morphology of 7 nm thick Ag films deposited over MoO_3 layers coated with wetting metals of different surface energies (Ca, Al, and Au).[117] As the surface energy of the metal wetting layer increases, the surface morphology of the thin silver film improves correspondingly (Figure 8b). It is worth noting that although employing a metal with high surface energy as the wetting layer serves as a useful empirical guideline for preparing ultrathin metal films, this conclusion cannot simply be taken for granted. Reported surface energy values of metals vary among literature, and direct measurement of these values can be challenging. Also, various factors (e.g., substrate type, deposition rate, chamber pressure, etc.) would influence the degree of surface coverage as well as the surface morphology of the wetting metal layer, thus affecting the physicochemical properties of subsequently deposited candidate metal films.

One issue of the metal wetting layer approach is the diffusion and segregation of wetting metal into the candidate metal film, affecting both its optical and electrical properties. Todeschini et al. studied the diffusion characteristics of Ti and Cr wetting layers into thin Au films.[125] They found that Ti forms a uniform layer underneath the Au overlayer, while Cr interdiffuses into the Au overlayer and forms a thin Cr–Au alloy layer (**Figure 9**a). Under high-resolution transmission electron microscopy (HR-TEM) cross-section observation of a 20 nm thick Au film (with either a 2 nm thick Ti or Cr wetting layer), the Ti/Au sample presents as two individual layers of Ti and Au, respectively (Figure 9b), while the Cr/Au sample presents as a single layer instead (Figure 9c). Further characterization with the scanning TEM–energy-dispersive X-ray spectroscopy (STEM–EDX) shows that the interdiffusion length of Cr into Au is about 2–3 nm. Under the micro-four-point-probe measurement, the Ti/Au sample exhibits a lower sheet resistance compared to pure Au, which is due to the fact that the two individual layers act as parallel resistors. By contrast, the Cr/Au sample exhibits a higher sheet resistance than pure Au, due to the interdiffusion of Cr into Au, forming a Cr–Au alloy.

Figure 9. a) Schematic representations showing the cross-sectional atom distributions in the Ti/Au and Cr/Au samples. Ti forms a uniform layer underneath the Au overlayer, while Cr interdiffuses into the Au overlayer and forms a thin Cr–Au alloy layer. b) TEM cross-sectional image of the 2 nm Ti/20 nm Au sample, which presents as two individual layers of Ti and Au, respectively. c) TEM cross-sectional image of the 2 nm Cr/20 nm Au sample, which presents as a single layer. Reproduced with permission.[125] Copyright 2017, American Chemical Society. d) Schematic representation showing the structure of Ag films grown on Ge wetting layers before (left) and after (right) the segregation process occurs. e) Imaginary part of the relative permittivity (ε_2) for a 20 nm thick Ag film deposited on 2 nm thick Ge wetting layer, measured using spectroscopic ellipsometry at 1, 10, and 60 days after deposition (solid lines), as well as Maxwell-Garnett calculation of ε_2 of Ge–Ag mixture with Ge-to-Ag ratio of 2:20 (dotted curve). Adapted with permission.[126] Copyright 2018, Beilstein Journal of Nanotechnology. f) XPS measurements of atomic concentrations of the main elements as a function of Ar-ion etching time obtained for a 100 nm thick Ag film onto a 1 nm thick Ge wetting layer on SiO₂ substrate. Profiles were taken 2 weeks (left) and 4 weeks (right) after the sample deposition. The concentration of Ge is multiplied by a factor of 10. Adapted with permission.[127] Copyright 2015, American Chemical Society. g) Schematic representation showing a Au-based plasmonic nanostructure. The thickness values of the Au layer, adhesion layer (either Ti or Cr), and poly(methyl methacrylate) (PMMA) layer are 30, 2, and 100 nm, respectively. Sample without any adhesion layer is also prepared. h–j) Background-subtracted EEL spectra extracted from the center area of the nanodisk (indicated by the inset in (h)) for samples with (h) no adhesion layer, (i) 2 nm Ti, and (j) 2 nm Cr. The peaks are broader and less resolved in the presence of an adhesion layer, indicating the plasmon damping effect induced by the wetting layer. Adapted with permission.[133] Copyright 2017, American Chemical Society.

Different from Cr, Ge atoms tend to gradually migrate into the grain boundary voids throughout the whole Ag films, leading to separation of Ge atoms in small regimes inside the whole Ag film. This phenomenon is referred as segregation (schematically shown in Figure 9d).[126] Ciesielski et al. reported that Ge segregation leads to a gradual increase of the

ADVANCED
SCIENCE NEWS

www.advancedsciencenews.com

ADVANCED
OPTICAL
MATERIALS

www.advopticalmat.de

optical loss (in terms of the imaginary part of the relative permittivity, ε_2) of the deposited Ag film (Figure 9e). Besides, an additional absorption band around 550 nm gets more obvious with time, which can be attributed to the increased mixing of Ge and Ag atoms. This is confirmed by the Maxwell-Garnett effective medium theory calculation of the effective ε_2 of a silver film with Ge inclusions. Also, Wróbel et al. studied the vertical concentration profile of Ge atoms inside a 100 nm thick Ag film using X-ray photoelectron spectroscopy (XPS), where successive sublayers of a Ge/Ag sample were etched with Ar ions and the elemental compositions of the uncovered surfaces were measured.[127] Figure 9f shows the profiles of atomic concentrations of several main elements as a function of etching time for a 100 nm thick Ag film deposited on SiO$_2$ substrate (with 1 nm thick Ge wetting layer). For measurement of the sample 2 weeks after evaporation, a fraction of Ge atoms has diffused into the Ag grain boundary voids and tend to concentrate on the Ag/air surface, while the rest of Ge atoms remains on the SiO$_2$ substrate (Figure 9f, left panel). The segregation of Ge atoms continues with time. For measurement of sample 4 weeks after evaporation, the amount of Ge atoms on the SiO$_2$ has been further reduced, and Ge atoms are distributed on both Ag grain boundary voids and Ag/air surface (Figure 9f, right panel).

The second issue with the metal wetting layer approach is the induced optical loss by the wetting layer. This is because typical wetting metals (e.g., Cr, Ti, Ni, etc.) usually exhibit larger optical loss compared to the candidate metals (e.g., Ag, Au, etc.). Such issue usually stands out in devices using multiple layers of wetting and candidate metals (such as optical filters and hyperbolic materials employing a multilayer structure[128,129]), or in plasmonic devices where there is an enhanced optical field in the dielectric/metal interface (where the metal wetting layer usually resides[130]). Metal wetting layers can lead to reduced propagation lengths in plasmonic waveguides,[131] or damped plasmon resonances in plasmonic resonators.[132] Madsen et al. studied the plasmon damping effect of wetting layers in Au nanostructures using electron energy loss spectroscopy (EELS).[133] The local plasmon resonances of three Au plasmonic nanostructures (schematically shown in Figure 9g; the characterized structures include one sample with 30 nm thick Au film without any wetting layer, and two samples with either a 2 nm thick Ti or Cr wetting layer) are probed with EELS. Compared to sample without any wetting layer (Figure 9h), sample with either a Ti or Cr wetting layer exhibits both broader and less resolved peaks in the EEL spectrum, due to the induced plasmon damping by the wetting layer (Figure 9i,j). Strategies to mitigate the above issue include carefully optimizing the material and geometry of the employed wetting layer,[134] using nonmetal-based wetting layers,[135,136] or fabricated metallic nanostructures using the wetting-layer-free, codeposition approach (will be discussed in Section 3.2.3).
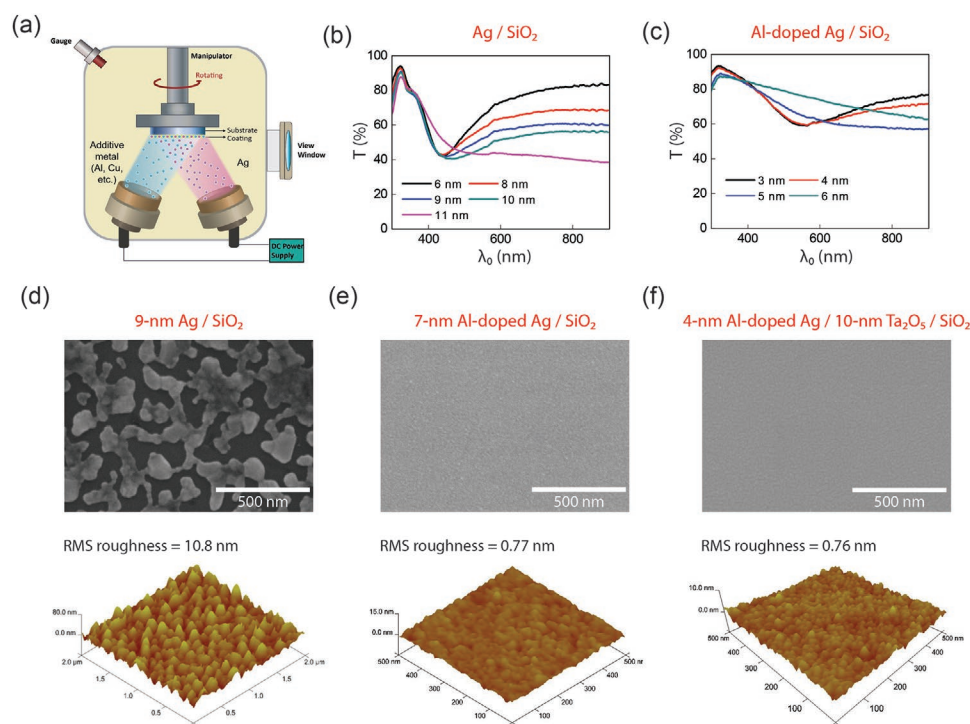
3.2.3. Metal Doping

Doping an additive metal into the candidate metal through a codeposition process is an efficient approach for preparing high-quality, ultrathin, and ultrasmooth metal films without any

wetting layer.[46,137–141] As schematically illustrated in **Figure 10a**, a small amount of additive metal (denoted as X here, which can be Al, Cu, Ti, Ni, Cr, etc.) is codeposited with Ag, creating a X-doped Ag film. During this codeposition process, the deposition rate of metal X is chosen to be much lower than that of Ag. Consequently, the obtained X-doped Ag films maintain the great optoelectronic properties of pure Ag films, while at the same time, exhibit significantly improved surface morphologies with reduced percolation thresholds.

As discussed in earlier sessions, Ag follows the Volmer–Weber growth mode, where the deposited Ag atoms form isolated islands at the initial stage of film growth. For example, a 9 nm thick Ag film shows a discontinuous and rough surface morphology with a RMS roughness value of 10.8 nm, which is even larger than the film's own nominal thickness (Figure 10d).[46] These isolated metallic islands absorb light of specific frequencies due to the induced LSPRs, leading to dips in the measured transmittance spectra. As shown in Figure 10b, there are obvious transmission dips for Ag films with nominal thicknesses below 10 nm. By contrast, by only adding a small amount of Al (≈6% atomic ratio in this case) and keeping other parameters unchanged during the film deposition, the obtained Al-doped Ag films exhibit a "transmission-dip-free" characteristic with a thickness of only 6 nm (Figure 10c), indicating a significantly reduced percolation threshold and improved surface morphology induced by the Al doping.[46,138] For example, a 7 nm thick Al-doped Ag film exhibits a smooth and defect-free surface morphology, with a RMS roughness value of only 0.77 nm (Figure 10e).[137] Furthermore, by first putting a 10 nm thick Ta$_2$O$_5$ wetting layer on the SiO$_2$ substrate, the percolation threshold of the subsequently deposited Al-doped Ag film is further reduced to only 4 nm (Figure 10f).[139]

The codeposited additive metal atoms act as nucleation sites for Ag atoms, and significantly alter their growth dynamics and reduce the associated percolation thresholds. Gu et al. studied the effect of Al doping on the nuclei density of Ag films, where the surface morphologies of pure Ag and Al-doped films (all with a nominal thickness of 3 nm, deposited on the SiO$_2$/Si surface) were characterized by atomic force microscopy (AFM).[138] At such an ultrathin thickness regime where both pure Ag and Al-doped Ag films are still discontinuous, they have already exhibited dramatically different growth behaviors. The pure Ag film is comprised of large particles with irregular sizes (**Figure 11a**, left panel), which corresponds to the fact that Ag follows the Volmer–Weber growth mode and tends to coalesce into isolated islands. By contrast, the Al-doped Ag film consists of tiny and densely distributed particles over the substrate (Figure 11a, right panel). The nuclei density and particle size of metal films are associated to the diffusion rate of the metal atoms on the substrate surface (which is SiO$_2$ for the study here), which is inversely proportional to the metal–oxide bond energy in most cases. Because the Al−O bonds exhibit a much higher strength than the Ag−O bonds, the average diffusion length of Al atoms on the SiO$_2$ surface is much shorter than that of Ag atoms. Consequently, Al atoms are easier to be immobilized on the SiO$_2$ surface, which contributes to an increased density of heterogeneous nucleation sites for Ag atoms and leads to the early stage formation of an ultrathin and

Figure 10. a) Schematic representation of the fabrication procedure of doped Ag thin films. b) Measured transmittance of Ag films with different thicknesses. c) Measured transmission of Al-doped Ag films (Al atomic concentration: ≈6%) with different thicknesses. Adapted with permission.[138] Copyright 2014, American Chemical Society. d) SEM (upper panel) and 2D AFM (lower panel) of a 9 nm thick (nominal thickness) Ag film on fused silica substrate. e) SEM (upper panel) and 2D AFM (lower panel) of a 7 nm thick Al-doped Ag film on fused silica substrate. f) SEM (upper panel) and 2D AFM (lower panel) of a 4 nm thick (nominal thickness) Ag film on fused silica substrate with a 10 nm thick Ta_2O_5 wetting layer.
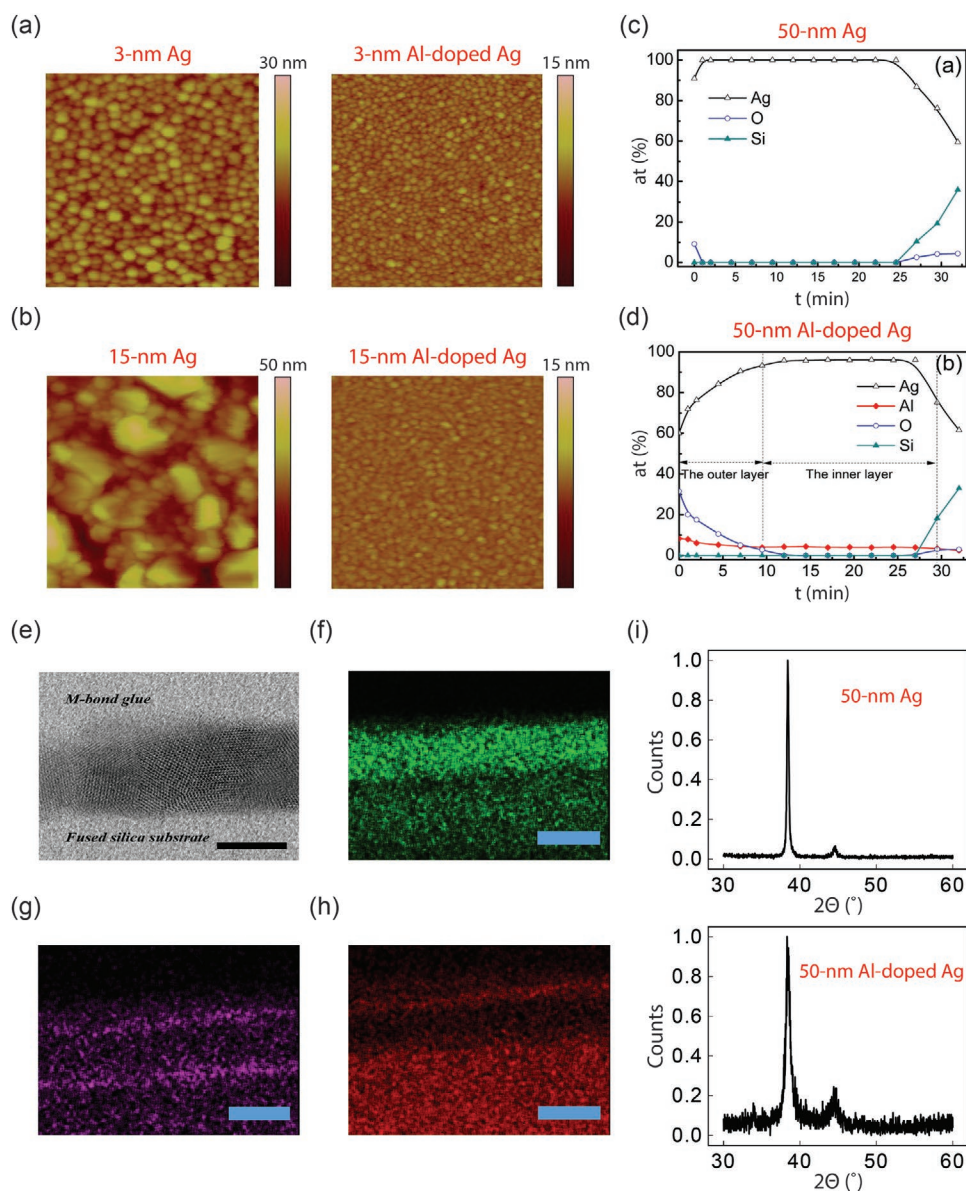
smooth doped Ag film. In addition, similar growth characteristics have been observed in the initial growth stage of Ni-doped Ag films by Zhang et al.[140] As the film continues to grow, the small metal particles coalesce into larger ones. Compared to a pure Ag film, the particle size of an Al-doped Ag film only increases slightly when the film thickness increases from 3 to 15 nm (Figure 11a,b). This suggests that the introduction of Al during the deposition process of Ag reduces the surface diffusion and mass transportation of Ag atoms and suppresses the expansion of Ag particle size.

Investigating how the additive metal elements are distributed inside the doped Ag sample is beneficial to understanding its optoelectronic properties. Toward this goal, Gu et al.[138] have studied the depth profiling of different elements of pure Ag and Al-doped Ag samples using XPS (Figure 11c,d). For ease of experiment and to ensure a full coverage of metal film over the used SiO_2/Si substrate (especially for the pure Ag sample), a film thickness of 50 nm is chosen for both samples. For the 50 nm thick pure Ag film, oxygen is detected only at the surface of the as-prepared sample and the interface between the film and Si substrate. Close to the interface between the film and substrate, O and Si can be detected after the film is etched for 24.5 min (indicating the time needed to completely etch away the 50 nm thick film). By contrast, for the 50 nm thick Al-doped Ag sample, oxygen can be detected from the surface of the as-prepared film toward the substrate for an etching duration of ≈9.5 min (corresponding to about 1/3 of the film thickness). Considering that there is no oxygen produced during

deposition, oxygen in Al-doped Ag films should originate from the ambient atmosphere after the samples are taken out of the vacuum chamber. Furthermore, an Al-enriching feature can be clearly observed in the outer layer of the Al-doped Ag sample. The atomic concentration of Al drops gradually from about 8% for the outermost surface to about 4% for the newly formed surface after 9.5 min of etching. After that, the atomic concentration of Al is almost constant at 4% in the inner layer. This indicates the outward diffusion of Al together with the inward diffusion of oxygen.

Similar findings have been observed in a STEM study of Al-doped Ag films by Zhang et al.[137] Figure 11e shows an annular bright field (ABF) cross-sectional STEM image of a 7 nm Al-doped Ag film, suggesting the film's polycrystalline structure. The element mapping across an ≈16 nm thick film for Ag, Al, and O atoms is characterized by EDX and shown in Figure 11f–h. It can be seen that Al and Ag are mixed throughout the entire film, which corresponds to the fact that these two elements form a solid solution at both ambient and elevated temperatures in the case of a low Al concentration according to their reported phase diagram. There is an enrichment of Al and O elements near the top surface of the Al-doped Ag film, which is consistent with the XPS study.

As mentioned earlier, Al element has a large bond strength with the O element, and therefore, tends to be oxidized easily when exposed to an oxygen-containing environment. For the Al-doped Ag sample, oxygen atoms from ambient

Figure 11. a) 2D AFM images of a 3 nm thick Ag film (left panel) and a 3 nm thick Al-doped Ag film (right panel). b) 2D AFM images of a 15 nm thick Ag film (left panel) and a 15 nm thick Al-doped Ag film (right panel). All scans are performed over a square area of side length of 500 nm. c,d) Composition depth profiles of (c) a 50 nm thick Ag film and (d) a 50 nm thick Al-doped Ag film. All films in (a) to (d) are deposited on SiO_2/Si substrates. Adapted with permission.[138] Copyright 2014, American Chemical Society. e) Annular bright field (ABF) cross-sectional scanning transmission electron microscope (STEM) image of a 7 nm Al-doped Ag film, which shows its polycrystalline structure. The scale bar is 5 nm. f–h) Cross-sectional element mapping of Ag (f), Al (g), and O (h) atom distributions in an ≈16 nm thick Al-doped Ag film. The scale bar is 20 nm. Reproduced with permission.[137] Copyright 2017, Wiley-VCH. i) XRD patterns of a 50 nm thick Ag film and a 50 nm thick Al-doped Ag film. Both films are deposited on SiO_2/Si substrates. Adapted with permission.[138] Copyright 2014, American Chemical Society.
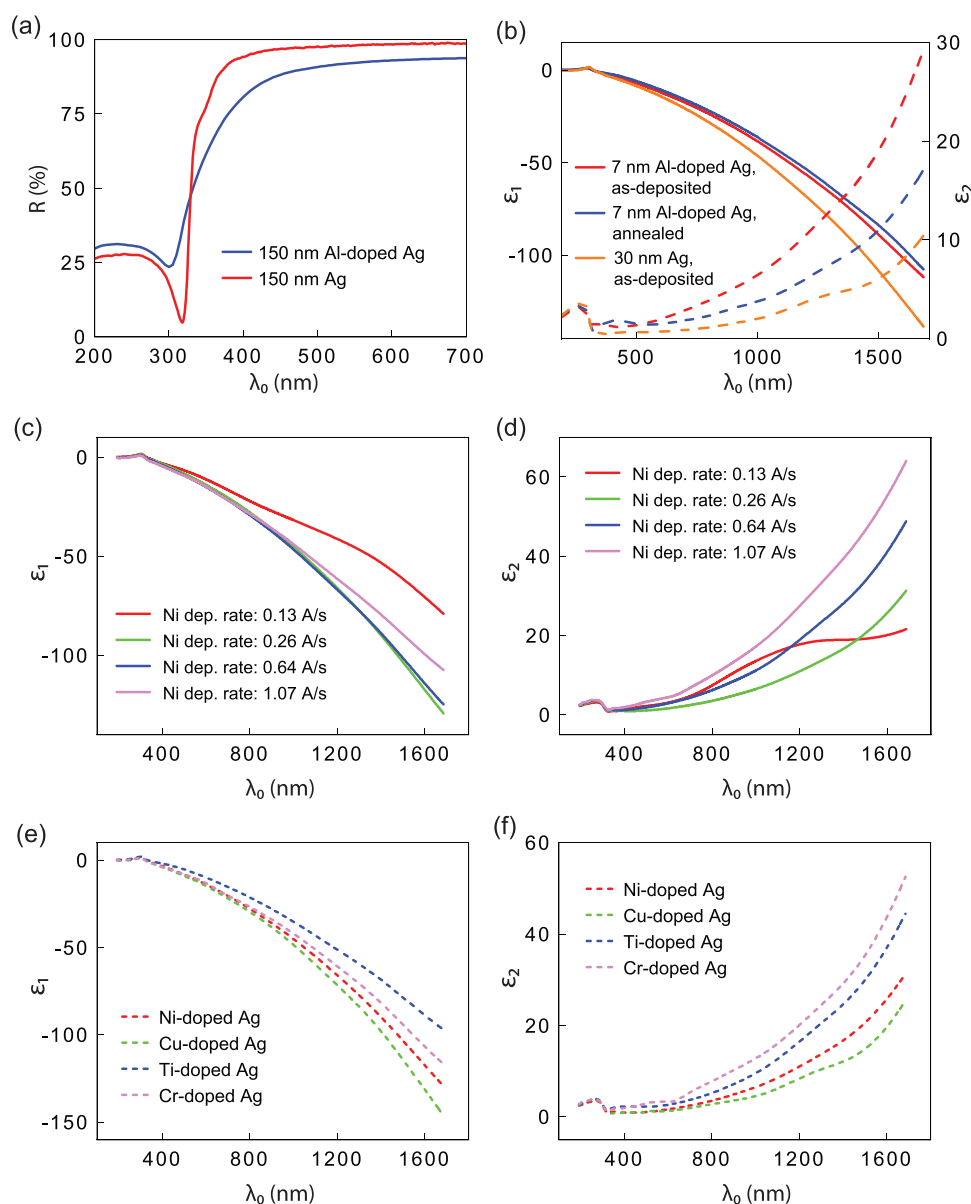
atmosphere diffuse inward into the film, while Al atoms in the film diffuse outward toward the ambient side, and Al−O bonds are spontaneously formed in order to decrease the free energy of the film system. As a result, Al-doped Ag films consist of two layers: an outer layer containing Al−O bonds with ≈1/3 of the thickness of the films and an inner layer composed of Ag and Al. Such a spontaneously formed Al−O network curbs the diffusion of Ag atoms and stabilizes the film. As noted later, an Al_2O_3 layer deposited on top of a thin Ag can further improve the film's stability, due to the barrier property of the Al_2O_3. By

contrast, a thin pure Ag film does not have such a "protection layer," and therefore, can easily dewet from the substrate. Note that although the concentration of Al at the boundaries of Al-doped Ag is higher than that of Al within the film, Ag atoms are still the majority of the film due to the low doping level of Al (≈6% averaged atomic concentration throughout the sample in most cases). Therefore, doping Al into Ag will not significantly alter its optical and electronic properties, while at the same, will greatly improve the film's surface morphology and reduces the percolation threshold.

X-ray diffraction (XRD) characterization further demonstrates that Al doping effectively curbs the grain size enlarging in the doped Ag films. Figure 11i shows the XRD patterns of 50 nm Al-doped Ag films and pure Ag films (deposited on Si substrate). All the diffraction peaks, except the Si (004) peak at 69.68° from the substrate, can be assigned to the cubic Ag. This indicates that Al doping does not introduce any other phase into the Ag films. The average grain sizes for Al-doped Ag and pure Ag thin films, calculated from the full width at half maximum of the main diffraction peak (111) by the Scherrer

equation, are 9.7 and 30.1 nm, respectively. This suggests that Al doping remarkably reduces the grain size of Ag films.

Regarding the film's optical properties, Zhang et al. observed an increase of the plasma frequency (w_p) of the Ag film due to Al doping.[137] The plasma frequency, w_p, is proportional to the metal's free electron density. Since, Ag has one free electron per atom, while Al has three. Therefore, adding Al into Ag increases the density of free electrons and blueshifts the w_p of the resultant film. For a metal film, there is a minimized reflection intensity near its w_p. **Figure 12**a shows the measured

Figure 12. a) Measured reflection intensity spectra from 150 nm thick Al-doped Ag and Ag films. There is an 18 nm blueshift of the plasma frequency, w_p, for Al-doped Ag compared to pure Ag (from 318 to 300 nm), due to the increased density of free electrons by the Al doping. b) Measured real (solid lines) and imaginary (dashed lines) parts of relative permittivity of an as-deposited 7 nm Al-doped Ag film, a 7 nm film underwent annealing treatment (500 °C for 10 s in N_2), and a 30 nm as-deposited pure Ag film. Adapted with permission.[137] Copyright 2017, Wiley-VCH. c,d) Real (c) and imaginary (d) parts of measured relative optical permittivities of Ni-doped Ag films with different Ni concentrations. The deposition rate of Ag is fixed at 11.09 A s^{-1}, whereas the rate of Ni varies. e,f) Real (e) and imaginary (f) parts of measured optical relative permittivities of doped Ag films with different doping metals. The doping concentration is chosen as "medium" for all four films, and the corresponding deposition rates are listed in Table 3. Adapted with permission.[140] Copyright 2019, American Chemical Society.

Table 3. Summary of optoelectronic properties of doped Ag with different doping concentrations.[140] Note: L, M, and H refer to low doping concentration, medium doping concentration, and high doping concentration, respectively. The deposition rate of the additive metal is listed in the row 3, while the deposition of Ag is fixed as 1.109 nm s^{-1}. Each sheet resistance value is an averaged one from measurements of three ≈7 nm film. The averaged visible transmittance is a simulated value of a 7 nm thick film, using the experimentally measured optical permittivity values of an ≈7 nm thick film.

Doping concentration	Ni-doped Ag			Cu-doped Ag			Ti-doped Ag			Cr-doped Ag		
	L	M	H	L	M	H	L	M	H	L	M	H
Deposition rate [nm s^{-1}]	0.013	0.026	0.064	0.009	0.019	0.208	0.027	0.041	0.067	0.046	0.075	0.119
Averaged visible (400–700 nm) transmittance [%]	77.01	79.27	73.79	78.93	80.74	77.01	69.62	78.66	73.06	70.06	75.68	71.99
Sheet resistance [$\Omega \square^{-1}$]	19.52	18.92	25.70	12.48	12.33	19.37	50.5	46.5	56.5	30.9	24.3	43.1

reflection spectra of optically opaque (≈150 nm thick) Ag and Al-doped Ag films, where there is an 18 nm blueshift of w_p for Al-doped Ag compared to pure Ag (from 318 to 300 nm).

Regarding the film's electronic properties, the effect of Al doping on the electronic band structure of Ag is not obvious, largely due to the low concentration of Al atoms. For Ag, the interband electron transition from the occupied bound d states to unoccupied hybridized sp states leads to an increased absorption over the ultraviolet (UV) range, corresponding a peak in the imaginary part of the relative permittivity (ε_2). Figure 12b plots the measured real and imaginary parts of the relative permittivities of a 7 nm thick as-deposited Al-doped Ag film, a 7 nm thick Al-doped Ag film undergoing an annealing treatment (500 °C for 10 s in N$_2$ environment), and a 30 nm thick as-deposited pure Ag film. The peak wavelengths of interband transitions of both Al-doped Ag and pure Ag overlap with each other, indicating no obvious difference in their electronic band structures. In addition, the scattering loss of an ultrathin Al-doped Ag film is higher than a thicker (30 nm) pure Ag film, due to various factors including the introduction of "Al impurities," reduced film thickness, scattering of electrons due to the fine grains inside the polycrystalline doped Ag film (shown in Figure 11e), etc. However, by annealing the Al-doped Ag film for only 10 s, the imaginary part of permittivity, ε_2, can be significantly reduced over a large wavelength range, while the real part of permittivity, ε_1, maintains a similar value compared to that of as-deposited Al-doped Ag.

Metal doping offers benefits such as reduced percolation threshold, improved surface morphology, enhanced long-term and thermal stability. Moreover, by controlling the doping concentrations of the additive metal, or by employing different doping metal species, the optoelectronic properties of doped Ag films can be readily adjusted. As stated earlier, the optical loss of the metal thin film is directly proportional to the imaginary part of optical permittivity, ε_2. Zhang et al. characterized the optical permittivities of ≈7 nm thick Ni-doped Ag films with different Ni concentrations.[140] In this study, the deposition rate of Ag is fixed at 1.109 nm s^{-1}, while the rate of Ni varies. When the deposition rate of Ni is low (at 0.013 nm s^{-1}, which corresponds to the "low" concentration of Ni in the obtained doped Ag), the film resembles a defected thin Ag film. The imaginary part of optical permittivity, ε_2, exhibits a large value in the visible range, indicating a high optical loss. This is because of the "incomplete" wetting of Ag atoms due to the "less-than-necessary" additive Ni atoms. Increasing the Ni concentration gradually reduces ε_2 in the visible range. When the deposition
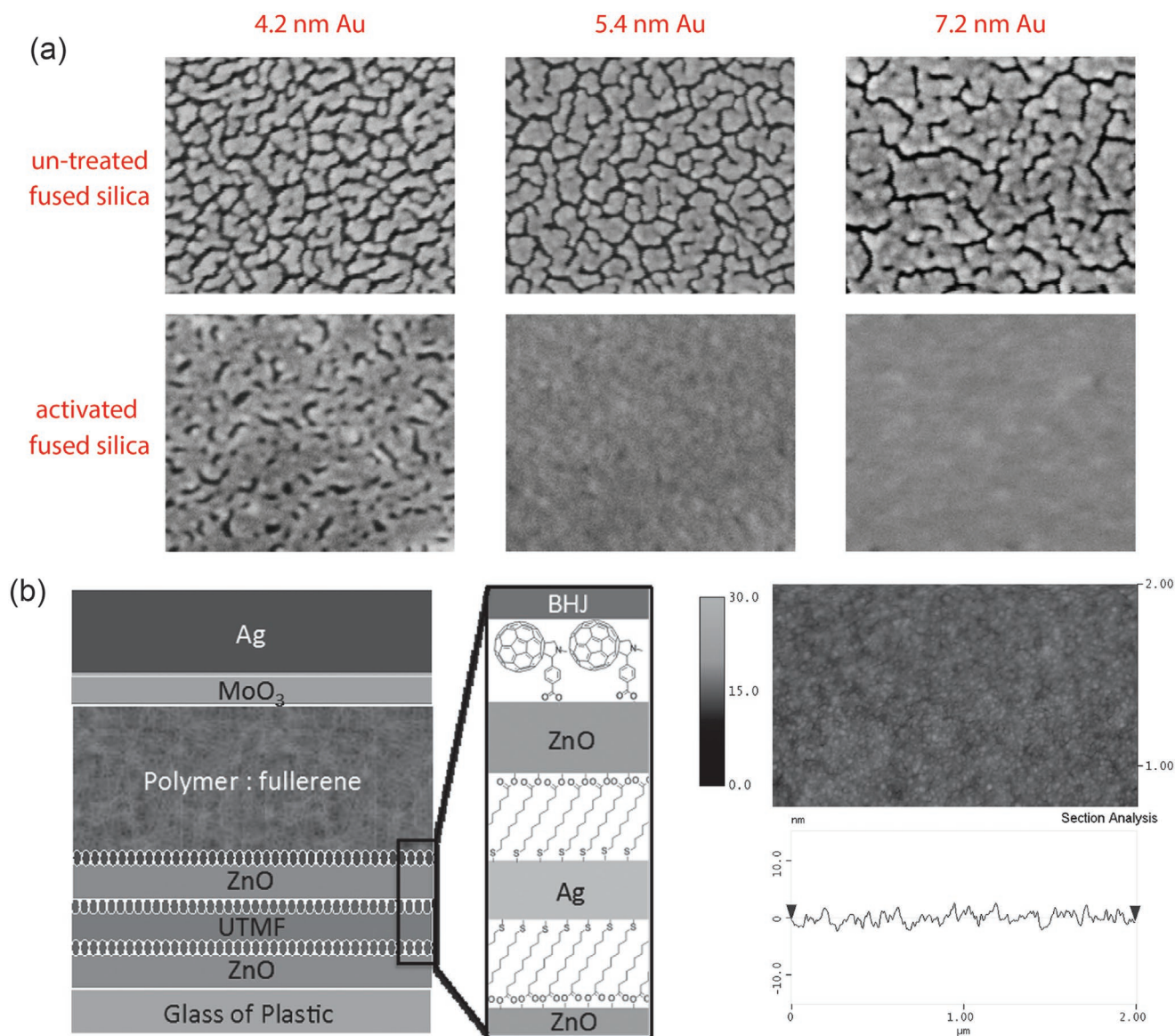
rate of Ni reaches 0.026 nm s^{-1}, the film has the lowest ε_2 across the visible and near-IR range, which follows the trend of Drude model for free-electron metals. The corresponding concentration of Ni atoms in the obtained doped Ag film is denoted as "medium." With the further increase of the Ni deposition rate (corresponding to a "high" concentration), ε_2 of the fabricated film increases again, due to the scattering of free electrons by the "more-than-necessary" Ni atoms. Similar trends of the evolution of permittivity with the doping concentration have been observed in other types of doped Ag as well (e.g., Al-doped Ag, Cu-doped Ag, etc.).[140]

Finally, the permittivity of doped Ag can also be adjusted by employing different additive metals. Figure 12e,f plots the measured curves of ε_1 and ε_2 for ≈7 nm thick doped Ag films with various additive metals (the doping concentration is chosen as the "medium" level for all samples). Considering the FoM for a metallic film (FoM = $\varepsilon_1/\varepsilon_2$), Cu-doped Ag exhibits the highest FoM over the spectral range of 200–1690 nm, Ni-doped Ag has an intermediate FoM, while Cr- and Ti-doped Ag have relatively low FoMs. The averaged visible transmittance and sheet resistance of doped Ag films with different doping elements and concentrations are listed in **Table 3**.

3.2.4. Molecular Surfactant

Molecular surfactant is another alternative method to promote high-quality ultrathin metal film growth, without inducing additional optical loss as in the case of metallic wetting layer or metal doping approach. By applying a thin layer of molecular surfactant with the desired chemical moieties on the substrate, the adhesion between the substrate and candidate metal can be significantly enhanced. Consequently, this leads to the immobilization of the metal adatoms on the substrate surface and suppression of their intrinsic Volmer–Weber growth mode.

Silane-based molecular surfactant has been shown to be an effective wetting promotor for thin Au films deposited on oxide surfaces.[142–147] Kossoy et al. have shown that continuous Au films (with a thickness down to 5.4 nm) can be deposited on fused silica substrate pretreated with (3-mercaptopropyl)trimethoxysilane (**Figure 13**a).[144] However, optical transmittance of the fabricated Au film is lower than expected for an ideal Au film with the same mass-equivalent thickness, due to nonabrupt transition zones between the metal and the surrounding dielectrics. Leandro et al. studied different wetting effects of amino- and mercapto- silane on

ADVANCED
SCIENCE NEWS
www.advancedsciencenews.com

ADVANCED
OPTICAL
MATERIALS
www.advopticalmat.de

Figure 13. a) SEM images of Au films (of different thicknesses) deposited on untreated fused silica substrates (top row) and on fused silica substrates pretreated with (3-mercaptopropyl)trimethoxysilane. The deposition rate is 0.1 nm s^{-1}. All images are 300 nm across. Adapted with permission.[144] Copyright 2014, Wiley-VCH. b) Left: schematic drawing of the polymer solar cell device and the molecular structure of the two 11-mercaptoundecanoic acid (MUA) self-assembled monolayer (SAM) and the fullerene-based SAM used for interfacial modifications. Right: AFM image of a 10 nm ultrathin Ag film on top of glass/ZnO/MUA. The measured surface RMS roughness is 0.95 nm. Adapted with permission.[148] Copyright 2014, Wiley-VCH.

ultrathin Au film formation, where they found that aminosilane-based surfactant exhibited the best wetting effect and 6 nm thick continuous Au films can be deposited over Si substrate with a surface roughness value less than 0.3 nm.[145] Stec et al. developed a novel process of using a mixed monolayer of (3-mercaptopropyl)trimethoxysilane and (3-aminopropyl)trimethoxysilane via codeposition from the vapor phase.[146] Highly conductive (sheet resistance: ≈11 Ω □$^{-1}$) and ultrathin (≈8 nm) Au films are deposited on glass with a low RMS surface roughness (≈0.4 nm), that are robust toward UV/O$_3$ treatment and ultrasonic agitation in a range of common solvents. The above method was later employed to fabricate 8 nm thick

Ag- and Cu-based transparent flexible electrodes for organic photovoltaic devices.[147]

Zou et al. demonstrated high-performance electrode having a ZnO/Ag/ZnO trilayer structure, where each of the interfaces in the above electrode is individually optimized with functional self-assembled monolayer (SAM) surfactant (Figure 13b, left panel).[148] The ZnO/Ag interface is modified with a double-end functionalized 11-mercaptoundecanoic acid (MUA) SAM to covalently attach Ag and ZnO together. The subsequently deposited 10 nm thick Ag film exhibits a smooth surface morphology with a RMS roughness of 0.95 nm (Figure 13b, right panel). Furthermore, a dipolar MUA SAM is applied at the

**ADVANCED
SCIENCE NEWS**

www.advancedsciencenews.com
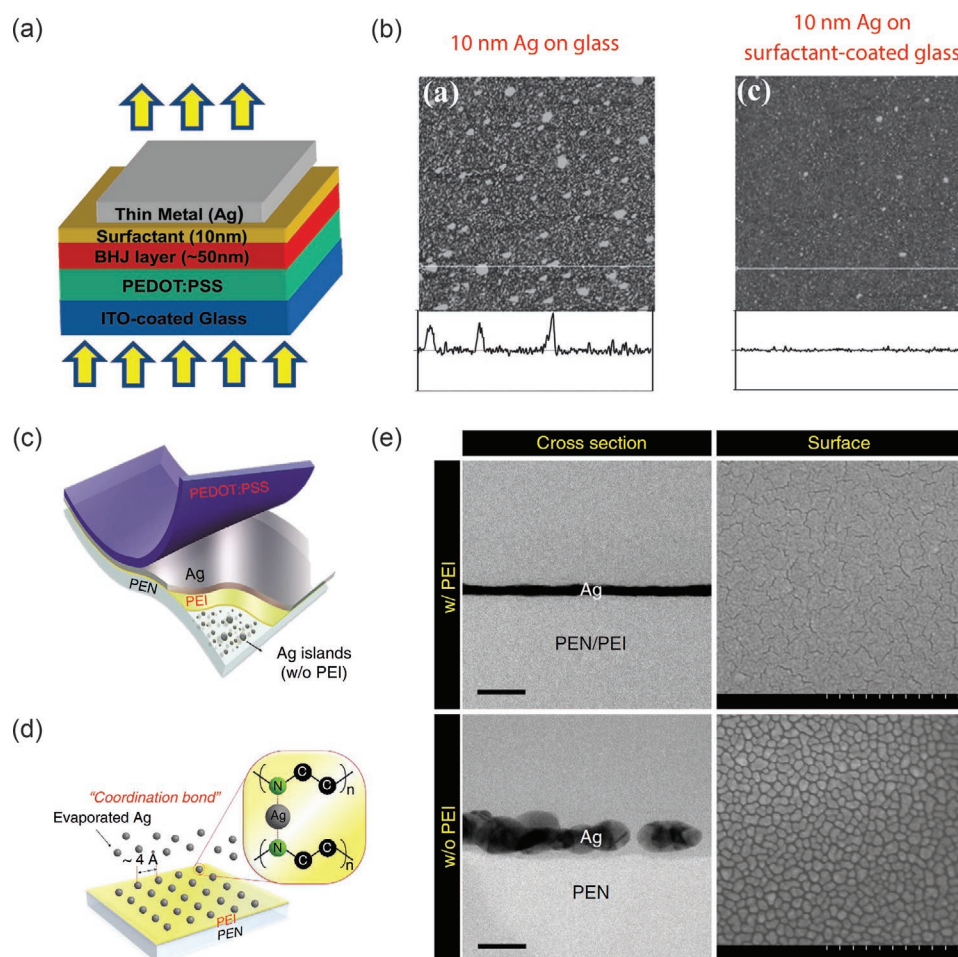
**ADVANCED
OPTICAL
MATERIALS**

www.advopticalmat.de

Ag/ZnO interface to achieve Ohmic contact, and a fullerene-based SAM is applied on the top ZnO layer to passivate the inorganic surface traps and improve interfacial exciton dissociation between the ZnO and active layer.

3.2.5. Polymer Surfactant

Like molecular surfactant, polymer surfactant works in a similar manner and provides strong bonds between the substrate and the candidate metal, leading to immobilization of the deposited metal adatoms over the substrate surface.[135,149–151] Bi et al. employed SU-8 polymer with sulfur-containing groups to enhance the formation of ultrathin (≈8 nm) Au films.[149] Chueh et al. employed a 10 nm thick fullerene-containing surfactant layer as both an interfacial electron selective layer for facilitating charge transport and a wetting layer for promoting ultrathin Ag film growth (**Figure 14**a).[150] A 10 nm thick Ag film deposited over a surfactant-coated glass substrate exhibits a

smooth surface morphology, while Ag film of the same thickness deposited directly on glass shows a granular morphology (Figure 14b). Such a polymer/Ag bilayer is used as the cathode in semitransparent organic solar cells. Kang et al. used an ≈5 nm thick polyethyleneimine (PEI) surfactant to fabricate ultrathin Ag films over a flexible polyethylene naphthalate (PEN) substrate (Figure 14c).[151] The functional amine groups of PEI act as a ligand and donate an unshared electron pair to the Ag atoms to create a coordination bond. Consequently, the initially deposited Ag atoms are immobilized and densely distributed Ag nuclei over the entire substrate surface are obtained (Figure 14d), which facilitate the subsequent high-quality, ultrathin Ag film formation (Figure 14e).

Compared to other wetting methods discussed in previous sections, the molecule or polymer surfactant technique is "metal-free," and therefore, avoids any undesired optical absorption induced by the wetting layer itself. However, many of the surfactant layers need to be applied over the substrate surface through separate, nonvacuum-deposition processes

Figure 14. a) Device schematic of the semitransparent organic photovoltaic device, where the polymer surfactant/Ag bilayer is used as the cathode. b) The AFM height images (over a 5 × 5 µm² area) and surface profiles of 10 nm thick thin Ag films deposited on glass (left) and polymer-surfactant-coated glass (right). Adapted with permission.[150] Copyright 2013, Wiley-VCH. c) Schematic of the flexible PEI/Ag/poly(3,4-ethylenedioxythiophene) polystyrene sulfonate (PEDOT:PSS) electrode consisting of the ultrathin Ag film between the PEI and PEDOT:PSS layer. d) Conceptual diagram for the growth mechanism of Ag films with PEI nucleation inducers. e) Cross-sectional and surface morphology images of the PEI/Ag and bare Ag electrodes taken using transmission electron microscopy (TEM) and SEM, respectively. Scale bars, left 50 nm, right 500 nm. Reproduced with permission.[151] Copyright 2015, Nature Publishing Group.

ADVANCED
SCIENCE NEWS
www.advancedsciencenews.com

ADVANCED
OPTICAL
MATERIALS
www.advopticalmat.de

such as solvent dipping,[144,145] vapor evaporation,[146,147] or spin coating,[148,150,151] which could be time-consuming and difficult to be employed for mass production. Such limited scalability might constrain the technique's usage in large-scale and high-throughput thin-metal-film-based electrode manufacturing.
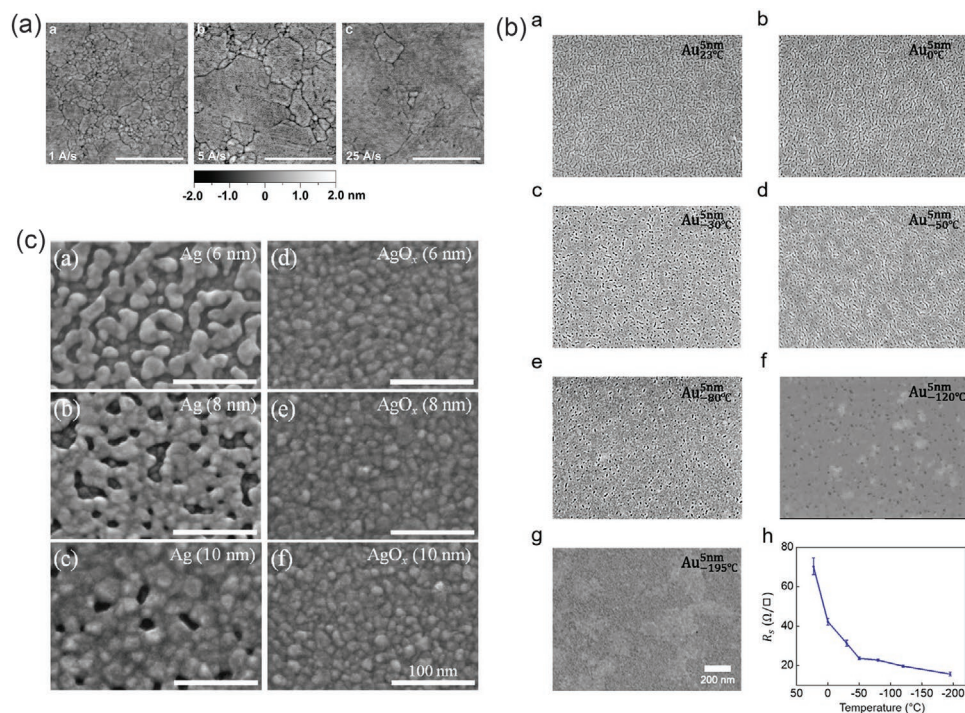
3.2.6. Deposition Conditions

Besides various wetting-layer approaches elaborated in previous sections, deposition conditions also play a vital role in determining the morphology and optoelectronic properties of thin metal films. As the deposition conditions consist of many different factors and could vary from tool to tool or among research groups, here we only discuss some general guidelines when choosing the proper deposition conditions for high-quality, ultrathin metal film preparation.

First of all, vacuum condition plays an important role in affecting the properties of deposited thin metal films. As the chamber base pressure gets reduced, the mean free paths of metal adatoms increase accordingly and they are able to maintain good kinetic energies when landing on the substrate. This benefits the nucleation and coalescence stages of a thin film formation. At the same time, when the chamber base pressure gets reduced, the amount of residual gases (e.g., water vapor, oxygen, etc.) inside the deposition chamber drops down. These gases can be absorbed by the freshly deposited metal films and then form defect centers inside the films, affecting their optical

and electrical properties.[152] For example, Abd El-Fattah et al. reported atomically thin (<5 nm), single-crystalline Ag films on Si substrate deposited under an ultrahigh vacuum condition ($\approx 7.5 \times 10^{-11}$ Torr base pressure) and with other precisely controlled tool factors.[153] Second, deposition rate is another important factor affecting the properties of deposited films.[154,155] Generally speaking, faster deposition rates suppress the surface-diffusion-enabled agglomeration and yield metal films of better quality. **Figure 15**a shows the AFM images of three Ag films deposited under high vacuum conditions ($\approx 3 \times 10^{-8}$ Torr base pressure), but at different rates.[156] The film deposited with the highest rate (2.5 nm s^{-1}) exhibits the largest grain size and the lowest optical loss.

Substrate temperature can be another important factor influencing the properties of deposited metal films. High temperature provides more kinetic energy for the metal adatom's diffusion over the substrate surface and increases the grain size of deposited metal films, even leading to single-crystalline film formation in some studies.[157–159] Although an elevated temperature is beneficial for depositing high-quality thick metal films, it can be detrimental to ultrathin metal films which are more prone to surface roughing and dewetting. Also, as many transparent conductors are deposited on flexible substrates, a high deposition temperature is not compatible. Studies have shown that substrate cooling is indeed beneficial for high-quality, ultrathin metal film formation.[48,96,160] Lemasters et al. have found that by cooling the substrate to cryogenic temperatures (≈ -195 °C), wetting-layer-free plasmonic Au films with

Figure 15. a) AFM images of template-stripped Ag films deposited at a base pressure of $\approx 3 \times 10^{-8}$ Torr but at different rates. The film deposited using the highest rate exhibits the largest grain size and thus, the lowest optical loss. Reproduced with permission.[156] Copyright 2015, American Chemical Society. b) SEM images and measured sheet resistance values of 5 nm thick Au films deposited using different substrate temperatures. As the temperature approaches the cryogenic temperature, the film surface morphology gets improved and the sheet resistance gets reduced. Reproduced with permission.[48] Copyright 2015, American Chemical Society. c) SEM images of Ag and oxygen-doped Ag layers of different thicknesses on ZnO films. Oxygen doping improves the morphology of ultrathin Ag films. Reproduced with permission.[161] Copyright 2013, Wiley-VCH.

**ADVANCED
SCIENCE NEWS**
www.advancedsciencenews.com

**ADVANCED
OPTICAL
MATERIALS**
www.advopticalmat.de

thicknesses down to 3 nm can be obtained.[48] As shown in Figure 15b, as the substrate temperature goes down, the surface morphology of 5 nm thick Au films gets improved and at the same time, the associated sheet resistance gets reduced.

Finally, it is worth noting that although residual gas is commonly considered to be harmful for high-quality metal film deposition, recent studies have shown that by introducing a proper trace amount of oxygen or nitrogen gas (along with the argon gas) during a sputter deposition process, ultrathin and continuous Ag or Cu films can be obtained.[161–164] As an example, Wang et al. have shown that by using a gas mixture of argon and oxygen during Ag sputtering, continuous and low-loss oxygen-doped Ag (O/Ag = 3.4 at%) layers of thicknesses down to 6 nm can be deposited on ZnO films (Figure 15c).[161]

3.3. Methods to Enhance Stability of Thin Silver Films

Stability of thin-metal-film-based transparent conductor is essential for its practical applications. Although Ag is the most promising candidate material by its highest electrical conductivity and lowest optical loss over the visible and near-IR range among different metals, it is known to exhibit relatively poor stability. Under ambient environment, the surface of a Ag film can exhibit a degraded morphology over time, or get tarnished due to the presence of small amount of trace air pollutants (e.g., hydrogen sulfide, chlorine, nitrogen dioxide, etc.).[165,166] As mentioned in earlier sessions, segregation of the wetting-layer atoms could also change the optical and electronic properties of Ag films.[126] The above issues are further aggravated when the film size is reduced to the thin film regime where the surface boundary plays a crucial role and the recrystallization temperature gets reduced. Finally, under elevated temperatures or with high humidity, the degradation of Ag is significantly accelerated.[167,168] Beyond certain temperature, Ag films could completely dewet from the substrate, resulting in optically lossy and electrically insulating films.[169–171]
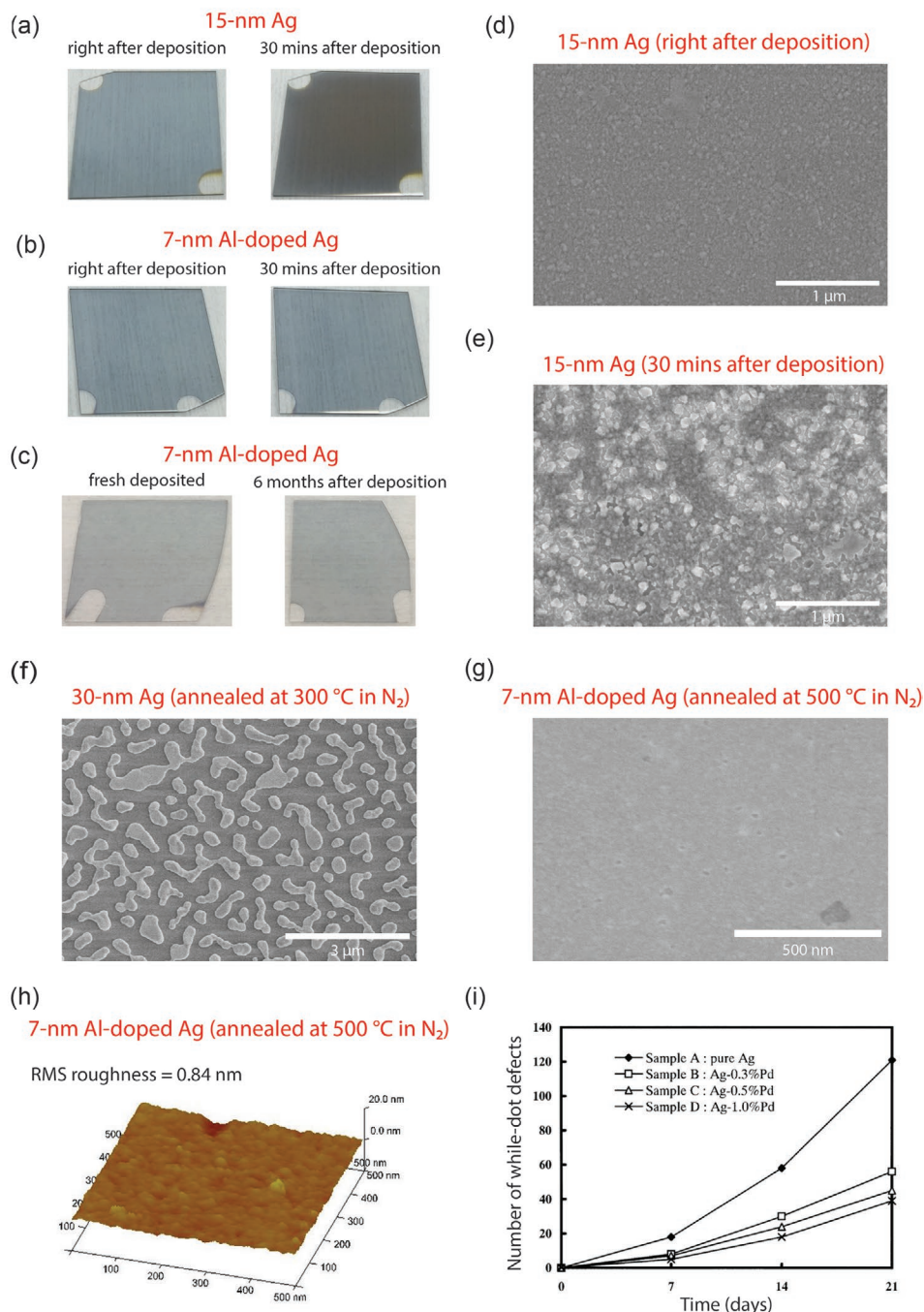
Zhang et al. studied the morphology change of thin Ag films during a short period after deposition.[137] **Figure 16**a shows the images of a 15 nm thick Ag film (deposited on fused silica substrate) right after and 30 min after being taken out of the deposition chamber. The freshly deposited sample exhibits a uniform and bright-colored appearance (Figure 16a, left panel). However, it degrades rapidly in air, ending in a tarnished and dark-colored appearance after only 30 min in ambient condition (Figure 16a, right panel). A similar degradation phenomenon has been observed in 50 nm thick Ag films as well.[172]

One common incorrect explanation of such degradation phenomenon is "the oxidation of Ag in air." Since Ag exhibits one of the lowest adhesion strengths with oxide among common metals, it will not be easily oxidized in a dry ambient environment.[138,173] Instead, we believe that the above degradation comes from the morphology change of Ag surface when the sample is moved from the vacuum chamber into the ambient environment. To illustrate this, the corresponding SEM images of the samples in Figure 16a are shown in Figure 16d,e, respectively. It can be seen that during a short 30 min period, Ag atoms have started to aggregate into islands over the sample surface, leading to an obvious morphology change of the sample as well
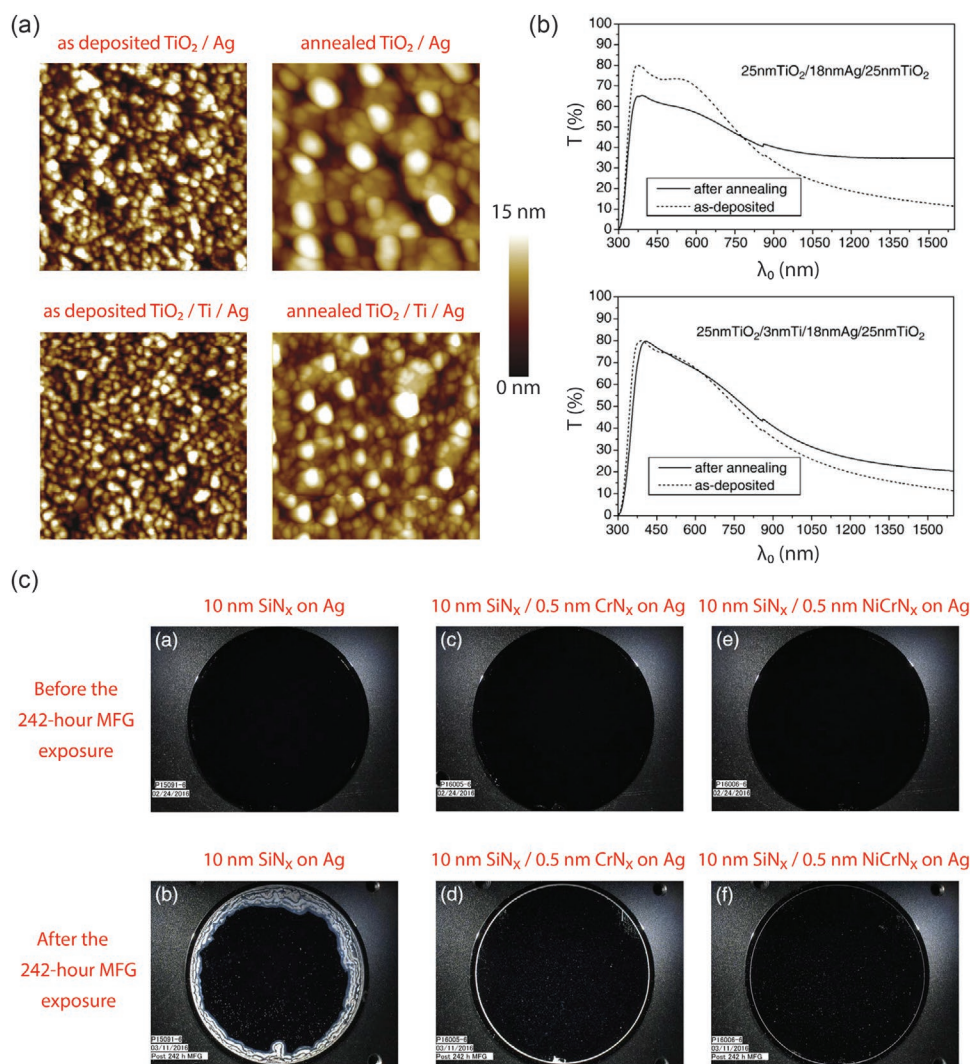
as its visual appearance. When the surrounding environment changes (such as from vacuum to air), the Ag atoms will start to migrate over the film surface and try to form a new "stable" state. Since Ag atoms are preferred to aggregate with each other than with the substrate, the newly formed "stable" state will be a rough film surface with agglomerated Ag islands. Moreover, such instability is greatly accelerated by heating. For example, a continuous 30 nm thick Ag film will dewet from the substrate and form completely isolated Ag "droplets" after the sample is annealed in a nitrogen (N_2) environment at 300 °C for 3 min (Figure 16f). Indeed, thermal annealing of continuous Ag films has become a convenient fabrication method to prepare Ag nanoparticles over large areas.[171,174,175]

As noted in earlier sections, the stability of Ag can be significantly enhanced by metal doping.[137,138,168,176] Within the same 30 min period right after the sample is taken out of the deposition chamber, there is no noticeable visual appearance change of a 7 nm thick Al-doped Ag sample (Figure 16b). In fact, the sample is stable under ambient conditions for over six months without any protective layer (Figure 16c). Furthermore, the thermal stability of Al-doped Ag is significantly improved compared to pure Ag. Figure 16g shows the SEM of a 7 nm Al-doped Ag film after a thermal treatment at 500 °C in a N_2 environment for 3 min, where the sample still maintains its smooth surface morphology and its surface RMS roughness increases slightly from 0.77 to 0.84 nm (Figure 16h). Furthermore, such thermal treatment helps to remove defects inside the sample, and therefore, reduces the optical loss of the as-deposited Al-doped Ag films (shown in Figure 12b). Detailed analysis of the effect of Al doping on the properties of Ag films has been explained in Section 3.2.3. Ando et al. showed that an increase in the palladium (Pd) amount inside a 9 nm thick Ag film can suppress deterioration of the sample under high-temperature and high-humidity conditions.[168] They prepared samples of the same three-layer-structure: Al-doped ZnO (AZO) (38 nm)/ Ag (9 nm, with varying Pd amounts)/AZO (16 nm)/glass, and evaluated their degradation characteristics under a moisture test (40 °C temperature and 90% relative humidity) by counting the white-dot defects larger than 0.2 mm in diameter in an area of a side length of 10 mm. It is found that the induced deterioration is remarkably reduced for samples with higher Pd contents (Figure 16i). The mechanism of Pd doping for enhancing the stability of Ag can be attributed to the formed PdO passivation layer, which retards the dissolution of Ag atoms.[177]

Many wetting layers are found beneficial not only for preparing high-quality thin Ag films, but also for enhancing their stability.[178–180] Wetting layers help to form Ag films with reduced defects and improved adhesion with the substrate during deposition. After deposition, wetting layers further constrain the migration and agglomeration of Ag atoms under heating or humidity conditions. Both effects work together to enhance the stability of thin Ag films. Wang et al. studied the effect of Ti wetting layers on the stability of TiO_2/Ag/TiO_2 multilayered structures.[178] **Figure 17**a shows the 2D AFM images of the as-deposited and annealed (300 °C in air for 30 min) 18 nm thick Ag films, which are deposited on a 25 nm thick TiO_2 layer without and with a 3 nm thick Ti wetting layer. It can be seen that the TiO_2/Ti/Ag sample exhibits a smoother surface morphology compared to the TiO_2/Ag sample, both after deposition

Figure 16. a) Images of a 15 nm thick Ag film on fused silica substrate right after being taken out of the deposition chamber (left panel) and after being kept in ambient air environment for 30 min (right panel). b) Images of a 7 nm thick Al-doped Ag film on fused silica substrate right after being taken out of the deposition chamber (left panel) and after being kept in ambient air environment for 30 min (right panel). c) Images of a 7 nm thick Al-doped Ag film sample which is freshly deposited and a 7 nm thick Al-doped Ag sample which has been kept in ambient air environment for half a year. d) SEM of a 15 nm thick fresh Ag film on fused silica substrate. e) SEM of a 15 nm thick Ag film on fused silica substrate, which has been kept in ambient air environment for 30 min. f) SEM of a 30 nm thick Ag film on fused silica substrate, which has undergone annealing in N_2 environment at 300 °C for 3 min. The film has totally dewetted from the substrate. g,h) SEM (g) and AFM (h) of a 7 nm thick Al-doped Ag film on fused silica substrate, which has undergone a 500 °C annealing treatment in N_2 for 10 s. Adapted with permission.[137] Copyright 2017, Wiley-VCH. i) Moisture test results (in terms of the number of white-dot defects) of the Ag samples with different palladium contents. All samples have the same structure of AZO (38 nm)/Ag (9 nm, with varying Pd contents)/AZO (16 nm)/glass. The moisture test has a temperature of 40 °C and a relative humidity of 90%. Reproduced from permission.[168] Copyright 2000, Elsevier Science Ltd.

**ADVANCED
SCIENCE NEWS**

www.advancedsciencenews.com

**ADVANCED
OPTICAL
MATERIALS**

www.advopticalmat.de

Figure 17. a) AFM images of the as-deposited and annealed 18 nm thick Ag films on 25 nm thick TiO_2 layers without and with 3 nm thick Ti wetting layers. b) Effect of a 3 nm thick Ti wetting layer on the transmittance of the as-deposited and annealed multilayer samples on glass. Adapted with permission.[178] Copyright 2006, Elsevier B.V. c) Dark field optical microscopy images of Ag mirrors with different protection layers before (upper panel) and after (lower panel) of a 242 h mixed flowing gas (MFG) exposure. Adapted with permission.[185] Copyright 2017, The Optical Society.

and after annealing. The RMS roughness values of the as-deposited and annealed TiO_2/Ag films and the as-deposited and annealed TiO_2/Ti/Ag films are 3.0, 9.8, 2.7, and 5.0 nm, respectively. In addition, the sample's transmission spectrum shows a better stability and exhibits a less obvious change after annealing, when the TiO_2/Ag/TiO_2 multilayered structure is inserted with a 3 nm thick Ti wetting layer (Figure 17b).

Adding protection layers on top of Ag films is another useful method to enhance their stability. Moisture is known to trigger the degradation of Ag films. Coating a dielectric layer atop the Ag film could be useful to block the penetration of moisture from the ambient environment into Ag, though cautions are needed to ensure that the dielectric layer itself does not degrade easily by heating or humidity.[167,181–184] Nichrome, chrome nitride (CrN), or nichrome nitride ($NiCrN_x$) coating acts as an effective passivation medium for Ag film protection, and remarkably, even a sub-nanometer thick coating can greatly

improve Ag's stability.[185–189] In many cases, the above thin coatings are employed together with a silicon nitride (SiN_x) protection layer on top. Folgner et al. applied the mixed flowing gas (MFG) exposure to Ag mirrors with different protection layers to evaluate their environmental durabilities.[185] Compared to the Ag mirror with a 10 nm thick SiN_x protection layer, mirrors with either a 0.5 nm CrN_x/10 nm SiN_x protection layer or a 0.5 nm $NiCrN_x$/10 nm SiN_x protection layer show less visual degradation and improved stability after 242 h of MFG exposure (Figure 17c).

Finally, SAMs can also work as effective protection layers for Ag films.[190–194] Several studies have shown the protection property of thiol compounds on Ag surfaces. Due to their ability to form densely packed and complete films on metallic supports, SAMs derived from thiols are useful in blocking electron transfer or in inhibiting the transport of corrosive species.[195] Evesque et al. studied the formation of hexadecanethiol-based

SAM on silver mirror to prevent its tarnishing.[193] The SAM layer over the mirror surface can impede the diffusion of dissolved oxygen, and thus, slows down the reaction rate of silver sulfide formation.

4. Spectroscopic Ellipsometry Characterization of Ultrathin Metal Films

Precisely and reliably characterizing both the optical properties (e.g., refractive index, reflection spectrum, transmission spectrum, etc.) and structural properties (e.g., film thickness, surface roughness, composition, etc.) of a thin metal film is not only essential for optimizing its fabrication process, but also important for an accurate optical design of thin-metal-film-based optoelectronic devices. In this session, we will explain how spectroscopic ellipsometry measurement can be utilized as a straightforward and reliable technique for characterizing thin metal films.
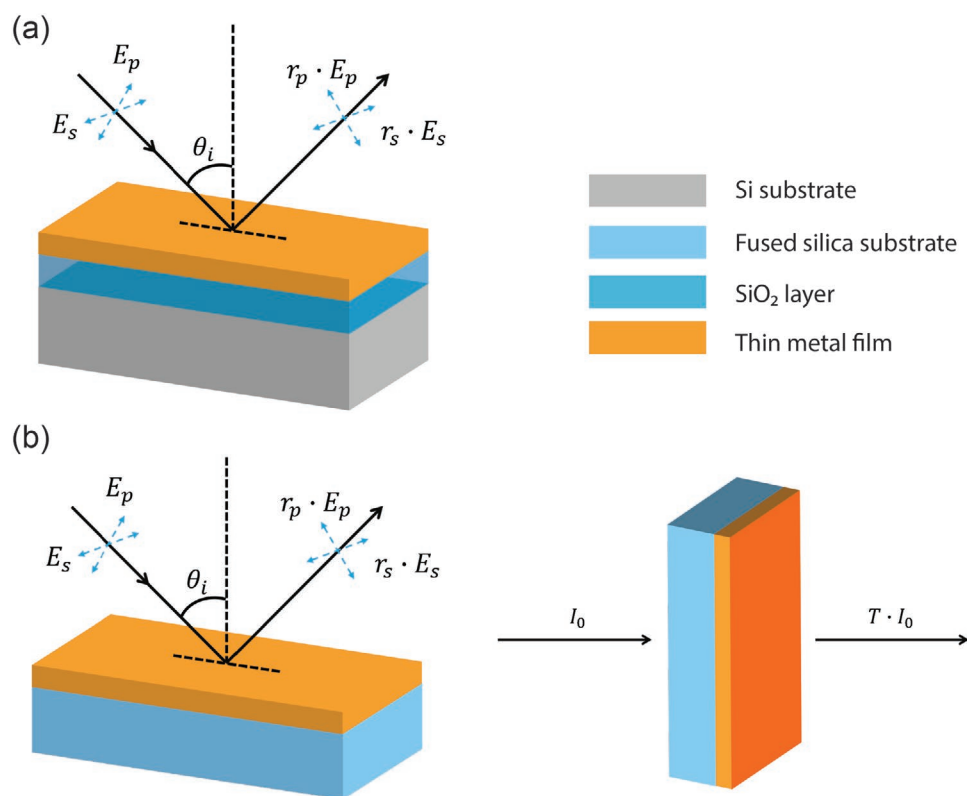
Ellipsometry measures the change in state of polarization (SOP) when light gets reflected from or transmits through a sample. The recorded change is sensitive to both the sample's optical properties, film thickness, as well as structural morphology. Therefore, ellipsometry can be used to determine the complex refractive indices (which can be either isotropic or anisotropic) and thickness of the sample. It can also be applied to characterize the composition, surface roughness, and other material properties which could affect the sample's optical response.

In a reflection-type spectroscopic ellipsometry measurement (which is widely used for thin film characterization), the complex reflection coefficients of the s- and p-polarized incident light, r_s and r_p, are collected (**Figure 18**a). Here, s (p) refers to a polarization state whose electric field oscillates perpendicular (parallel) to the plane of incidence. Based on the recorded data, two ellipsometric parameters, Psi [$\Psi_{meas}(\lambda)$] and Delta [$\Delta_{meas}(\lambda)$], are calculated as follows

$$\tan \Psi_{meas}(\lambda) e^{i\Delta_{meas}(\lambda)} = \frac{r_p(\lambda)}{r_s(\lambda)} \tag{9}$$

Instead of directly measuring the individual change in SOP for the s- and p-polarized light upon reflection, ellipsometry measures the relative change in amplitude (in terms of Psi) and phase (in terms of Delta) between the s- and p-polarized light. Such a "self-reference" measurement excludes the need for any reference (or calibration) sample, and at the same time, can be less sensitive to factors such as intensity fluctuation of the probe beam, low intensity of the reflected light from the sample, etc. To ensure a good measurement sensitivity, the angle of incidence, θ_i, is usually set around the sample's Brewster angle (which is larger than 50° for most samples), because r_p undergoes a significant change around this angle. Moreover, sets of $\Psi_{meas}(\lambda, \theta_i)$ and $\Delta_{meas}(\lambda, \theta_i)$ are usually acquired at a few discrete θ_i for the subsequent data analysis.

A thin metal film is usually modeled as a single layer with refractive indices [$n(\lambda)$ and $k(\lambda)$] and layer thickness (d). Sets

Figure 18. a,b) Schematic representations of the "interference enhancement" (a) and "spectroscopic ellipsometry plus transmission" (b) ellipsometry measurement. The legend in (a) applies to (b).
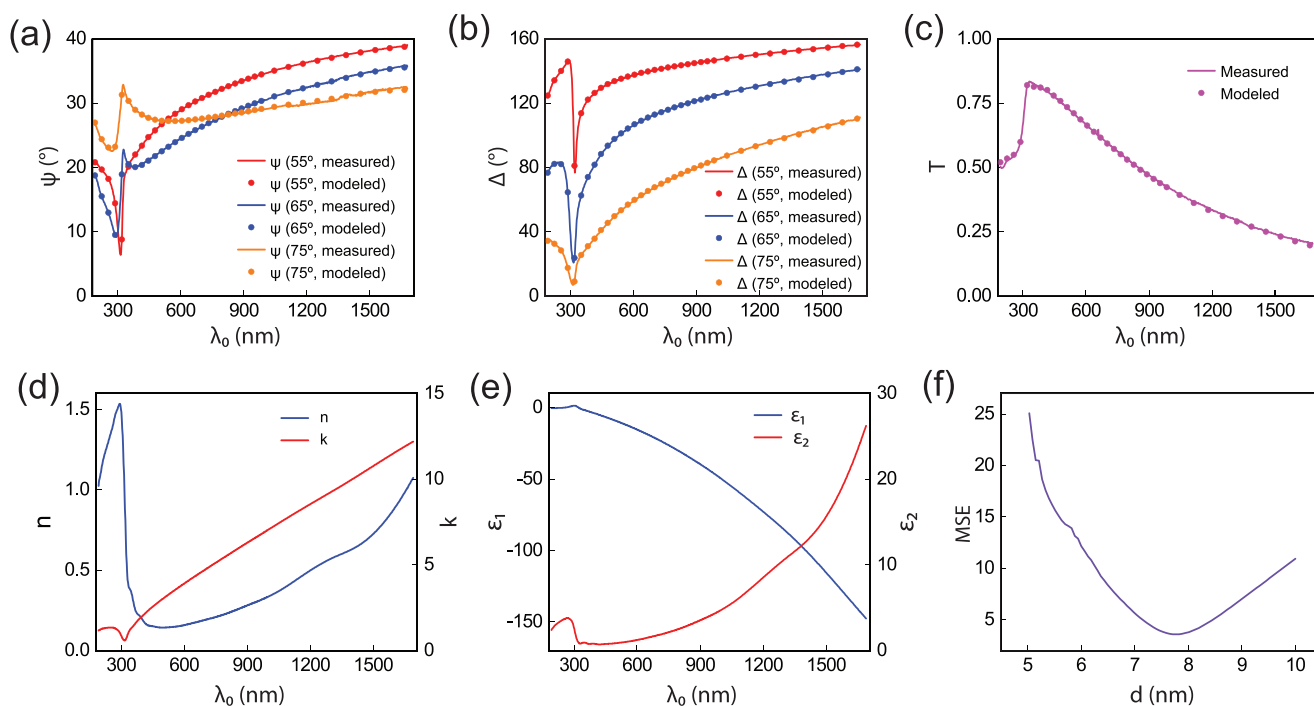
of n, k, and d (as well as other parameters for some applications, such as surface roughness, vertical composition gradient, etc.) are used to calculate the modeled Psi and Delta curves, $\Psi_{model}(\lambda, \theta_i)$ and $\Delta_{model}(\lambda, \theta_i)$. Regression analysis (such as the Levenberg–Marquardt algorithm) is employed to compare the modeled curves, $\Psi_{model}(\lambda, \theta_i)$ and $\Delta_{model}(\lambda, \theta_i)$, to the experimentally measured curves, $\Psi_{meas}(\lambda, \theta_i)$ and $\Delta_{meas}(\lambda, \theta_i)$, which yields a net mean square error (MSE). New sets of n, k, and d are iteratively generated, and the modeled and measured Psi and Delta curves are compared. Minimization of the MSE leads to a termination of the above iteration process, and determination of the film's optical properties as well as thickness value.

For characterizing an ultrathin metal film, simultaneous determination of n, k, and d can be challenging and may end up with multiple possible values. This is because for a thin metal film (which is also absorbing), its optical properties and film thickness are correlated with each other. For example, assume there are two thin metal film samples (denoted as samples #1 and #2), and ellipsometry characterization finds that sample #1 exhibits a larger optical absorption than sample #2. However, the reason could be either that sample #1 has a large absorption coefficient (k) than sample #2, or that sample #1 has a larger film thickness (d) than sample #2. To break up the above correlation, additional and independent sample information needs to be provided for the subsequent ellipsometry modeling. Solutions include "extrapolation from transparent region," "multisample analysis," "in situ analysis," "interference enhancement," and "spectroscopic ellipsometry plus transmission (SE + T)." Here, we will discuss the last two methods, which are relatively straightforward and easy to implement, and at the same time,

do not require any sample modification nor substantial reconfiguration of a standard ellipsometer.

To perform an "interference enhancement" measurement (Figure 18a), the ultrathin metal film is deposited on a Si substrate coated with a transparent dielectric layer (e.g., SiO$_2$). The substrate (with the dielectric coating) has known refractive indices and thickness values, or has been characterized by ellipsometry before the metal film deposition. During the metal film characterization, the underneath transparent dielectric layer provides extra reflected light and thus, additional information for the subsequent ellipsometry data fitting. To perform a "SE + T" measurement (Figure 18b), the ultrathin metal film is deposited on a transparent substrate (e.g., fused silica). Besides measuring the complex reflection coefficients of s- and p-polarized light at discrete angles of incidence, additional sample information is obtained by acquiring the power transmission coefficient at normal incidence, $T(\lambda)$.

Figure 19 displays the results of an ellipsometry characterization of an ≈7 nm thick Cu-doped Ag film deposited on a fused silica wafer (500 µm thick, double-side-polished), using the "SE + T" method. The dielectric functions of the Cu-doped Ag film are modeled using B-spline functions, and no surface roughness is assumed for this study. Experimental curves of $\Psi_{meas}(\lambda, \theta_i)$ and $\Delta_{meas}(\lambda, \theta_i)$ are acquired at three discrete angles of incidence: $\theta_{i=1,2,3} = 55°$, $65°$, $75°$. The measured and best-match modeled Psi and Delta curves are plotted in Figure 19a,b, respectively. The measured and best-match modeled transmission curves are plotted in Figure 19c. All measured and best-match modeled curves exhibit a close correspondence, with a MSE value of 3.584. The fitted layer thickness of the Cu-doped

Figure 19. a,b) Measured and best-match modeled Psi (a) and Delta (b) curves. c) Measured and best-modeled transmission curves. The sample is an ≈7 nm thick Cu-doped Ag film deposited on a fused silica wafer (500 µm thick, double-side-polished), and the ellipsometry characterization is performed using the "SE + T" method. d,e) Measured refractive indices (d) and relative electric permittivities (e) of the sample. f) Uniqueness test of the extracted film thickness. The point with the lowest MSE value corresponds to the best-fit film thickness value.
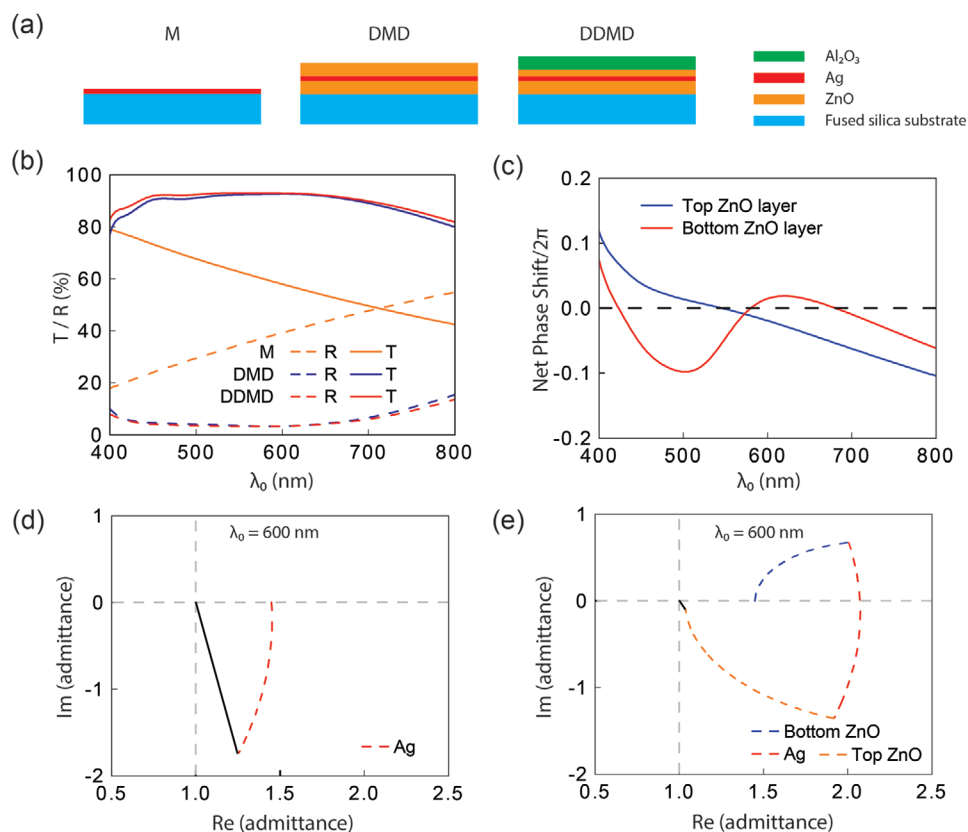
**ADVANCED
SCIENCE NEWS**

www.advancedsciencenews.com

**ADVANCED
OPTICAL
MATERIALS**

www.advopticalmat.de

Ag film is 7.77 ± 0.013 nm. The corresponding iterative-modeling-fitted refractive indices of the Cu-doped Ag film, $n(\lambda)$ and $k(\lambda)$, are plotted in Figure 19d. The corresponding relative electric permittivities, $\varepsilon_1(\lambda)$ and $\varepsilon_2(\lambda)$, are plotted in Figure 19e.

To further evaluate the robustness of the above ellipsometry characterization, along with the soundness of extracted refractive indices and thickness value, parameter uniqueness test can be performed. As an example, we perform a uniqueness test of the extracted film thickness. We first choose a set of test values around its best-fit value, and then compute the corresponding regression-analysis-fitting MSE. During the computation, the film thickness is fixed at each test value, while all other model parameters are allowed to vary. After each computation, the resulting MSE is recorded. The result of this uniqueness test is a plot of the MSE versus the predefined test film thickness values (Figure 19f). It can be seen that the MSE increases rapidly as the film thickness deviates from its best-fit value. This indicates that the ellipsometry characterization has a strong sensitivity to this parameter, and the extraction of this parameter is uniquely defined, since no other combination of the remaining fit parameters is able to produce a similar MSE. Otherwise, if the MSE is relatively insensitive to change of a test parameter, we can infer that this parameter cannot be uniquely extracted, and the analytical permittivity modeling is not robust.

5. Optical Design of Thin-Metal-Film-Based Transparent Conductors

Due to its intrinsic high reflectivity over the visible range, the transmittance through a thin metal film is largely limited. As an example, for a 10 nm thick Ag film deposited on a 500 μm thick fused silica substrate (**Figure 20**a, left panel), the corresponding averaged visible (400–800 nm) transmittance is calculated to be only 58.9% (Figure 20b). This calculation is performed using the transfer matrix method, and light is incident onto the Ag/air interface. Also, transmittance through air is defined as the reference (in other words, transmittance of 100%). For the purpose of simplicity, both the real and imaginary parts of the relative permittivity of the 10 nm thick Ag film are assumed to identical to those of a thick Ag film (plotted in Figure 3).

It is worth noting that the limited transmittance through a thin metal film (e.g., Ag, Au) is largely due to its high optical reflectance, rather than high absorption. Therefore, one widely used method to enhance the visible transmittance of a thin metal film is to add dielectric antireflection layers on both sides of the metal layer,[4,46,197–203] where the top dielectric film can simultaneously serve as a protection layer for the sandwiched metal film in many cases. For example, when the 10 nm thick

Figure 20. a) Schematic representation of transparent conductors of different geometries: single-layer metal on fused silica (denoted "M," left panel); dielectric–metal–dielectric on fused silica (denoted "DMD," middle panel); dielectric–dielectric–metal–dielectric on fused silica (denoted "DDMD," right panel). b) Calculated absolute transmission and reflection spectra of transparent conductors illustrated in (a). c) Net phase shift inside the top and bottom ZnO dielectric layers in the DMD structure. An optical resonance occurs when the net phase shift equals to 0. d,e) Admittance diagrams of the M (d) and DMD (e) structures at free-space wavelength of 600 nm. The structure's reflection intensity is proportional to the length of the black solid line, which connects the ending admittance point of the structure and air (1, 0).

**ADVANCED
SCIENCE NEWS**
www.advancedsciencenews.com

**ADVANCED
OPTICAL
MATERIALS**
www.advopticalmat.de

Ag film is sandwiched between two 40 nm thick ZnO films (Figure 20a, middle panel), the corresponding averaged visible transmittance through such a DMD structure is increased to 89.2% (Figure 20b). Similar to the earlier case, light is incident onto the interface between the top ZnO layer and air. The significantly improved transmittance over the visible range is associated with a substantially reduced reflection (from 38.3% to 6.0% by adding the two dielectric layers), which is caused by multiple optical resonances inside the two dielectric layers.[137,140] Such optical resonance occurs at a certain wavelength when the associated net phase shift inside the dielectric layer equals to multiples of 2π radians. The net phase shift inside each dielectric layer includes both reflection phase shifts at the two metal–dielectric interfaces and the propagation phase shift through the dielectric layer. For the DMD structure studied here, these resonances occur at 546 nm inside the top ZnO layer, and at discrete wavelengths of 423, 580, and 681 nm inside the bottom ZnO layer (Figure 20c).

The enhanced transmittance of the DMD structure can be explained by the admittance diagram as well. The optical admittance of a medium, Y, is defined as $Y = \sqrt{\varepsilon/\mu}$, where ε and μ are the relative permittivity and permeability, respectively. Since μ of typical materials remains unity at optical frequencies, Y equals to the material's refractive index.[204–208] The admittance of the structure in this study starts from the point (1.45, 0), which corresponds to the refractive index of fused silica substrate. By adding more layers onto the fused silica substrate, the admittance evolves accordingly. The admittance locus of a lossless dielectric ($k = 0$) or perfect electric conductor ($n = 0$) is a complete circle, while that of an absorbing material (such as semiconductor or metal, of which both n and k exhibit nonzero values) is a spiral. The reflectance of a structure, R, can be calculated by

$$R = |r|^2 = \left(\frac{Y_0 - Y_1}{Y_0 + Y_1}\right)\left(\frac{Y_0 - Y_1}{Y_0 + Y_1}\right)^* \quad (10)$$

where Y_0 and Y_1 are the admittance of the incident medium (air in this case) and the structure exit surface, respectively. The distance between the ending admittance point of structure and air (1, 0) becomes a direct measure of the structure's reflectance. Taking the admittance diagrams of the single-layer-Ag structure and DMD structure at the free-space wavelength of 600 nm as an example (Figure 20d,e), the distance between the ending point of the DMD structure and (1, 0) gets significantly reduced compared to that of the single-layer-Ag structure, clearly showing the antireflection effects of the two ZnO dielectric layers.
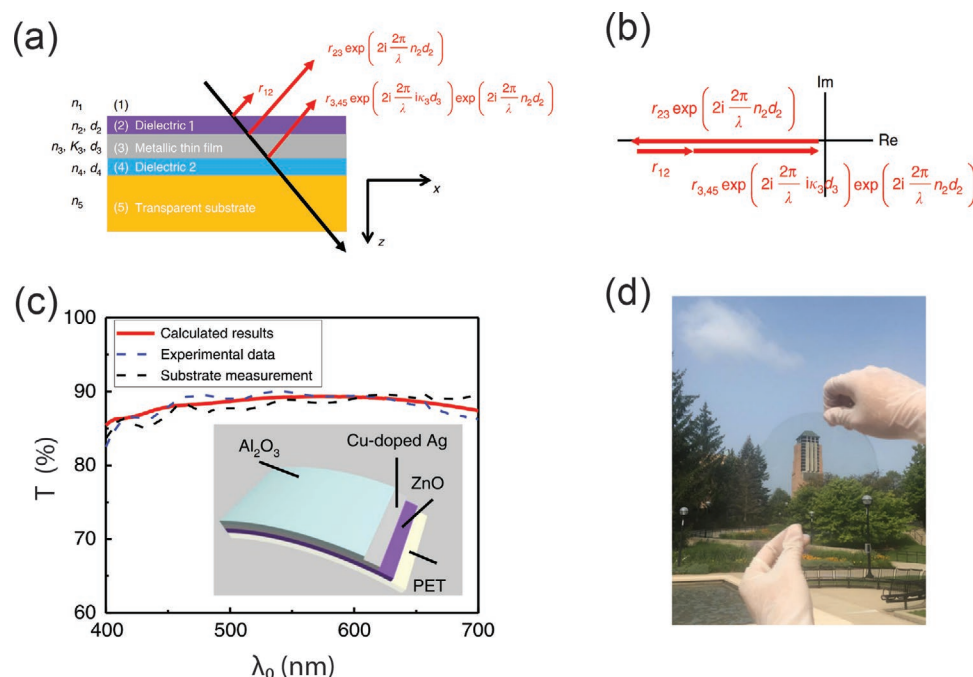
Finally, an even higher visible transmittance can be achieved by employing more dielectric antireflection coatings. For example, when adding a 40 nm thick Al_2O_3 layer on top of the ZnO layer of the DMD structure and adjusting the top ZnO layer thickness to 20 nm (Figure 20a, right panel), the corresponding averaged visible transmittance is further improved to 90.3% (Figure 20b). Such improved visible transparency is attributed to additional optical resonances inside the Al_2O_3 layer, and at the same time, a graded index profile facilitated by the Al_2O_3 layer (therefore, better index matching with air).

When light is incident on a DMD structure from the air side, the refractive indices of the entrance medium (e.g., air) and exit medium (e.g., substrate such as glass) are different. The same thing occurs when light is incident from the substrate side. Therefore, it is reasonable to infer that a DMD design with an optimized transmittance should employ different dielectric materials on each side. Unfortunately, most reported DMD structures in the literature utilize identical materials for both the top and bottom dielectric layers.[209] Recently, Ji et al. developed a quantitative design strategy for optimizing the transmittance of DMD-based transparent conductors and demonstrated devices with relative transmittance over 100%.[210] To maximize transmittance through a DMD structure with a chosen sandwiched metallic layer (as schematically illustrated in **Figure 21**a), the sum of the two reflection phase vectors from the dielectric–metal interfaces, $r_{3,45}\exp\left(2i\frac{2\pi}{\lambda_0}ik_3d_3\right)\exp\left(2i\frac{2\pi}{\lambda_0}n_2d_2\right)$ and $r_{23}\exp\left(2i\frac{2\pi}{\lambda_0}n_2d_2\right)$, needs to cancel the reflection phase vector from the top air–dielectric interference, r_{12}. Here, light is normally incident from the air side, and r_{12}, r_{23}, and $r_{3,45}$ are the complex reflection coefficients at the air–Dielectric 1 interface (1–2 interface), Dielectric 1–metal interface (2–3 interface), and metal–Dielectric 2 (3–4 interface), respectively. To maximize the transmittance through the DMD structure, the three phase vectors should be aligned along a line (Figure 21b) and satisfy the following relation

$$\left|r_{3,45}\exp\left(2i\frac{2\pi}{\lambda_0}ik_3d_3\right)\exp\left(2i\frac{2\pi}{\lambda_0}n_2d_2\right)\right| = \left|r_{23}\exp\left(2i\frac{2\pi}{\lambda_0}n_2d_2\right)\right| - |r_{12}| \quad (11)$$

Further analysis shows that to maximize the transmittance, a material of high refractive index is required for the bottom dielectric layer (Dielectric 2), and the layer thickness, d_4, is determined by $d_4 = \psi_{34}\lambda_0/4\pi n_4$. Here, ψ_{34} is the phase angle of the complex reflection coefficient, r_{34}, λ_0 is the free-space wavelength of incident light (can be the central wavelength of the wavelength band under study), and n_4 is the refractive index of the chosen dielectric material. Moreover, both the thickness and refractive index of the top dielectric layer (Dielectric 1) need to be numerically swept to achieve the best transmittance through the DMD structure. Experimentally, the authors demonstrated a DMD-based transparent conductor on a flexible polyethylene terephthalate (PET) substrate with constituent layers of a 24 nm thick ZnO film (Dielectric 2), 6.5 nm thick Cu-doped Ag film, and 65 nm thick Al_2O_3 film (Dielectric 1). The device exhibits an absolute averaged transmittance of 88.4% over the visible range (Figure 21c,d), which is higher than that of the PET substrate itself (88.1%). Moreover, it is worthwhile noting that an even higher transmittance can be achieved by replacing the bottom ZnO layer with a dielectric material of higher refractive index in the visible, such as TiO_2 and HfO_2.[211,212]

We would like to point out that a few previous reported works also mentioned the use of high-refractive-index bottom dielectric for optimizing the transmittance of DMD structures, but the associated physical mechanism was incorrectly attributed to the suppression of surface plasmon polariton (SPP) modes.[43,197,213] Although a metal–dielectric interface could support such SPP modes, these modes cannot be excited by

Figure 21. a) Schematic representation of the design parameters and wave reflection at different interfaces of the DMD-based transparent conductor. b) Phasor diagrams of the reflected waves. c) Calculated and measured absolute transmittance spectra of the designed DMD transparent conductor. The transmittance of a bare polyethylene terephthalate (PET) polymeric substrate is provided as a comparison. The inset shows the configuration of the designed DMD structure. d) Photograph of a fabricated DMD transparent conductor on a flexible PET substrate. Adapted with permission.[210] Copyright 2020, Nature Publishing Group.

a free-space incident light, unless additional coupling mechanisms (e.g., grating, prism, nanoparticle scatter, etc.) are provided. Therefore, the correct explanation for employing high-refractive-index material for the bottom dielectric layer is that such a configuration facilitates the suppression of the overall reflection from the DMD structure.
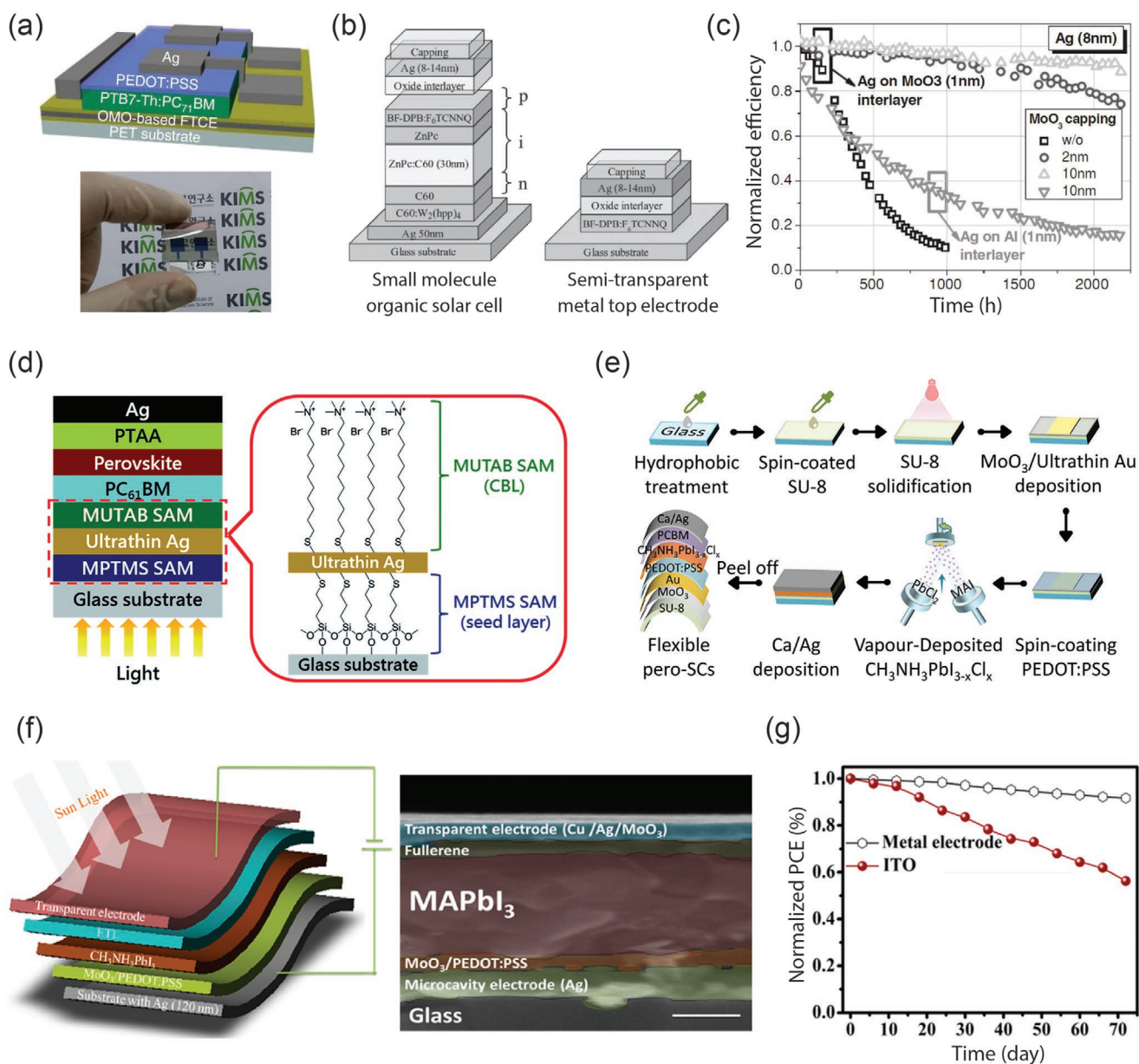
6. Device Applications

6.1. Organic Solar Cells and Perovskite Solar Cells

Organic solar cells (OSCs) have been studied extensively in recent years, and are considered as a promising future photovoltaic technology for clean energy production by their low cost, mechanical flexibility, lightweight, and large-scale manufacturing compatibility.[214–222] For OSCs, optically transparent, electrically conductive, and mechanically flexible electrodes are highly desired. Unfortunately, these requirements are not easily satisfied by the commonly used ITO electrodes. Therefore, an array of ITO-free electrodes has been explored, among which thin-metal-film-based one stands out by its high electrical conductivity, good optical transmittance, improved mechanical flexibility, and relatively straightforward preparation.[46,91,98,117,139,146,148,150,223] Many researchers have utilized different strategies of preparing high-quality ultrathin metal films (as discussed in Section 3.2) and employed the obtained thin metal layers as transparent electrodes in OSCs. For example, Zhao et al. developed thin Cu-based transparent electrodes and employed them in flexible OSCs (**Figure 22**a).[162] Through a

limited Cu oxidation process with a trace amount of oxygen, continuous and smooth Cu ultrathin films are obtained. The Cu-based transparent electrode consists of weakly oxidized Cu thin film (O/Cu ratio: ≈6%) sandwiched between ZnO films, and exhibits an average visible transmittance of 83%, a sheet resistance of $9 \, \Omega \, \square^{-1}$, and strong oxidation resistance. Schubert et al. utilized oxide/ultrathin Ag/oxide multilayers as the top semitransparent electrodes in OSCs (Figure 22b), and found that such electrodes greatly improved the stability and lifetime of small molecule OSCs (Figure 22c).[98]

Perovskite solar cells have attracted great research interest in recent years by their large carrier mobility, long carrier lifetime, adjustable bandgap, low-cost manufacturing process, high power conversion efficiency (PCE), and great commercialization potential.[224–234] So far, a majority of high-efficiency perovskite solar cells are based on electrodes using transparent conductive oxides such as ITO and fluorine doped tin oxide (FTO). However, thin-metal-film-based electrodes have gained increased attention for flexible and lightweight device applications.[235–240] Chang and co-workers demonstrated large-area, ITO-free perovskite solar cells using ultrathin Ag films (sandwiched between two SAMs) as the bottom transparent electrodes, and the devices exhibited PCEs up to 16.2% and good environmental stability (Figure 22d).[235] By coating a (3-mercaptopropyl)trimethoxysilane SAM before the Ag film deposition, the associated percolation threshold is reduced from 12 to 8 nm, and the obtained 8 nm thick Ag film exhibits a remarkably low sheet resistance of $6.1 \, \Omega \, \square^{-1}$. Xu et al. demonstrated flexible perovskite solar cells using an ultrathin (7 nm) Au electrode, facilitated by a composite wetting layer made of SU-8 polymer and MoO_3

Figure 22. a) Device architecture (upper panel) and optical photograph (lower panel) of the flexible inverted organic solar cell using a ZnO/oxidized Cu/ZnO multilayer transparent electrode. Adapted with permission.[162] Copyright 2015, Nature Publishing Group. b) Schematic representation of the small molecule OSC using oxide/ultrathin Ag/oxide multilayers as the top semitransparent electrode. c) Time development of the normalized power conversion efficiency (PCE) of the OSC at an elevated light intensity of 4 suns (400 mW cm^{-2}). Device lifetime improves as the thickness of the MoO$_3$ capping layer increases. Adapted with permission.[98] Copyright 2012, Wiley-VCH. d) Schematic representation of the perovskite solar cell using an ultrathin (8 nm) Ag film (sandwiched between two SAMs) as the bottom transparent electrode. Adapted with permission.[235] Copyright 2016, Royal Society of Chemistry. e) Fabrication process of a flexible perovskite solar cell with an ultrathin (7 nm) Au anode. Reproduced with permission.[237] Copyright 2017, Elsevier B.V. f) Left panel: schematic representation of a top-illuminated perovskite solar cell using a top semitransparent electrode made of Cu (1 nm)/Ag (10 nm)/MoO$_3$ (varying thicknesses) and a bottom electrode made of thick Ag (120 nm); right panel: cross-sectional SEM image of a representative perovskite solar cell. Scale bar: 500 nm. g) Normalized PCEs of the Ag-based and ITO-based devices with time. Both devices are stored in a N$_2$-filled glovebox. Adapted with permission.[236] Copyright 2018, American Chemical Society.

dielectric (Figure 22e).[237] After all layers have been deposited, the SU-8 layer could be peeled off from the hydrophobic glass substrate, and consequently, flexible planar perovskite solar cells are obtained. Hanmandlu et al. demonstrated top-illuminated hysteresis-free perovskite solar cells using top semitransparent electrodes made of Cu (1 nm)/Ag (10 nm)/MoO$_3$

(varying thicknesses) and bottom electrodes made of thick Ag (120 nm) (Figure 22f), and the devices exhibit enhanced PCEs and long-term stability compared to devices using ITO as the bottom electrodes (Figure 22g).[236]

For OSCs, their PCEs are highly correlated with the amount of light absorbed by the active layer. However, increasing the

**ADVANCED
SCIENCE NEWS**

www.advancedsciencenews.com

**ADVANCED
OPTICAL
MATERIALS**

www.advopticalmat.de

active layer thickness is a straightforward way to enhance light absorption, but not always an effective method to boost the device's PCE. This is because of the short exciton diffusion length and low carrier mobility in organic semiconductors, which lead to high recombination rates of photogenerated charge carriers during their transportation toward electrodes. The above physical limitation indicates that a relatively thin active layer is preferred, as long as the layer's light absorption capability is not compromised at the same time.[241–244] Toward this goal, optimizing the solar cell structure to achieve light trapping inside the photoactive layer plays an important role in realizing strong light absorption without having to increase the photoactive layer thickness. One effective and straightforward approach is to utilize thin-metal-film-based electrode to form an optical microcavity inside the OSC and to trap the incident light inside the photoactive layer.[46,96,101,139,245]
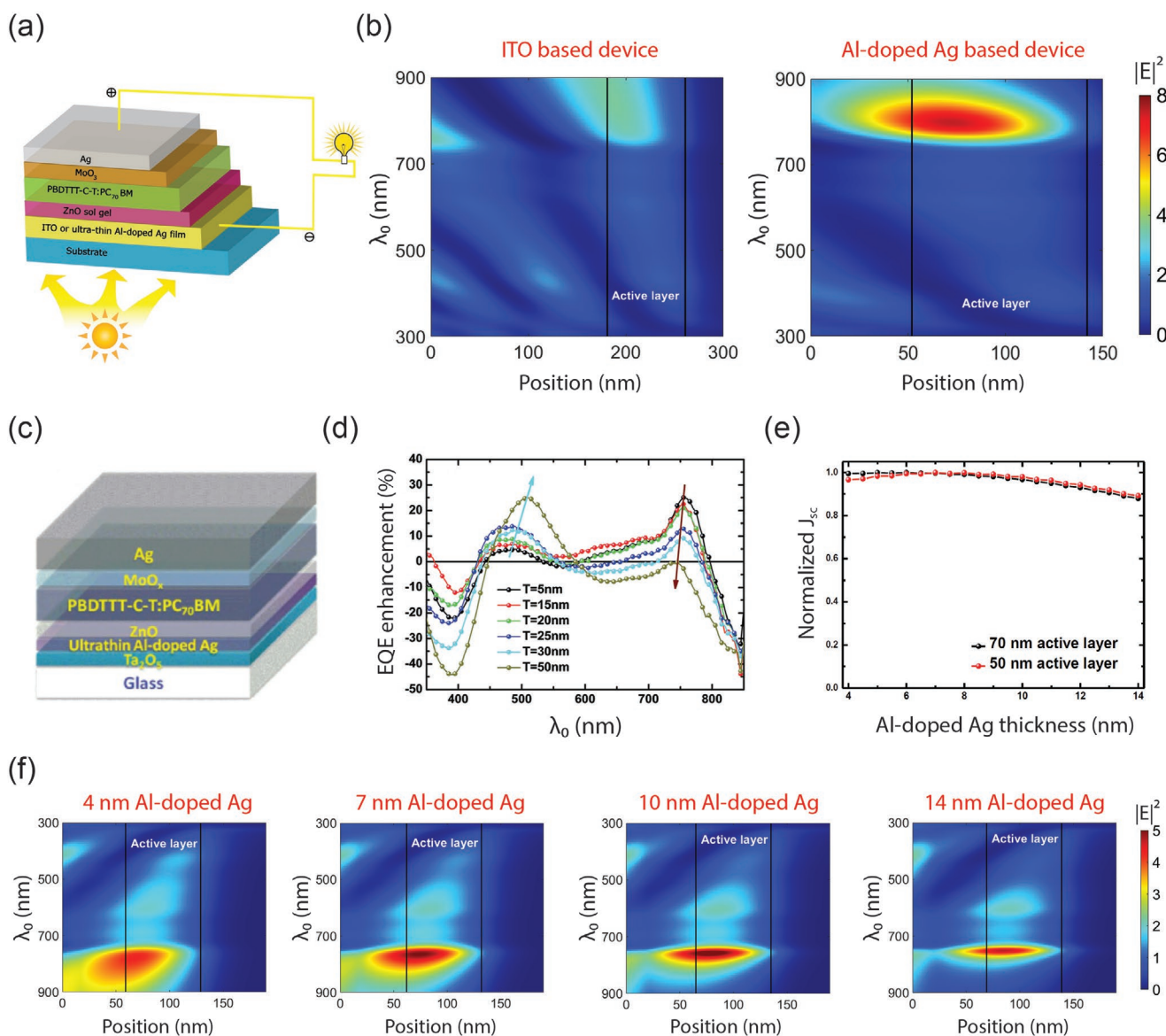
Zhang et al. employed 7 nm thick Al-doped Ag films as the bottom semitransparent electrodes in OSCs, and the devices exhibit improved PCEs compared to ITO-based ones (**Figure 23**a).[46] For the Al-doped Ag-based device, a resonant cavity is formed inside the active layer by the top reflective Ag anode and the bottom semitransparent Al-doped Ag cathode (Figure 23b). Such resonance exhibits a spectrum peak near the absorption edge of the photoactive layer material (Poly[4,8-bis-(2-ethylhexyloxy)-benzo[1,2b:4,5b0]dithiophene-2,6-diyl-alt-4-(2-ethylhexyloxy)-thieno-[3,4b]thiophene-2,6-diyl] (PBDTTT-C-T):[6,6]-phenyl C71-butyricacid methyl ester (PC$_{70}$BM)), leading to more efficient light harvesting. Based on this work, Zhao et al. inserted a Ta$_2$O$_5$ dielectric layer (with varying thicknesses) underneath the 7 nm thick Al-doped Ag electrode, while keeping other device constituent layers unchanged (Figure 23c).[139] The Ta$_2$O$_5$ layer functions as an optical spacer to tune the optical field distribution inside the entire device without the need to modify other layers' thicknesses. At the same time, the electrical characteristics of the OSC are not affected at all since this Ta$_2$O$_5$ layer is located "external" to the device's "electrical parts." With a Ta$_2$O$_5$ layer of proper thickness, the light harvesting inside the active layer is enhanced in a certain range of its absorption spectrum, while the absorption in the rest of the spectrum is not sacrificed (improved photon management), leading to an enhanced PCE (Figure 23d). The authors have further shown that the thickness of the semitransparent Al-doped Ag electrode influences the resonance effect inside the active layer in terms of both enhanced light intensity and spectrum width (Figure 23f). When the electrode gets too thin (e.g., 4 nm), the optical resonance has a broad spectrum, but a weak peak intensity. As the electrode gets thicker (e.g., 7 and 10 nm), the peak intensity gets higher, but the spectrum width is compromised. If the electrode gets even thicker (e.g., 14 nm), both the peak intensity and spectrum width are reduced due to the absorption loss associated with the metal electrode. Therefore, a balanced point needs to be identified between the spectrum width and peak intensity of the formed optical resonance. Numerical simulation of the generated photocurrent (J_{sc}) suggests that a thin Al-doped Ag electrode (between 6 and 8 nm) is most effective in optimizing the device's PCE (Figure 23e), showing the unique advantage of thin, smooth, and low-loss metal electrode for resonant light harvesting in OSCs.

6.2. Organic Light Emitting Diodes

Organic light emitting diodes (OLEDs) are considered as a leading technology for flat panel displays and eco-friendly lighting sources by their superior color quality, lightweight, low cost, and compatibility with flexible substrates.[246–251] In particular, flexible OLEDs hold great promise for the currently explosive development of bendable and wearable optoelectronic devices as well as flexible solid-state lighting.[252–256]

As an essential component of a flexible OLED, flexible transparent electrode is desired to have high optical transmittance, good electrical conductivity over large areas, robust mechanical flexibility and durability, as well as long-term stability. Unfortunately, these requirements cannot be easily fulfilled by the widely used transparent conductive oxide electrodes such as ITO. Consequently, various ITO-free flexible transparent electrodes have been explored, including metallic nanostructures,[31,34,257] carbon-based materials,[22,258,259] conductive polymers,[260,261] and thin metal films.[140] Among these candidates, thin-metal-film-based one stands out by its high electrical conductivity, good optical transmittance, improved mechanical flexibility, and large-scale manufacturing compatibility.[140,143,149,151,262] As an example, Zhang and co-workers employed 8 nm thick Ni-doped Ag films as transparent electrodes for centimeter-size flexible OLEDs (**Figure 24**a), which exhibit bending stability over 1000 circles (Figure 24b).[140] By replacing the thick ITO electrode with an ultrathin metal film, the associated waveguide modes are eliminated and therefore, the device exhibits both enhanced outcoupling efficiency and current efficiency. At the same time, because the metal electrode is so thin that the induced microcavity effect is weak, the OLED exhibits close-to-identical emission spectra at large viewing angles up to 60° (Figure 24c).

At the same time, thin-metal-film-based transparent electrodes could also benefit the light outcoupling performance of OLEDs. For bottom-emitting OLEDs, ITO-based devices suffer from limited light extraction efficiencies (≈20%), since a large portion of emitted photons are being trapped inside the device as waveguide modes. This is because of the refractive index mismatch among the organic layers ($n \approx 1.6$–1.8), ITO ($n \approx 1.8$), and substrate ($n \approx 1.5$).[263] To overcome this limitation, numerous methods have been explored, which include substituting the standard glass substrate with high-index materials ($n \geq 1.8$, for index matching with ITO),[264] patterning the ITO electrode,[265] incorporating nanostructures into the device (e.g., photonic crystals,[266] subanode grids,[267] nanoscale scatters,[268,269] bucking layers,[270] etc.), and using microlens arrays[271] or scattering films on the device emitting surfaces.[272] These approaches have demonstrated significantly enhanced light extraction efficiencies, but many of them involve complex and costly nano-/microfabrication, or are only suitable for OLEDs fabricated on rigid substrates. By contrast, thin-metal-film-based electrode provides a straightforward and low-cost solution for enhancing the outcoupling efficiencies of bottom-emitting OLEDs.[273,274] As an example, Wang and co-workers demonstrated high-efficiency phosphorescent OLEDs using an outcoupling enhancement method based on multilayer anode, which consists of a high-index Ta$_2$O$_5$ optical coupling layer, electrically conductive Au layer, and hole-injection MoO$_3$ layer (Figure 24d).[274] By
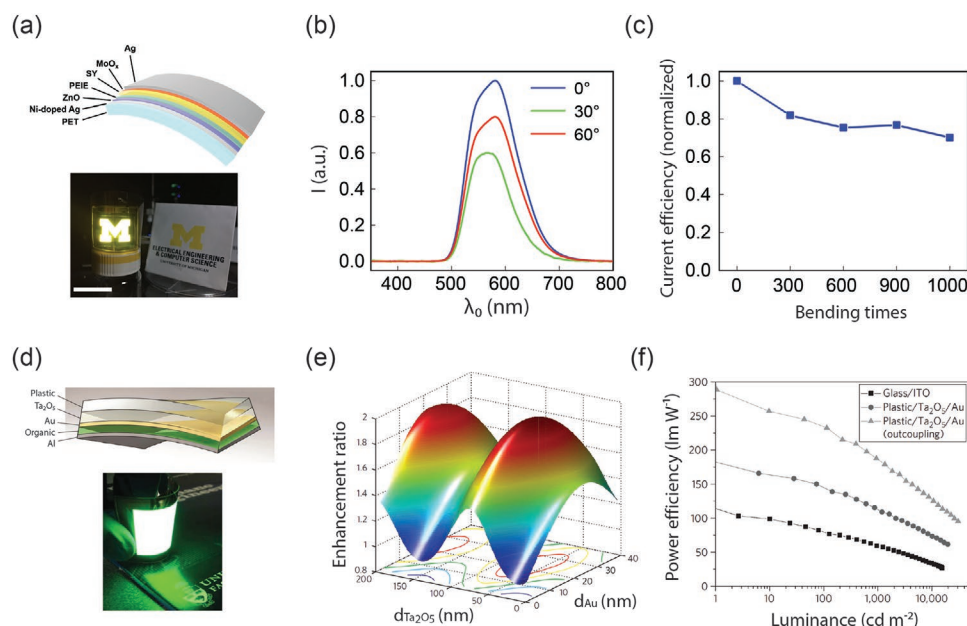
Figure 23. a) Schematic representation of the OSC with either ITO or ultrathin Al-doped Ag film as the bottom semitransparent electrode. The thicknesses of the ZnO, PBDTTT-C-T:PC$_{70}$BM, MoO$_3$, and Ag layers are 45, 90, 6, and 100 nm, respectively. b) Simulated optical field intensity ($|E|^2$) distribution versus position and wavelength in ITO-based device (left) and 7-nm Al-doped Ag-based device (right), where the enhanced optical field in the active layer around 800 nm is responsible for the enhanced PCE of the Al-doped Ag-based OSC. Adapted with permission.[46] Copyright 2014, Wiley-VCH. c) Schematic representation of the OSC using Ta$_2$O$_5$/Al-doped Ag as the electrode. The thicknesses of the ZnO, PBDTTT-C-T:PC$_{70}$BM, MoO$_3$, and Ag layers in this study are 40, 70, 10, and 100 nm, respectively. d) EQE enhancement of the Ta$_2$O$_5$ (5, 15, 20, 25, 30, and 50 nm)/Al-doped Ag (7 nm)-based OSCs over the ITO-based reference device. e) Simulated photocurrent (J_{sc}) of the devices with the Al-doped Ag electrode of varying thicknesses (from 3 to 14 nm). The thicknesses of all the other layers are fixed during the simulation. f) Simulated optical field intensity ($|E|^2$) distribution versus position and wavelength in different OSCs with Al-doped Ag electrodes of varying thicknesses. The thicknesses of the Ta$_2$O$_5$, ZnO, PBDTTT-C-T:PC$_{70}$BM, MoO$_3$, and Ag layers used in the simulation are 15, 40, 70, 10, and 100 nm, respectively. Adapted with permission.[139] Copyright 2015, Wiley-VCH.

collectively optimizing the layers' thicknesses (Figure 24e) and employing a lens-based structure to further outcouple the light trapped in the substrate, the authors achieved a peak external quantum efficiency (EQE) and power efficiency of 63% and 290 lm W^{-1}, respectively (Figure 24f). This is equivalent to an enhancement by a factor of ≈2.5 over ITO-based devices.

For top-emitting OLEDs, thin metal films have been considered as promising top semitransparent electrodes by their low-temperature preparation process and high optical transparency.[118,275,276] Usually, a dielectric capping layer is further

added on top of the metal film to further reduce the induced cavity effect and improve the viewing angle. Schwab and coworkers fabricated an ultrathin electrode with a stack architecture of Au/Ag/N,N-di(naphthalen-1-yl)-N,N-diphenyl-benzidine (NPB), where a 2 nm thick Au film acted as the wetting seed layer, while the NPB film acted as both the antireflective layer and the capping layer.[118] Benefiting from an increased optical transmittance through this multilayer Ag electrode, high-performance top-emitting white OLEDs with both a broadband emission and angular color stability were achieved.

ADVANCED
SCIENCE NEWS
www.advancedsciencenews.com

ADVANCED
OPTICAL
MATERIALS
www.advopticalmat.de

Figure 24. a) Upper panel: schematic representation of a flexible OLED using the ultrathin Ni-doped Ag-based flexible transparent electrode; lower panel: photography of a large-area OLED in the form of the University of Michigan "M" logo. The device is bent with a radius of 0.5 in., and gives both bright and uniform emission over the whole device area. Scale bar: 2 cm. b) Measured emission spectrum as a function of viewing angle for the OLED using an 8 nm thick Ni-doped Ag electrode, where the device exhibits an angle-invariant emission spectrum. c) Measured maximal current efficiencies of Ni-doped Ag-based OLED as a function of bending cycles (with a radius of 0.25 in.). The device maintains 70% of its peak efficiency after 1200 bending cycles. Adapted with permission.[140] Copyright 2019, American Chemical Society. d) Upper panel: schematic representation of the OLED device structure on low-cost flexible plastic with the $Ta_2O_5/Au/MoO_3$ electrode; lower panel: photograph of a large-area flexible OLED (50 mm × 50 mm) working at high luminance (>5000 cd m^{-2}). e) Calculated enhancement ratio of the $Ta_2O_5/Au/MoO_3$ electrode relative to ITO as a function of the thickness of both Au and Ta_2O_5. f) Power efficiencies as a function of luminance for OLEDs using different electrodes (without and with the lens-based outcoupling structure). Adapted with permission.[274] Copyright 2011, Nature Publishing Group.
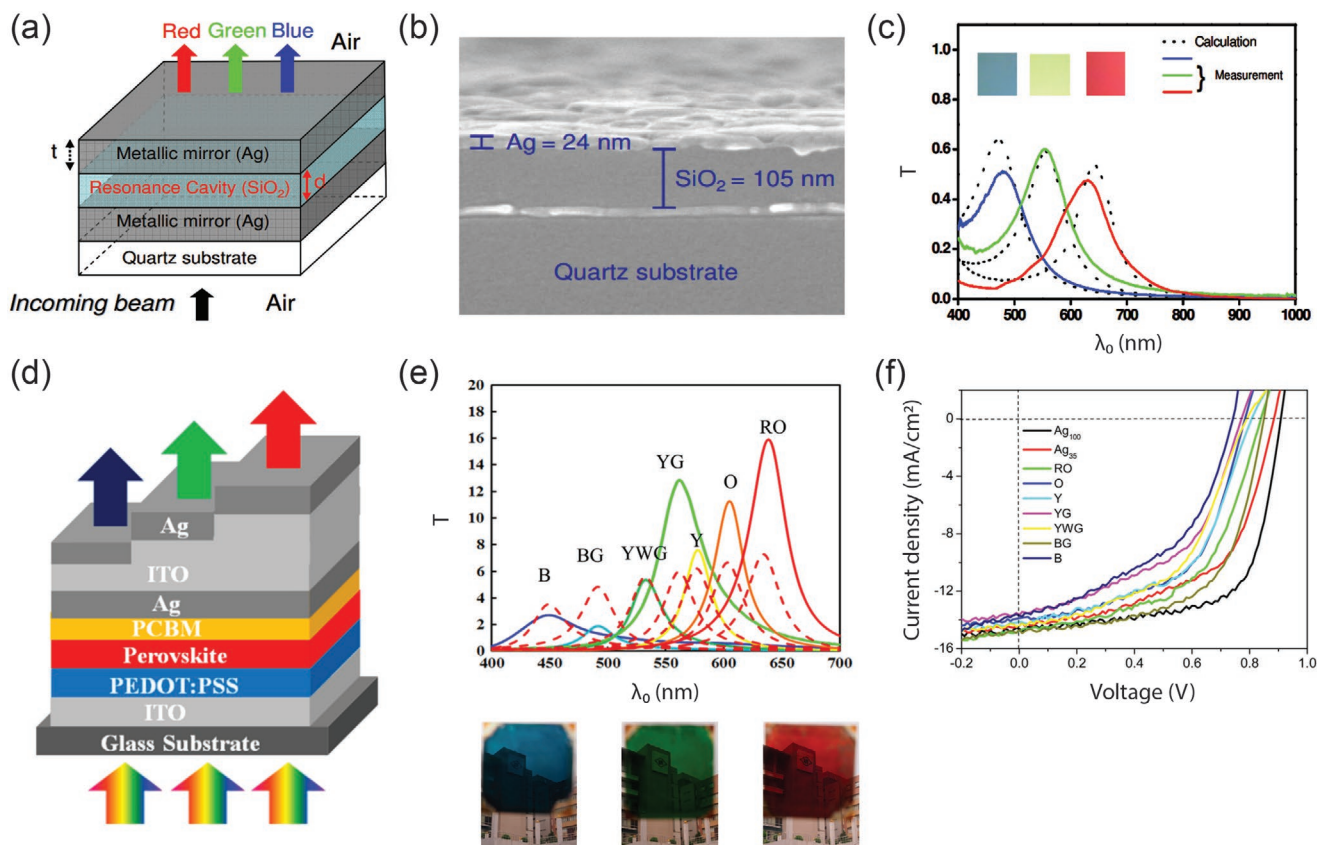
6.3. Optical Spectrum Filters

Thin metal films are also essential components in one representative category of transmissive optical spectrum filters that is based on the metal–dielectric–metal (MDM) Fabry–Pérot cavity configuration.[277–283] The schematic drawing of a MDM-based filter consisting of a dielectric layer (SiO_2) sandwiched by two thin metallic films (Ag) is shown in **Figure 25**a, and the cross-sectional SEM image of a representative device is shown in Figure 25b.[278] The thicknesses of the two Ag layers are fixed at 25 nm, and that of the SiO_2 layer varies to adjust the transmission spectrum through the DMD filter. When light is incident on the device, the transmission intensity over a certain wavelength range gets significantly enhanced by the optical resonance inside the device, which occurs when the net phase shift in the SiO_2 cavity layer equals to a multiple of 2π radians. Such phase shift consists of both the propagation phase shift accumulated inside the SiO_2 dielectric layer and two reflection phase shifts acquired upon reflection at the top and bottom metal–dielectric (Ag–SiO_2) interfaces. Consequently, by adjusting the layer thickness or material of the dielectric layer, transmission spectra of different central wavelengths can be generated. At the same time, the peak intensity and 3 dB bandwidth of the transmission spectra are largely affected by the layer thickness and material of the metallic layer. For example, when the two Ag layer thicknesses are fixed at 25 nm and the SiO_2 layer thickness is set as 100, 130, and 160 nm, respectively, the associated

transmission spectrum exhibits a peak intensity (up to 60%) at 480, 555, and 650 nm, corresponding to a high-purity blue, green, and red color, respectively (Figure 25c). In addition, the respective 3 dB bandwidths of the spectra are 120 nm (blue color), 100 nm (green color), and 120 nm (red color). It is worth noting that the transmission peak wavelength of the abovementioned Ag/SiO_2/Ag filter is sensitive to the illumination angle of the incident light, largely due to the relatively low refractive index of the employed dielectric layer (SiO_2). Filters with more robust angular responses can be implemented by using high-refractive-index dielectrics such as TiO_2 and ZnS.[279,280,284]

By its spectral filtering capability, good electrical conductivity, and large-scale manufacturing compatibility, the MDM-based filters can be employed as semitransparent electrodes in various optoelectronic devices, such as solar cells with colored appearances[285–289] and light emitting diodes with modified emission properties.[290] The schematic of a colored perovskite solar cell using a Ag/ITO/Ag top electrode is shown in Figure 25d.[285] Illumination light incident upon the bottom ITO/glass substrate is partially absorbed by the photoactive layer and then filtered by the Ag/ITO/Ag cavity, before exiting the device. By adjusting the thickness of the ITO layer sandwiched between the two 35 nm thick Ag layers, different transmission colors can be created (Figure 25e). Decent PCEs ranging from 5.7% to 7.2% have been achieved for these colored perovskite solar cells (Figure 25f).

In addition to employing the whole MDM-based filters as semitransparent electrodes in solar cell devices, colored solar

**ADVANCED
SCIENCE NEWS**

www.advancedsciencenews.com

**ADVANCED
OPTICAL
MATERIALS**

www.advopticalmat.de

Figure 25. a) Schematic representation of a transmission-type optical spectrum filter using a metal–dielectric–metal (MDM) structure. b) Cross-sectional SEM image of a fabricated device which generates blue color. c) Calculated and measured transmittance spectra of the three different samples, which generate blue, green, and red colors, respectively. Insets are photos of the fabricated devices. Adapted with permission.[278] Copyright 2010, The Optical Society. d) Schematic representation of a colored perovskite solar employing a MDM semitransparent electrode. e) Simulated (dashed lines) and measured (solid lines) transmittance spectra of the colored perovskite devices. Images of the fabricated devices are displayed in the bottom. f) Current density–potential characteristics of various colored devices under illumination with AM 1.5G solar simulated light. Adapted with permission.[285] Copyright 2016, American Chemical Society.

cells can also be implemented by structuring the whole device as a MDM filter. This is achieved by replacing the middle dielectric layer of the MDM filter with the photoactive and charge transporting layers, and at the same time, utilizing the top and bottom semitransparent metal electrodes as the two metal layers of the MDM filter.[222,291–293] Lee and co-workers demonstrated colored amorphous silicon (a-Si) solar cells using thin-Ag-film-based electrodes as both the anode and cathode (**Figure 26**a).[293] Distinct transmissive RGB colors can be generated when the thickness of the a-Si layer is set as 31, 11, and 6 nm, respectively (Figure 26b). A power conversion efficiency up to 2% is achieved (Figure 26c), and most of the absorbed photons in the undoped a-Si layer contributes to the extracted electric charges, thanks to the suppressed electron–hole recombination rate inside the ultrathin a-Si layer.
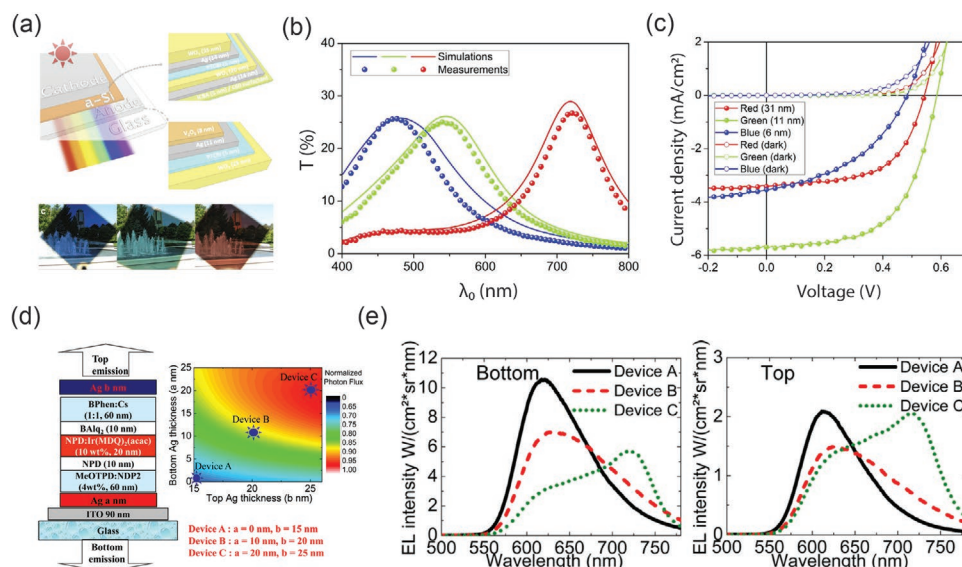
Similar strategies have been utilized to implement semitransparent LED devices.[294–297] Lee and co-workers demonstrated a group of bidirectional OLEDs using Ag-based cathodes and ITO/Ag-based anodes (Figure 26d; Device A: 15 nm Ag cathode and 90 nm ITO/0 nm Ag anode; Device B: 20 nm Ag cathode and 90 nm ITO/10 nm Ag anode; Device C: 25 nm Ag cathode and 90 nm ITO/10 nm Ag anode). For OLED without

the Ag layer in the bottom anode (Device A), its emission peak wavelength is located at ≈617 nm, close to the photoluminescence peak wavelength (≈606 nm) of the light emitting layer. By inserting a thin Ag film on top of the bottom ITO layer (Devices B and C), the entire OLED structure becomes an effective MDM cavity and the corresponding emission spectra from both the top and bottom sides are apparently modified by the induced cavity effect (Figure 26e).

6.4. Low-Emissivity Coatings

Low-emissivity (low-E) coatings are usually applied on architectural windows to minimize the amount of UV and infrared (IR) light that can pass through, without compromising the windows' visible transmittance.[298] Low-E coatings help to improve the windows' thermal insulating and solar energy shielding capabilities. During a cold weather, a low-E coating prevents the radiant heat from escaping out of the window; while during a hot weather, it blocks the solar heat from entering into the building.

Different designs have been proposed for low-E coatings, including photonic crystals,[299] metal nanoparticles,[300] and

ADVANCED
SCIENCE NEWS
www.advancedsciencenews.com

ADVANCED
OPTICAL
MATERIALS
www.advopticalmat.de

Figure 26. a) Upper panel: schematic representation of the colored amorphous silicon (a-Si) solar cell using thin-Ag-film-based electrodes as both the anode and cathode; lower panel: photographs of the fabricated colored solar cells. b) Calculated and measured transmittance spectra of the colored solar cells. The thicknesses of the a-Si layer are 6, 11, and 31 nm for the blue, green, and red colored devices, respectively. c) Current density–voltage characteristics of the solar cells under AM 1.5 illumination and dark conditions. Adapted with permission.[293] Copyright 2014, Nature Publishing Group. d) Device structures and photon flux simulation results (the sum of both directions) of the bidirectional OLEDs using ITO/Ag-based anodes and Ag-based cathodes. e) Electroluminescence (EL) spectra from the bottom side (left panel) and top side (right panel) of the three OLED devices, using the same driving current of 1 mA. Adapted with permission.[294] Copyright 2011, AIP Publishing LLC.
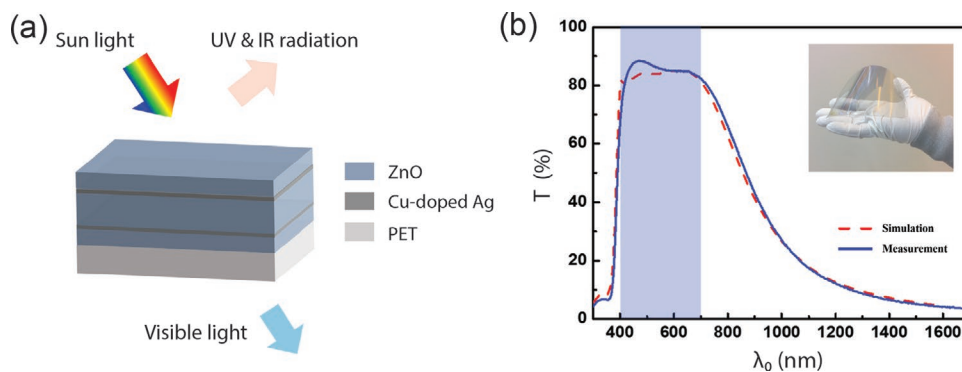
thin metal films.[167,168,301–302] Among them, thin-metal-film-based low-E coatings stand out by their simple design and compatibility with mass production. The relation between its reflection of IR radiation and electrical conductivity of a conducting material is given by the Hagen–Rubens relation[303,304]

$$R \approx 1 - 2\sqrt{\frac{2\varepsilon_0 w}{\sigma}} \qquad (12)$$

where w is the frequency of the IR radiation, ε_0 is the permittivity of vacuum, and σ is the material's electrical conductivity. Under a simplified consideration, σ is frequency-independent and equal to the material's DC conductivity. The Hagen–Rubens relation indicates that metals with large electrical conductivity

are good reflectors in the IR region. By its lowest DC conductivity among metals, Ag exhibits the best IR shielding capability. More importantly, Ag also has the lowest optical loss over the visible range, which guarantees a high visible transmittance. Consequently, a majority of low-E coatings are based on Ag films or Ag/dielectric multilayer structures.

Zhang et al. demonstrated large-area (6 in. in diameter) low-E coatings deposited on flexible PET substrates (**Figure 27**a).[140] The coating consists of stacks of ZnO and Cu-doped Ag layers (75 nm ZnO/8 nm Cu-doped Ag/30 nm ZnO/8 nm Cu-doped Ag/75 nm ZnO). The constituent Cu-doped Ag films effectively suppress the coating's IR transmission by their high IR reflectivity. At the same time, three ZnO dielectric layers help to create optical resonances at different wavelengths across the visible

Figure 27. a) Schematic representation of a low-E coating which transmits a large percentage of the visible light, while blocks both UV and IR radiation. The sample consists of 75 nm ZnO/8 nm Cu-doped Ag/30 nm ZnO/8 nm Cu-doped Ag/75 nm ZnO on a PET substrate. b) Simulated (dashed red line) and measured (solid blue line) transmittance through the low-E coating. The visible transmission window is denoted by the shaded blue area. The inset shows the photo of a 6 in. sample. Reproduced with permission.[140] Copyright 2019, American Chemical Society.

**ADVANCED
SCIENCE NEWS**

www.advancedsciencenews.com

**ADVANCED
OPTICAL
MATERIALS**

www.advopticalmat.de

range, inducing a broadband and high visible transparency. The thickness of each individual ZnO layer is carefully optimized to ensure a high and flat transmittance between 400 and 700 nm. The device exhibits an averaged 85.2% visible transmittance (400–700 nm). At the same time, there is a minimal transmittance for UV light, and the transmittance in the IR region drops under 10% beyond 1250 nm (Figure 27b). Moreover, the low-E coating exhibits a neutral color appearance, making it highly desirable for window applications. When evaluated in the International Commission on Illumination (CIE) *L*a*b** color space, the coating's transmission spectrum corresponds to a *L** value of 95.7 (meaning close to diffusive white), and *a** (*b**) value of −0.01 (0.42) (meaning neutral color appearance). Compared to previous work utilizing Ag/dielectric multilayer structures, this work utilizes ultrathin and low-loss doped Ag films, which not only guarantees the coating's high visible transparency, but at the same time, maintains the coating's neutral-color appearance.

One important thing to consider is the stability of low-E coatings, as they are often applied on the building windows and need to withstand harsh environment conditions. Many strategies discussed in Section 3.3 have been utilized to enhance the stability of these coatings. Also, low-E coatings are usually packed with desiccant during their storage and transport, and are properly shielded inside the glass windows after installation.

6.5. Transparent Electromagnetic Interference Shielding Coatings

Radio frequency (RF) electromagnetic waves have been increasingly employed in diverse applications such as telecommunications and wearable electronics in recent years. While at the same time, the associated electromagnetic energy pollution has also been gaining an increased attention. Such electromagnetic interference (EMI) could lead to malfunction of electronic devices, and exposure to intensive electromagnetic radiation is believed to hazardous to human health.[305,306] Consequently, EMI shielding technology plays a vital role for maintaining an appropriate operation condition for sensitive electronic devices and a healthy living environment for human beings.[307–309]

For many EMI shielding applications, the shielding coatings are desired to be optically transparent and mechanically flexible. This facilitates their easy integration into existing optoelectronic systems such as displays, mobile devices, smart windows, etc. Toward this goal, various designs have been exploited, including carbon-based materials,[310–312] metal meshes and nanowires,[313–315] and thin metal films.[92,202,316] Compared to other candidates, thin metal films exhibit unique advantages of simple structure and large-scale manufacturing compatibility, and therefore, have been gaining increased attention in recent years. For example, Maniyara et al. demonstrated DMD-based transparent EMI shielding coatings on silica substrate (**Figure 28**a).[92] By choosing a 12 nm thick Ag film as the sandwiched metallic layer and optimizing the thicknesses of the top (AZO) and bottom (TiO₂) dielectric layers, the coating exhibits an averaged visible transmittance of 91.6% (Figure 28b) and shielding of RF and microwave interference signals with ≈30 dB attenuation up to 18 GHz (Figure 28c). Wang et al. demonstrated flexible EMI shielding coatings with a DMD structure of ITO (40 nm)/ Cu-doped Ag (8 nm)/ITO (40 nm).[202] The coating transmits
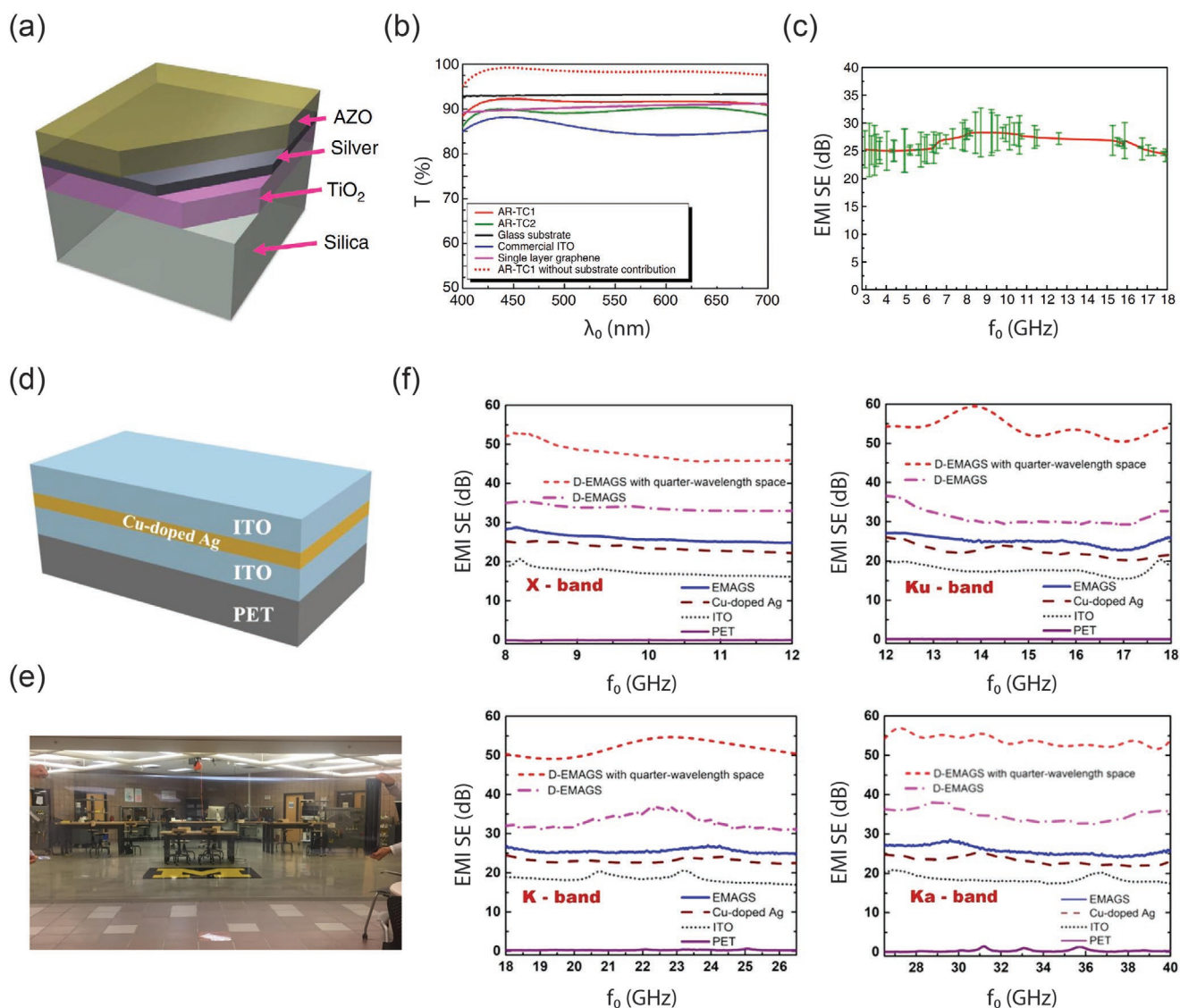
96.5% visible light relative to the substrate (Figure 28d) and shows an excellent average EMI shielding effectiveness (SE) of ≈26 dB, over a broad bandwidth of 32 GHz, covering the entire X, Ku, Ka, and K bands (Figure 28e). By adding a monolayer graphene on the backside of the substrate, they were able to further increase the structure's RF absorption without scarifying much of its visible transparency.[316]

7. Conclusions and Outlook

This review summarizes some key concepts and recent achievements of thin-metal-film-based transparent conductors. A few strategies are identified for preparing a high-performance thin-metal-film-based conductor, which include: i) choosing a constituent metal with low optical loss; ii) optimizing the metal film's structural morphology; iii) reducing the optical absorption or reflection of the transparent conductor. By their highest electrical conductivity and lowest optical loss among metals, Ag, Au, and Cu stand out as promising candidates for thin-metal-film-based transparent conductors. However, fabricating high-quality, ultrathin films using these metals is challenging, due to the metal atom's intrinsic Volmer–Weber (3D) growth mechanism. Consequently, various fabrication techniques have been explored, including dielectric wetting layer, metallic wetting layer, metal doping, molecular surfactant, polymer surfactant, and deposition condition optimization. The optical properties and thickness values of the fabricated thin metal films can be reliably characterized using the spectroscopic ellipsometry method.

The transmittance through a single-layer metal film is still limited, largely due to its high optical reflection. One effective approach to mitigating the above limitation is to employ antireflection dielectric coatings atop and beneath the metal film, forming a DMD structure. This review discusses the relevant strategies for choosing the appropriate dielectric layers and procedures of designing DMD-based conductors with optimized transmittance. By their high electrical conductivity over large areas, good optical transmittance, low haze, and compatibility with large-scale manufacturing, thin-metal-film-based transparent conductors and their derivatives have been increasingly employed in various optoelectronic devices such as solar cells, light emitting diodes, optical filters, low-emissivity windows, and transparent electromagnetic interference shielding coatings.

Although an array of fabrication techniques for obtaining high-quality metal films has been demonstrated, a large portion of these reported methods are described empirically without a consistent theoretical guideline. The metal film deposition is a very complicated process, which is not only influenced by the employed "wetting" layer, but also highly affected by numerous deposition tool factors such as vacuum level, deposition power, gas ratio, chamber impurity, etc. Future development in both experimental characterization techniques and computational modeling capabilities could help to get a deeper understanding of the wetting-layer's mechanism and facilitate the development of universal guidelines for preparing ultrathin metal films. Also, combining two or more "wetting mechanisms" could help to further reduce the associated percolation thresholds and obtain thin-metal-film-based transparent conductors of enhanced optoelectronic performance. Finally, the constantly

Figure 28. a) Schematic representation of the DMD-based transparent EMI shielding coating on a silica substrate. b) Measured transmission spectrum of the DMD-based transparent EMI shielding coating. The transmission spectra of a bared fused silica substrate, single-layer graphene, and commercial ITO are also plotted for comparison. c) Measured shielding effectiveness (SE) of the coating. Adapted with permission.[92] Copyright 2016, Nature Publishing Group. d) Schematic representation of a flexible transparent EMI shielding coating with a DMD structure of ITO (40 nm)/Cu-doped Ag (8 nm)/ITO (40 nm). e) Photo of a large-area ($\approx 200 \times 50$ cm^2) flexible sample. f) Measured EMI SE results of the flexible transparent EMI shielding coating over the X band (8–12 GHz), Ku band (12–18 GHz), K band (18–26.5 GHz), and Ka band (26.5–40 GHz). Adapted with permission.[202] American Chemical Society.

emerging novel concepts and applications of optoelectronic devices motivate the research community to develop thin-metal-film-based transparent conductors with even lower optical loss, higher electrical conductivity, better mechanical flexibility, robust operational stability, and multiple functionality.

Acknowledgements

Conflict of Interest

C.Z. and L.J.G. declared financial interest in the ultrathin metal-based transparent conductor technology.

[1] M. Morales-Masis, S. De Wolf, R. Woods-Robinson, J. W. Ager, C. Ballif, *Adv. Electron. Mater.* **2017**, *3*, 1600529.

[2] D. S. Ginley, H. Hosono, D. C. Paine, *Handbook of Transparent Conductors*, Springer US, New York **2010**.

[3] R. G. Gordon, *MRS Bull.* **2000**, *25*, 52.

[4] W. Cao, J. Li, H. Chen, J. Xue, *J. Photonics Energy* **2014**, *4*, 040990.

[5] D. R. Cairns, R. P. Witte II, D. K. Sparacin, S. M. Sachsman, D. C. Paine, G. P. Crawford, R. R. Newton, *Appl. Phys. Lett.* **2000**, *76*, 1425.

[6] M. T. Dang, J. Lefebvre, J. D. Wuest, *ACS Sustainable Chem. Eng.* **2015**, *3*, 3373.

[7] A. M. Alfantazi, R. R. Moskalyk, *Miner. Eng.* **2003**, *16*, 687.

[8] M. Nasr Saleh, G. Lubineau, *Sol. Energy Mater. Sol. Cells* **2014**, *130*, 199.

[9] J. W. Park, G. Kim, S. H. Lee, E. H. Kim, G. H. Lee, *Surf. Coat. Technol.* **2010**, *205*, 915.

[10] E. H. Kim, C. W. Yang, J. W. Park, *J. Appl. Phys.* **2011**, *109*, 043511.

[11] J. H. Kim, H. J. Seok, H. J. Seo, T. Y. Seong, J. H. Heo, S. H. Lim, K. J. Ahn, H. K. Kim, *Nanoscale* **2018**, *10*, 20587.

[12] N. Straue, M. Rauscher, M. Dressler, A. Roosen, *J. Am. Ceram. Soc.* **2012**, *95*, 684.

[13] R. E. Triambulo, J. H. Kim, M. Y. Na, H. J. Chang, J. W. Park, *Appl. Phys. Lett.* **2013**, *102*, 241913.

[14] D. Singh, R. Tao, G. Lubineau, *npj Flexible Electron.* **2019**, *3*, 10.

[15] J. Liu, Y. Yi, Y. Zhou, H. Cai, *Nanoscale Res. Lett.* **2016**, *11*, 108.

[16] H. G. Im, S. Jeong, J. Jin, J. Lee, D. Y. Youn, W. T. Koo, S. B. Kang, H. J. Kim, J. Jang, D. Lee, H. K. Kim, I. D. Kim, J. Y. Lee, B. S. Bae, *NPG Asia Mater.* **2016**, *8*, e282.

[17] J. H. Yoo, Y. Kim, M. K. Han, S. Choi, K. Y. Song, K. C. Chung, J. M. Kwak, J. Kim, *ACS Appl. Mater. Interfaces* **2015**, *7*, 15928.

[18] J. Lewis, S. Grego, B. Chalamala, E. Vick, D. Temple, *Appl. Phys. Lett.* **2004**, *85*, 3450.

[19] M. Vosgueritchian, D. J. Lipomi, Z. Bao, *Adv. Funct. Mater.* **2012**, *22*, 421.

[20] Y. Wang, C. Zhu, R. Pfattner, H. Yan, L. Jin, S. Chen, F. Molina-Lopez, F. Lissel, J. Liu, N. I. Rabiah, Z. Chen, J. W. Chung, C. Linder, M. F. Toney, B. Murmann, Z. Bao, *Sci. Adv.* **2017**, *3*, e1602076.

[21] D. Gupta, M. M. Wienk, R. A. J. Janssen, *Adv. Energy Mater.* **2013**, *3*, 782.

[22] Y. Xu, J. Liu, *Small* **2016**, *12*, 1400.

[23] D. S. Hecht, L. Hu, G. Irvin, *Adv. Mater.* **2011**, *23*, 1482.

[24] S. Jiang, P. X. Hou, M. L. Chen, B. W. Wang, D. M. Sun, D. M. Tang, Q. Jin, Q. X. Guo, D. D. Zhang, J. H. Du, K. P. Tai, J. Tan, E. I. Kauppinen, C. Liu, H. M. Cheng, *Sci. Adv.* **2018**, *4*, eaap9264.

[25] Y. Wang, S. W. Tong, X. F. Xu, B. Özyilmaz, K. P. Loh, *Adv. Mater.* **2011**, *23*, 1514.

[26] M.-G. Kang, H. J. Park, S. H. Ahn, L. J. Guo, *Sol. Energy Mater. Sol. Cells* **2010**, *94*, 1179.

[27] M. G. Kang, T. Xu, H. J. Park, X. Luo, L. J. Guo, *Adv. Mater.* **2010**, *22*, 4378.

[28] M. G. Kang, L. J. Guo, *Adv. Mater.* **2007**, *19*, 1391.

[29] S. Hong, J. Yeo, G. Kim, D. Kim, H. Lee, J. Kwon, H. Lee, P. Lee, S. H. Ko, *ACS Nano* **2013**, *7*, 5024.

[30] J. H. Park, D. Y. Lee, Y. H. Kim, J. K. Kim, J. H. Lee, J. H. Park, T. W. Lee, J. H. Cho, *ACS Appl. Mater. Interfaces* **2014**, *6*, 12380.

[31] C. Zhang, A. Khan, J. Cai, C. Liang, Y. Liu, J. Deng, S. Huang, G. Li, W. D. Li, *ACS Appl. Mater. Interfaces* **2018**, *10*, 21009.

[32] A. Kumar, C. Zhou, *ACS Nano* **2010**, *4*, 11.

[33] H. Lu, X. Ren, D. Ouyang, W. C. H. Choy, *Small* **2018**, *14*, 1703140.

[34] H. Wu, D. Kong, Z. Ruan, P.-C. Hsu, S. Wang, Z. Yu, T. J. Carney, L. Hu, S. Fan, Y. Cui, *Nat. Nanotechnol.* **2013**, *8*, 421.

[35] J. Y. Lee, S. T. Connor, Y. Cui, P. Peumans, *Nano Lett.* **2008**, *8*, 689.

[36] C. H. Liu, X. Yu, *Nanoscale Res. Lett.* **2011**, *6*, 75.

[37] C. Zhang, J. Cai, C. Liang, A. Khan, W. D. Li, *Adv. Funct. Mater.* **2019**, *29*, 1903123.

[38] B. Bari, J. Lee, T. Jang, P. Won, S. H. Ko, K. Alamgir, M. Arshad, L. J. Guo, *J. Mater. Chem. A* **2016**, *4*, 11365.

[39] B. Han, Y. Huang, R. Li, Q. Peng, J. Luo, K. Pei, A. Herczynski, K. Kempa, Z. Ren, J. Gao, *Nat. Commun.* **2014**, *5*, 5674.

[40] B. Han, K. Pei, Y. Huang, X. Zhang, Q. Rong, Q. Lin, Y. Guo, T. Sun, C. Guo, D. Carnahan, M. Giersig, Y. Wang, J. Gao, Z. Ren, K. Kempa, *Adv. Mater.* **2014**, *26*, 873.

[41] B. Han, Q. Peng, R. Li, Q. Rong, Y. Ding, E. M. Akinoglu, X. Wu, X. Wang, X. Lu, Q. Wang, G. Zhou, J. M. Liu, Z. Ren, M. Giersig, A. Herczynski, K. Kempa, J. Gao, *Nat. Commun.* **2016**, *7*, 12825.

[42] J. Gao, Z. Xian, G. Zhou, J. M. Liu, K. Kempa, *Adv. Funct. Mater.* **2018**, *28*, 1705023.

[43] Y. G. Bi, Y. F. Liu, X. L. Zhang, D. Yin, W. Q. Wang, J. Feng, H. B. Sun, *Adv. Opt. Mater.* **2019**, *7*, 1800778.

[44] B. O'Connor, C. Haughn, K.-H. An, K. P. Pipe, M. Shtein, *Appl. Phys. Lett.* **2008**, *93*, 223304.

[45] J. Yun, *Adv. Funct. Mater.* **2017**, *27*, 1606641.

[46] C. Zhang, D. Zhao, D. Gu, H. Kim, T. Ling, Y. K. R. Wu, L. J. Guo, *Adv. Mater.* **2014**, *26*, 5696.

[47] D. S. Ghosh, *Ultrathin Metal Transparent Electrodes for the Optoelectronics Industry*, Springer International Publishing, Switzerland **2013**.

[48] R. Lemasters, C. Zhang, M. Manjare, W. Zhu, J. Song, S. Urazhdin, H. J. Lezec, A. Agrawal, H. Harutyunyan, *ACS Photonics* **2019**, *6*, 2600.

[49] S. Kosuga, R. Suga, O. Hashimoto, S. Koh, *Appl. Phys. Lett.* **2017**, *110*, 233102.

[50] J. K. Wassei, R. B. Kaner, *Mater. Today* **2010**, *13*, 52.

[51] F. S. F. Morgenstern, D. Kabra, S. Massip, T. J. K. Brenner, P. E. Lyons, J. N. Coleman, R. H. Friend, *Appl. Phys. Lett.* **2011**, *99*, 183307.

[52] R. A. Serway, J. R. Gordon, *Principles of Physics*, Saunders College Publishing, Philadelphia, PA, USA **1998**.

[53] Electrical resistivity and conductivity, https://en.wikipedia.org/wiki/Electrical_resistivity_and_conductivity (accessed: November 2020).

[54] D. Gall, *J. Appl. Phys.* **2016**, *119*, 085101.

[55] K. Fuchs, *Math. Proc. Cambridge Philos. Soc.* **1938**, *34*, 100.

[56] E. H. Sondheimer, *Adv. Phys.* **1952**, *1*, 1.

[57] S. B. Soffer, *J. Appl. Phys.* **1967**, *38*, 1710.

[58] T. Sun, B. Yao, A. P. Warren, K. Barmak, M. F. Toney, R. E. Peale, K. R. Coffey, *Phys. Rev. B* **2010**, *81*, 155454.

[59] M. A. Angadi, *J. Mater. Sci.* **1985**, *20*, 761.

[60] J. R. Sambles, K. C. Elsom, *J. Phys. D: Appl. Phys.* **1982**, *15*, 1459.

[61] P. Martin, *Electrical Transport and Scattering Mechanisms in Thin Silver Films for Thermally Insulating Glazing*, Ph.D. Thesis, TU Dresden **2011**, http://nbn-resolving.de/urn:nbn:de:bsz:14-qucosa-70920.

[62] A. F. Mayadas, M. Shatzkes, *Phys. Rev. B* **1970**, *1*, 1382.

[63] A. F. Mayadas, M. Shatzkes, J. F. Janak, *Appl. Phys. Lett.* **1969**, *14*, 345.

[64] D. Ebner, M. Bauch, T. Dimopoulos, *Opt. Express* **2017**, *25*, A240.

[65] J. H. Yun, N. Duraisamy, M. M. D. Kumar, J. Kim, *Mater. Lett.* **2015**, *143*, 215.

[66] Y. Li, Y. Chen, M. Qiu, H. Yu, X. Zhang, X. W. Sun, R. Chen, *Sci. Rep.* **2016**, *6*, 20114.

ADVANCED
SCIENCE NEWS

www.advancedsciencenews.com

ADVANCED
OPTICAL
MATERIALS

www.advopticalmat.de

[67] S. P. Cho, S. I. Na, S. S. Kim, *Sol. Energy Mater. Sol. Cells* **2019**, *196*, 1.

[68] D. S. Ghosh, L. Martinez, S. Giurgola, P. Vergani, V. Pruneri, *Opt. Lett.* **2009**, *34*, 325.

[69] L. Martínez, D. S. Ghosh, S. Giurgola, P. Vergani, V. Pruneri, *Opt. Mater.* **2009**, *31*, 1115.

[70] D. W. Lynch, W. R. Hunter, in *Handbook of Optical Constants of Solids*, (Ed: E. D. Palik), Academic Press, Burlington **1997**, pp. 275–367.

[71] I. Lee, J. L. Lee, *J. Photonics Energy* **2015**, *5*, 057609.

[72] D. B. Fraser, H. D. Cook, *J. Electrochem. Soc.* **1972**, *119*, 1368.

[73] G. Haacke, *J. Appl. Phys.* **1976**, *47*, 4086.

[74] P. B. Johnson, R. W. Christy, *Phys. Rev. B* **1972**, *6*, 4370.

[75] N. Kaiser, *Appl. Opt.* **2002**, *41*, 3053.

[76] A. W. Adamson, A. P. Gast, *Physical Chemistry of Surfaces*, Wiley, New York **1997**.

[77] S. H. Overbury, P. A. Bertrand, G. A. Somorjai, *Chem. Rev.* **1975**, *75*, 547.

[78] R. Sangiorgi, M. L. Muolo, D. Chatain, N. Eustathopoulos, *J. Am. Ceram. Soc.* **1988**, *71*, 742.

[79] C. T. Campbell, *Surf. Sci. Rep.* **1997**, *27*, 1.

[80] H. Han, N. D. Theodore, T. L. Alford, *J. Appl. Phys.* **2008**, *103*, 013708.

[81] H. W. Choi, N. D. Theodore, T. L. Alford, *Sol. Energy Mater. Sol. Cells* **2013**, *117*, 446.

[82] H. M. Lee, Y. J. Lee, I. S. Kim, M. S. Kang, S. B. Heo, Y. S. Kim, D. Kim, *Vacuum* **2012**, *86*, 1494.

[83] T. Dimopoulos, G. Z. Radnoczi, B. Pécz, H. Brückl, *Thin Solid Films* **2010**, *519*, 1470.

[84] D. R. Sahu, S. Y. Lin, J. L. Huang, *Thin Solid Films* **2008**, *516*, 4728.

[85] I. Crupi, S. Boscarino, V. Strano, S. Mirabella, F. Simone, A. Terrasi, *Thin Solid Films* **2012**, *520*, 4432.

[86] S. W. Cho, J. A. Jeong, J. H. Bae, J. M. Moon, K. H. Choi, S. W. Jeong, N. J. Park, J. J. Kim, S. H. Lee, J. W. Kang, M. S. Yi, H. K. Kim, *Thin Solid Films* **2008**, *516*, 7881.

[87] J. A. Jeong, Y.-S. Park, H. K. Kim, *J. Appl. Phys.* **2010**, *107*, 023111.

[88] H. J. Lee, J. W. Kang, S. H. Hong, S. H. Song, S. J. Park, *ACS Appl. Mater. Interfaces* **2016**, *8*, 1565.

[89] H. K. Park, J. W. Kang, S. I. Na, D. Y. Kim, H. K. Kim, *Sol. Energy Mater. Sol. Cells* **2009**, *93*, 1994.

[90] A. Dhar, T. L. Alford, *APL Mater.* **2013**, *1*, 012102.

[91] D. S. Ghosh, Q. Liu, P. Mantilla-Perez, T. L. Chen, V. Mkhitaryan, M. Huang, S. Garner, J. Martorell, V. Pruneri, *Adv. Funct. Mater.* **2015**, *25*, 7309.

[92] R. A. Maniyara, V. K. Mkhitaryan, T. L. Chen, D. S. Ghosh, V. Pruneri, *Nat. Commun.* **2016**, *7*, 13771.

[93] P. C. Lansåker, J. Backholm, G. A. Niklasson, C. G. Granqvist, *Thin Solid Films* **2009**, *518*, 1225.

[94] W. Yu, L. Shen, F. Meng, Y. Long, S. Ruan, W. Chen, *Sol. Energy Mater. Sol. Cells* **2012**, *100*, 226.

[95] I. P. Lopez, L. Cattin, D. T. Nguyen, M. Morsli, J. C. Bernède, *Thin Solid Films* **2012**, *520*, 6419.

[96] N. P. Sergeant, A. Hadipour, B. Niesen, D. Cheyns, P. Heremans, P. Peumans, B. P. Rand, *Adv. Mater.* **2012**, *24*, 728.

[97] M. Ghasemi Varnamkhasti, H. R. Fallah, M. Mostajaboddavati, A. Hassanzadeh, *Vacuum* **2012**, *86*, 1318.

[98] S. Schubert, M. Hermenau, J. Meiss, L. Müller-Meskamp, K. Leo, *Adv. Funct. Mater.* **2012**, *22*, 4993.

[99] A. Dhar, T. L. Alford, *J. Appl. Phys.* **2012**, *112*, 103113.

[100] A. T. Barrows, R. Masters, A. J. Pearson, C. Rodenburg, D. G. Lidzey, *Sol. Energy Mater. Sol. Cells* **2016**, *144*, 600.

[101] J. F. Salinas, H. L. Yip, C. C. Chueh, C. Z. Li, J. L. Maldonado, A. K. Y. Jen, *Adv. Mater.* **2012**, *24*, 6362.

[102] H. Kermani, H. R. Fallah, M. Hajimahmoodzadeh, S. V. Tabatabaei, *Appl. Opt.* **2013**, *52*, 780.

[103] D. Y. Kim, Y. C. Han, H. C. Kim, E. G. Jeong, K. C. Choi, *Adv. Funct. Mater.* **2015**, *25*, 7145.

[104] Y. C. Han, M. S. Lim, J. H. Park, K. C. Choi, *Org. Electron.* **2013**, *14*, 3437.

[105] R. H. H. Ko, A. Khalatpour, J. K. D. Clark, N. P. Kherani, *APL Mater.* **2018**, *6*, 121112.

[106] M. Girtan, *Sol. Energy Mater. Sol. Cells* **2012**, *100*, 153.

[107] V. J. Logeeswaran, N. P. Kobayashi, M. S. Islam, W. Wu, P. Chaturvedi, N. X. Fang, S. Y. Wang, R. S. Williams, *Nano Lett.* **2009**, *9*, 178.

[108] W. Chen, K. P. Chen, M. D. Thoreson, A. V. Kildishev, V. M. Shalaev, *Appl. Phys. Lett.* **2010**, *97*, 211107.

[109] C. Cioarec, P. Melpignano, N. Gherardi, R. Clergereaux, C. Villeneuve, *Langmuir* **2011**, *27*, 3611.

[110] E. Jeong, G. Zhao, S. M. Yu, S.-G. Lee, J.-S. Bae, J. Park, J. Rha, G. H. Lee, J. Yun, *Appl. Surf. Sci.* **2020**, *528*, 146989.

[111] H. Liu, B. Wang, E. S. P. Leong, P. Yang, Y. Zong, G. Si, J. Teng, S. A. Maier, *ACS Nano* **2010**, *4*, 3139.

[112] T. Stefaniuk, P. Wróbel, P. Trautman, T. Szoplik, *Appl. Opt.* **2014**, *53*, B237.

[113] P. Melpignano, C. Cioarec, R. Clergereaux, N. Gherardi, C. Villeneuve, L. Datas, *Org. Electron.* **2010**, *11*, 1111.

[114] O. S. Heavens, *J. Phys. Radium* **1950**, *11*, 355.

[115] J. Meiss, M. K. Riede, K. Leo, *J. Appl. Phys.* **2009**, *105*, 063108.

[116] J. Meiss, M. K. Riede, K. Leo, *Appl. Phys. Lett.* **2009**, *94*, 013303.

[117] S. Schubert, J. Meiss, L. Müller-Meskamp, K. Leo, *Adv. Energy Mater.* **2013**, *3*, 438.

[118] T. Schwab, S. Schubert, L. Müller-Meskamp, K. Leo, M. C. Gather, *Adv. Opt. Mater.* **2013**, *1*, 921.

[119] N. Formica, D. S. Ghosh, A. Carrilero, T. L. Chen, R. E. Simpson, V. Pruneri, *ACS Appl. Mater. Interfaces* **2013**, *5*, 3048.

[120] C. Zhang, C. Pfeiffer, T. Jang, V. Ray, M. Junda, P. Uprety, N. Podraza, A. Grbic, L. J. Guo, *Laser Photonics Rev.* **2016**, *10*, 791.

[121] C. Pfeiffer, C. Zhang, V. Ray, L. J. Guo, A. Grbic, *Phys. Rev. Lett.* **2014**, *113*, 023902.

[122] G. Kästle, H. G. Boyen, B. Koslowski, A. Plettl, F. Weigl, P. Ziemann, *Surf. Sci.* **2002**, *498*, 168.

[123] D. P. Fromm, A. Sundaramurthy, P. J. Schuck, G. Kino, W. E. Moerner, *Nano Lett.* **2004**, *4*, 957.

[124] J. Zhang, D. M. Fryauf, M. Garrett, V. J. Logeeswaran, A. Sawabe, M. S. Islam, N. P. Kobayashi, *Langmuir* **2015**, *31*, 7852.

[125] M. Todeschini, A. Bastos da Silva Fanta, F. Jensen, J. B. Wagner, A. Han, *ACS Appl. Mater. Interfaces* **2017**, *9*, 37374.

[126] A. Ciesielski, L. Skowronski, E. Górecka, J. Kierdaszuk, T. Szoplik, *Beilstein J. Nanotechnol.* **2018**, *9*, 66.

[127] P. Wróbel, T. Stefaniuk, M. Trzcinski, A. A. Wronkowska, A. Wronkowski, T. Szoplik, *ACS Appl. Mater. Interfaces* **2015**, *7*, 8999.

[128] A. Poddubny, I. Iorsh, P. Belov, Y. Kivshar, *Nat. Photonics* **2013**, *7*, 948.

[129] P. Shekhar, J. Atkinson, Z. Jacob, *Nano Convergence* **2014**, *1*, 14.

[130] B. Lahiri, R. Dylewicz, R. M. De La Rue, N. P. Johnson, *Opt. Express* **2010**, *18*, 11202.

[131] P. Berini, *Adv. Opt. Photonics* **2009**, *1*, 484.

[132] S. A. Maier, *Plasmonics: Fundamentals and Applications*, Springer US, New York **2007**.

[133] S. J. Madsen, M. Esfandyarpour, M. L. Brongersma, R. Sinclair, *ACS Photonics* **2017**, *4*, 268.

[134] X. Jiao, J. Goeckeritz, S. Blair, M. Oldham, *Plasmonics* **2009**, *4*, 37.

[135] L. Ke, S. C. Lai, H. Liu, C. K. N. Peh, B. Wang, J. H. Teng, *ACS Appl. Mater. Interfaces* **2012**, *4*, 1247.

[136] H. Aouani, J. Wenger, D. Gérard, H. Rigneault, E. Devaux, T. W. Ebbesen, F. Mahdavi, T. Xu, S. Blair, *ACS Nano* **2009**, *3*, 2043.

[137] C. Zhang, N. Kinsey, L. Chen, C. Ji, M. Xu, M. Ferrera, X. Pan, V. M. Shalaev, A. Boltasseva, L. J. Guo, *Adv. Mater.* **2017**, *29*, 1605177.

**ADVANCED
SCIENCE NEWS**

www.advancedsciencenews.com

**ADVANCED
OPTICAL
MATERIALS**

www.advopticalmat.de

[138] D. Gu, C. Zhang, Y. K. Wu, L. J. Guo, *ACS Nano* **2014**, *8*, 10343.

[139] D. Zhao, C. Zhang, H. Kim, L. J. Guo, *Adv. Energy Mater.* **2015**, *5*, 1500768.

[140] C. Zhang, Q. Huang, Q. Cui, C. Ji, Z. Zhang, X. Chen, T. George, S. Zhao, L. J. Guo, *ACS Appl. Mater. Interfaces* **2019**, *11*, 27216.

[141] H. Han, Y. Zoo, J. W. Mayer, T. L. Alford, *J. Appl. Phys.* **2007**, *102*, 036101.

[142] B. Pattier, J. F. Bardeau, M. Edely, A. Gibaud, N. Delorme, *Langmuir* **2008**, *24*, 821.

[143] R. A. Hatton, M. R. Willis, M. A. Chesters, D. Briggs, *J. Mater. Chem.* **2003**, *13*, 722.

[144] A. Kossoy, V. Merk, D. Simakov, K. Leosson, S. Kéna-Cohen, S. A. Maier, *Adv. Opt. Mater.* **2015**, *3*, 71.

[145] L. Leandro, R. Malureanu, N. Rozlosnik, A. Lavrinenko, *ACS Appl. Mater. Interfaces* **2015**, *7*, 5797.

[146] H. M. Stec, R. J. Williams, T. S. Jones, R. A. Hatton, *Adv. Funct. Mater.* **2011**, *21*, 1709.

[147] H. M. Stec, R. A. Hatton, *ACS Appl. Mater. Interfaces* **2012**, *4*, 6013.

[148] J. Zou, C.-Z. Li, C.-Y. Chang, H. L. Yip, A. K. Y. Jen, *Adv. Mater.* **2014**, *26*, 3618.

[149] Y. G. Bi, J. Feng, J. H. Ji, Y. Chen, Y. S. Liu, Y. F. Li, Y. F. Liu, X. L. Zhang, H. B. Sun, *Nanoscale* **2016**, *8*, 10010.

[150] C. C. Chueh, S. C. Chien, H.-L. Yip, J. F. Salinas, C. Z. Li, K. S. Chen, F. C. Chen, W. C. Chen, A. K. Y. Jen, *Adv. Energy Mater.* **2013**, *3*, 417.

[151] H. Kang, S. Jung, S. Jeong, G. Kim, K. Lee, *Nat. Commun.* **2015**, *6*, 6503.

[152] R. C. O'Handley, D. K. Burge, S. N. Jasperson, E. J. Ashley, *Surf. Sci.* **1975**, *50*, 407.

[153] Z. M. Abd El-Fattah, V. Mkhitaryan, J. Brede, L. Fernández, C. Li, Q. Guo, A. Ghosh, A. R. Echarri, D. Naveh, F. Xia, J. E. Ortega, F. J. García de Abajo, *ACS Nano* **2019**, *13*, 7771.

[154] S. H. Lim, H. K. Kim, *Sci. Rep.* **2020**, *10*, 8357.

[155] A. L. D. Vecchio, F. Spaepen, *J. Appl. Phys.* **2007**, *101*, 063518.

[156] K. M. McPeak, S. V. Jayanti, S. J. P. Kress, S. Meyer, S. Iotti, A. Rossinelli, D. J. Norris, *ACS Photonics* **2015**, *2*, 326.

[157] H. Reddy, U. Guler, K. Chaudhuri, A. Dutta, A. V. Kildishev, V. M. Shalaev, A. Boltasseva, *ACS Photonics* **2017**, *4*, 1083.

[158] J. H. Park, P. Ambwani, M. Manno, N. C. Lindquist, P. Nagpal, S. H. Oh, C. Leighton, D. J. Norris, *Adv. Mater.* **2012**, *24*, 3988.

[159] A. A. Baski, H. Fuchs, *Surf. Sci.* **1994**, *313*, 275.

[160] T. C. Zhang, Z. X. Mei, Y. Guo, Q. K. Xue, X. L. Du, *J. Phys. D: Appl. Phys.* **2009**, *42*, 065303.

[161] W. Wang, M. Song, T. S. Bae, Y. H. Park, Y. C. Kang, S. G. Lee, S. Y. Kim, D. H. Kim, S. Lee, G. Min, G. H. Lee, J. W. Kang, J. Yun, *Adv. Funct. Mater.* **2014**, *24*, 1551.

[162] G. Zhao, W. Wang, T. S. Bae, S. G. Lee, C. Mun, S. Lee, H. Yu, G. H. Lee, M. Song, J. Yun, *Nat. Commun.* **2015**, *6*, 8830.

[163] G. Zhao, W. Shen, E. Jeong, S. G. Lee, S. M. Yu, T. S. Bae, G. H. Lee, S. Z. Han, J. Tang, E. A. Choi, J. Yun, *ACS Appl. Mater. Interfaces* **2018**, *10*, 27510.

[164] G. Zhao, S. M. Kim, S. G. Lee, T. S. Bae, C. Mun, S. Lee, H. Yu, G. H. Lee, H. S. Lee, M. Song, J. Yun, *Adv. Funct. Mater.* **2016**, *26*, 4180.

[165] J. I. Lee, S. M. Howard, J. J. Kellar, K. N. Han, W. Cross, *Metall. Mater. Trans. B* **2001**, *32*, 895.

[166] T. E. Graedel, *J. Electrochem. Soc.* **1992**, *139*, 1963.

[167] E. Ando, M. Miyazaki, *Thin Solid Films* **1999**, *351*, 308.

[168] E. Ando, S. Suzuki, N. Aomine, M. Miyazaki, M. Tada, *Vacuum* **2000**, *59*, 792.

[169] K. Thürmer, E. D. Williams, J. E. Reutt-Robey, *Phys. Rev. B* **2003**, *68*, 155423.

[170] H. Krishna, N. Shirato, C. Favazza, R. Kalyanaraman, *J. Mater. Res.* **2011**, *26*, 154.

[171] K. Aslan, Z. Leonenko, J. R. Lakowicz, C. D. Geddes, *J. Fluoresc.* **2005**, *15*, 643.

[172] S. Butun, K. Aydin, *ACS Photonics* **2015**, *2*, 1652.

[173] Y. Huo, S. W. Fu, Y. L. Chen, C. C. Lee, *J. Mater. Sci.: Mater. Electron.* **2016**, *27*, 10382.

[174] B. Barman, H. Dhasmana, A. Verma, A. Kumar, D. Singh, V. Jain, *Energy Environ.* **2018**, *29*, 358.

[175] Y. Wang, Y. Yang, Y. Sun, B. Quan, Y. Li, C. Gu, J. Li, *RSC Adv.* **2017**, *7*, 11578.

[176] Y. S. Jung, Y. W. Choi, H. C. Lee, D. W. Lee, *Thin Solid Films* **2003**, *440*, 278.

[177] J. C. Lin, J. Y. Chan, *Mater. Chem. Phys.* **1996**, *43*, 256.

[178] Z. Wang, X. Cai, Q. Chen, P. K. Chu, *Thin Solid Films* **2007**, *515*, 3146.

[179] G. Leftheriotis, S. Papaefthimiou, P. Yianoulis, *Solid State Ionics* **2000**, *136–137*, 655.

[180] W. Chen, M. D. Thoreson, S. Ishii, A. V. Kildishev, V. M. Shalaev, *Opt. Express* **2010**, *18*, 5124.

[181] S. W. Chen, C. Y. Bai, C. C. Jain, C. J. Zhan, C. H. Koo, *Mater. Trans.* **2007**, *48*, 2230.

[182] M. Boccas, T. Vucina, C. Araya, E. Vera, C. Ahhee, *Thin Solid Films* **2006**, *502*, 275.

[183] D. K. Burge, H. E. Bennett, E. J. Ashley, *Appl. Opt.* **1973**, *12*, 42.

[184] J. D. Barrie, P. D. Fuqua, K. A. Folgner, C. T. Chu, *Appl. Opt.* **2011**, *50*, C135.

[185] K. A. Folgner, C. T. Chu, Z. R. Lingley, H. I. Kim, J. M. Yang, J. D. Barrie, *Appl. Opt.* **2017**, *56*, C75.

[186] K. A. Folgner, C.-T. Chu, S. D. Sitzman, S. C. Stuart, Z. R. Lingley, J. D. Barrie, *Appl. Opt.* **2020**, *59*, A187.

[187] R. J. Martín-Palma, J. M. Martínez-Duart, *J. Vac. Sci. Technol., A* **1999**, *17*, 3449.

[188] R. J. Martín-Palma, L. Vázquez, J. M. Martínez-Duart, R. Malats, *Sol. Energy Mater. Sol. Cells* **1998**, *53*, 55.

[189] C. T. Chu, P. D. Fuqua, J. D. Barrie, *Appl. Opt.* **2006**, *45*, 1583.

[190] A. Ulman, *Chem. Rev.* **1996**, *96*, 1533.

[191] M. H. Schoenfisch, J. E. Pemberton, *J. Am. Chem. Soc.* **1998**, *120*, 4502.

[192] N. Fishelson, A. Inberg, N. Croitoru, Y. Shacham-Diamand, *Microelectron. Eng.* **2012**, *92*, 126.

[193] M. Evesque, M. Keddam, H. Takenouti, *Electrochim. Acta* **2004**, *49*, 2937.

[194] M. C. Bernard, E. Dauvergne, M. Evesque, M. Keddam, H. Takenouti, *Corros. Sci.* **2005**, *47*, 663.

[195] W. S. Beh, I. T. Kim, D. Qin, Y. Xia, G. M. Whitesides, *Adv. Mater.* **1999**, *11*, 1038.

[196] K. Zilberberg, T. Riedl, *J. Mater. Chem. A* **2016**, *4*, 14481.

[197] S. Kim, J. L. Lee, *J. Photonics Energy* **2012**, *2*, 021215.

[198] J. Ham, S. Kim, G. H. Jung, W. J. Dong, J. L. Lee, *J. Mater. Chem. A* **2013**, *1*, 3076.

[199] M. Bauch, T. Dimopoulos, *Mater. Des.* **2016**, *104*, 37.

[200] L. Kinner, M. Bauch, R. A. Wibowo, G. Ligorio, E. J. W. List-Kratochvil, T. Dimopoulos, *Mater. Des.* **2019**, *168*, 107663.

[201] C. Guillén, J. Herrero, *Thin Solid Films* **2011**, *520*, 1.

[202] H. Wang, C. Ji, C. Zhang, Y. Zhang, Z. Zhang, Z. Lu, J. Tan, L. J. Guo, *ACS Appl. Mater. Interfaces* **2019**, *11*, 11782.

[203] C. Zhang, H. J. Lezec, W. Zhu, A. Agrawal, in *Imaging and Applied Optics 2018*, The Optical Society, Orlando, FL **2018**, paper ATh2A.4.

[204] H. A. Macleod, *Thin-Film Optical Filters*, 3rd ed., CRC Press, Boca Raton, FL **2001**.

[205] K. T. Lee, C. Ji, D. Banerjee, L. J. Guo, *Laser Photonics Rev.* **2015**, *9*, 354.

[206] C. Ji, K. T. Lee, L. J. Guo, *Opt. Lett.* **2019**, *44*, 86.

[207] C. Ji, Z. Zhang, T. Masuda, Y. Kudo, L. J. Guo, *Nanoscale Horiz.* **2019**, *4*, 874.

[208] C. Yang, C. Ji, W. Shen, K.-T. Lee, Y. Zhang, X. Liu, L. J. Guo, *ACS Photonics* **2016**, *3*, 590.

ADVANCED
SCIENCE NEWS

www.advancedsciencenews.com

ADVANCED
OPTICAL
MATERIALS

www.advopticalmat.de

[209] G. K. Dalapati, A. K. Kushwaha, M. Sharma, V. Suresh, S. Shannigrahi, S. Zhuk, S. Masudy-Panah, *Prog. Mater. Sci.* **2018**, *95*, 42.

[210] C. Ji, D. Liu, C. Zhang, L. J. Guo, *Nat. Commun.* **2020**, *11*, 3367.

[211] P. Huo, C. Zhang, W. Zhu, M. Liu, S. Zhang, S. Zhang, L. Chen, H. J. Lezec, A. Agrawal, Y. Lu, T. Xu, *Nano Lett.* **2020**, *20*, 2791.

[212] C. Zhang, S. Divitt, Q. Fan, W. Zhu, A. Agrawal, Y. Lu, T. Xu, H. J. Lezec, *Light: Sci. Appl.* **2020**, *9*, 55.

[213] K. Hong, J. H. Son, S. Kim, B. H. Koo, J.-L. Lee, *Chem. Commun.* **2012**, *48*, 10606.

[214] M. Kaltenbrunner, M. S. White, E. D. Głowacki, T. Sekitani, T. Someya, N. S. Sariciftci, S. Bauer, *Nat. Commun.* **2012**, *3*, 770.

[215] G. Li, R. Zhu, Y. Yang, *Nat. Photonics* **2012**, *6*, 153.

[216] F. C. Krebs, *Sol. Energy Mater. Sol. Cells* **2009**, *93*, 1636.

[217] C. J. Brabec, S. Gowrisanker, J. J. M. Halls, D. Laird, S. Jia, S. P. Williams, *Adv. Mater.* **2010**, *22*, 3839.

[218] X. W. Sun, D. W. Zhao, L. Ke, A. K. K. Kyaw, G. Q. Lo, D. L. Kwong, *Appl. Phys. Lett.* **2010**, *97*, 053303.

[219] D. W. Zhao, P. Liu, X. W. Sun, S. T. Tan, L. Ke, A. K. K. Kyaw, *Appl. Phys. Lett.* **2009**, *95*, 153304.

[220] A. J. Heeger, *Adv. Mater.* **2014**, *26*, 10.

[221] C. E. Small, S. Chen, J. Subbiah, C. M. Amb, S. W. Tsang, T. H. Lai, J. R. Reynolds, F. So, *Nat. Photonics* **2012**, *6*, 115.

[222] Y. Li, G. Xu, C. Cui, Y. Li, *Adv. Energy Mater.* **2018**, *8*, 1701791.

[223] Z. Wang, C. Zhang, R. Gao, D. Chen, S. Tang, J. Zhang, D. Wang, X. Lu, Y. Hao, *Sol. Energy Mater. Sol. Cells* **2014**, *127*, 193.

[224] D. Zhao, C. Chen, C. Wang, M. M. Junda, Z. Song, C. R. Grice, Y. Yu, C. Li, B. Subedi, N. J. Podraza, X. Zhao, G. Fang, R.-G. Xiong, K. Zhu, Y. Yan, *Nat. Energy* **2018**, *3*, 1093.

[225] A. K. Jena, A. Kulkarni, T. Miyasaka, *Chem. Rev.* **2019**, *119*, 3036.

[226] S. Jiang, Y. Sheng, Y. Hu, Y. Rong, A. Mei, H. Han, *Front. Optoelectron.* **2020**, *13*, 256.

[227] Y. Rong, Y. Hu, A. Mei, H. Tan, M. I. Saidaminov, S. I. Seok, M. D. McGehee, E. H. Sargent, H. Han, *Science* **2018**, *361*, eaat8235.

[228] J. P. Correa-Baena, M. Saliba, T. Buonassisi, M. Grätzel, A. Abate, W. Tress, A. Hagfeldt, *Science* **2017**, *358*, 739.

[229] A. Ren, H. Lai, X. Hao, Z. Tang, H. Xu, B. M. F. Yu Jeco, K. Watanabe, L. Wu, J. Zhang, M. Sugiyama, J. Wu, D. Zhao, *Joule* **2020**, *4*, 1263.

[230] P. K. Nayak, S. Mahesh, H. J. Snaith, D. Cahen, *Nat. Rev. Mater.* **2019**, *4*, 269.

[231] T. Leijtens, K. A. Bush, R. Prasanna, M. D. McGehee, *Nat. Energy* **2018**, *3*, 828.

[232] H. J. Snaith, P. Hacke, *Nat. Energy* **2018**, *3*, 459.

[233] Z. Li, T. R. Klein, D. H. Kim, M. Yang, J. J. Berry, M. F. A. M. van Hest, K. Zhu, *Nat. Rev. Mater.* **2018**, *3*, 18017.

[234] H. Yang, Y. Liu, Y. Dou, J. Zhang, Z. Wu, Q. Zhang, Y.-B. Cheng, J. Zhong, *Front. Optoelectron.* **2020**, *13*, 272.

[235] C. Y. Chang, Y. C. Chang, W. K. Huang, W. C. Liao, H. Wang, C. Yeh, B. C. Tsai, Y. C. Huang, C. S. Tsao, *J. Mater. Chem. A* **2016**, *4*, 7903.

[236] C. Hanmandlu, C. C. Liu, C. Y. Chen, K. M. Boopathi, S. H. Wu, M. Singh, A. Mohapatra, H. W. Lin, Y. C. Chang, Y. C. Chang, C. S. Lai, C. W. Chu, *ACS Appl. Mater. Interfaces* **2018**, *10*, 17973.

[237] M. Xu, J. Feng, Z.-J. Fan, X.-L. Ou, Z.-Y. Zhang, H. Y. Wang, H.-B. Sun, *Sol. Energy Mater. Sol. Cells* **2017**, *169*, 8.

[238] J. Zhao, K. O. Brinkmann, T. Hu, N. Pourdavoud, T. Becker, T. Gahlmann, R. Heiderhoff, A. Polywka, P. Görrn, Y. Chen, B. Cheng, T. Riedl, *Adv. Energy Mater.* **2017**, *7*, 1602599.

[239] X. L. Ou, M. Xu, J. Feng, H. B. Sun, *Sol. Energy Mater. Sol. Cells* **2016**, *157*, 660.

[240] E. D. Gaspera, Y. Peng, Q. Hou, L. Spiccia, U. Bach, J. J. Jasieniak, Y.-B. Cheng, *Nano Energy* **2015**, *13*, 249.

[241] M. A. Green, S. Pillai, *Nat. Photonics* **2012**, *6*, 130.

[242] H. A. Atwater, A. Polman, *Nat. Mater.* **2010**, *9*, 205.

[243] L. Müller-Meskamp, Y. H. Kim, T. Roch, S. Hofmann, R. Scholz, S. Eckardt, K. Leo, A. F. Lasagni, *Adv. Mater.* **2012**, *24*, 906.

[244] X. Li, W. C. H. Choy, L. Huo, F. Xie, W. E. I. Sha, B. Ding, X. Guo, Y. Li, J. Hou, J. You, Y. Yang, *Adv. Mater.* **2012**, *24*, 3046.

[245] Q. Gan, F. J. Bartoli, Z. H. Kafafi, *Adv. Mater.* **2013**, *25*, 2385.

[246] H. W. Chen, J. H. Lee, B. Y. Lin, S. Chen, S. T. Wu, *Light: Sci. Appl.* **2018**, *7*, 17168.

[247] S. J. Zou, Y. Shen, F. M. Xie, J. D. Chen, Y. Q. Li, J. X. Tang, *Mater. Chem. Front.* **2020**, *4*, 788.

[248] S. Choi, C. M. Kang, C. W. Byun, H. Cho, B. H. Kwon, J. H. Han, J. H. Yang, J. W. Shin, C. S. Hwang, N. S. Cho, K. M. Lee, H.-O. Kim, E. Kim, S. Yoo, H. Lee, *Nat. Commun.* **2020**, *11*, 2732.

[249] F. So, J. Kido, P. Burrows, *MRS Bull.* **2008**, *33*, 663.

[250] S. R. Forrest, *Nature* **2004**, *428*, 911.

[251] B. W. D'Andrade, S. R. Forrest, *Adv. Mater.* **2004**, *16*, 1585.

[252] T. Yokota, P. Zalar, M. Kaltenbrunner, H. Jinno, N. Matsuhisa, H. Kitanosako, Y. Tachibana, W. Yukita, M. Koizumi, T. Someya, *Sci. Adv.* **2016**, *2*, e1501856.

[253] Y. Lee, J. Y. Oh, W. Xu, O. Kim, T. R. Kim, J. Kang, Y. Kim, D. Son, J. B. H. Tok, M. J. Park, Z. Bao, T. W. Lee, *Sci. Adv.* **2018**, *4*, eaat7387.

[254] M. Choi, S. R. Bae, L. Hu, A. T. Hoang, S. Y. Kim, J. H. Ahn, *Sci. Adv.* **2020**, *6*, eabb5898.

[255] M. Choi, Y. J. Park, B. K. Sharma, S. R. Bae, S. Y. Kim, J. H. Ahn, *Sci. Adv.* **2018**, *4*, eaas8721.

[256] D. Zhang, T. Huang, L. Duan, *Adv. Mater.* **2020**, *32*, 1902391.

[257] S. Ding, J. Jiu, Y. Gao, Y. Tian, T. Araki, T. Sugahara, S. Nagao, M. Nogi, H. Koga, K. Suganuma, H. Uchida, *ACS Appl. Mater. Interfaces* **2016**, *8*, 6190.

[258] T. H. Han, Y. Lee, M. R. Choi, S. H. Woo, S. H. Bae, B. H. Hong, J. H. Ahn, T. W. Lee, *Nat. Photonics* **2012**, *6*, 105.

[259] Q. He, S. Wu, S. Gao, X. Cao, Z. Yin, H. Li, P. Chen, H. Zhang, *ACS Nano* **2011**, *5*, 5038.

[260] Y. Xia, K. Sun, J. Ouyang, *Adv. Mater.* **2012**, *24*, 2436.

[261] P. Hojati-Talemi, C. Bächler, M. Fabretto, P. Murphy, D. Evans, *ACS Appl. Mater. Interfaces* **2013**, *5*, 11654.

[262] S. Cheylan, D. S. Ghosh, D. Krautz, T. L. Chen, V. Pruneri, *Org. Electron.* **2011**, *12*, 818.

[263] W. Brütting, J. Frischeisen, T. D. Schmidt, B. J. Scholz, C. Mayr, *Phys. Status Solidi A* **2013**, *210*, 44.

[264] S. Mladenovski, K. Neyts, D. Pavicic, A. Werner, C. Rothe, *Opt. Express* **2009**, *17*, 7562.

[265] T. W. Koh, J. M. Choi, S. Lee, S. Yoo, *Adv. Mater.* **2010**, *22*, 1849.

[266] Y. R. Do, Y. C. Kim, Y. W. Song, C. O. Cho, H. Jeon, Y. J. Lee, S. H. Kim, Y. H. Lee, *Adv. Mater.* **2003**, *15*, 1214.

[267] Y. Qu, M. Slootsky, S. R. Forrest, *Nat. Photonics* **2015**, *9*, 758.

[268] H. W. Chang, J. Lee, S. Hofmann, Y. H. Kim, L. Müller-Meskamp, B. Lüssem, C. C. Wu, K. Leo, M. C. Gather, *J. Appl. Phys.* **2013**, *113*, 204502.

[269] X. Yang, K. Dev, J. Wang, E. Mutlugun, C. Dang, Y. Zhao, S. Liu, Y. Tang, S. T. Tan, X. W. Sun, H. V. Demir, *Adv. Funct. Mater.* **2014**, *24*, 5977.

[270] W. H. Koo, S. M. Jeong, F. Araoka, K. Ishikawa, S. Nishimura, T. Toyooka, H. Takezoe, *Nat. Photonics* **2010**, *4*, 222.

[271] M. Thomschke, S. Reineke, B. Lüssem, K. Leo, *Nano Lett.* **2012**, *12*, 424.

[272] T. W. Koh, J. A. Spechler, K. M. Lee, C. B. Arnold, B. P. Rand, *ACS Photonics* **2015**, *2*, 1366.

[273] L. H. Xu, Q. D. Ou, Y. Q. Li, Y. B. Zhang, X. D. Zhao, H. Y. Xiang, J. D. Chen, L. Zhou, S. T. Lee, J. X. Tang, *ACS Nano* **2016**, *10*, 1625.

[274] Z. B. Wang, M. G. Helander, J. Qiu, D. P. Puzzo, M. T. Greiner, Z. M. Hudson, S. Wang, Z. W. Liu, Z. H. Lu, *Nat. Photonics* **2011**, *5*, 753.

[275] S. Lenk, T. Schwab, S. Schubert, L. Müller-Meskamp, K. Leo, M. C. Gather, S. Reineke, *Appl. Phys. Lett.* **2015**, *107*, 163302.

**ADVANCED
SCIENCE NEWS**

www.advancedsciencenews.com

**ADVANCED
OPTICAL
MATERIALS**

www.advopticalmat.de

[276] J. Liang, X. Guo, L. Song, J. Lin, Y. Hu, N. Zhang, X. Liu, *Appl. Phys. Lett.* **2017**, *111*, 213301.

[277] Z. Li, S. Butun, K. Aydin, *ACS Photonics* **2015**, *2*, 183.

[278] Y. T. Yoon, S. S. Lee, *Opt. Express* **2010**, *18*, 5344.

[279] C. S. Park, V. R. Shrestha, S. S. Lee, E. S. Kim, D. Y. Choi, *Sci. Rep.* **2015**, *5*, 8467.

[280] C. S. Park, V. R. Shrestha, S. S. Lee, D. Y. Choi, *Sci. Rep.* **2016**, *6*, 25496.

[281] J. H. Han, D. Y. Kim, D. Kim, K. C. Choi, *Sci. Rep.* **2016**, *6*, 29341.

[282] C. Ji, S. Acharya, K. Yamada, S. Maldonado, L. J. Guo, *ACS Appl. Mater. Interfaces* **2019**, *11*, 29065.

[283] C. Ji, C. Yang, W. Shen, K.-T. Lee, Y. Zhang, X. Liu, L. J. Guo, *Nano Res.* **2019**, *12*, 543.

[284] C. Ji, K. T. Lee, T. Xu, J. Zhou, H. J. Park, L. J. Guo, *Adv. Opt. Mater.* **2017**, *5*, 1700368.

[285] J. H. Lu, Y. L. Yu, S. R. Chuang, C. H. Yeh, C. P. Chen, *J. Phys. Chem. C* **2016**, *120*, 4233.

[286] J. H. Lu, Y. H. Lin, B. H. Jiang, C. H. Yeh, J. C. Kao, C. P. Chen, *Adv. Funct. Mater.* **2017**, *28*, 1703398.

[287] Y. H. Chen, C. W. Chen, Z. Y. Huang, W. C. Lin, L. Y. Lin, F. Lin, K. T. Wong, H. W. Lin, *Adv. Mater.* **2014**, *26*, 1129.

[288] Y. Li, C. Ji, Y. Qu, X. Huang, S. Hou, C.-Z. Li, L.-S. Liao, L. J. Guo, S. R. Forrest, *Adv. Mater.* **2019**, *31*, 1903173.

[289] Q. Tai, F. Yan, *Adv. Mater.* **2017**, *29*, 1700192.

[290] J. H. Han, D. Kim, T.-W. Lee, E. G. Jeong, H. S. Lee, K. C. Choi, *ACS Photonics* **2018**, *5*, 1891.

[291] A. A. F. Husain, W. Z. W. Hasan, S. Shafie, M. N. Hamidon, S. S. Pandey, *Renewable Sustainable Energy Rev.* **2018**, *94*, 779.

[292] J. Sun, J. J. Jasieniak, *J. Phys. D: Appl. Phys.* **2017**, *50*, 093001.

[293] J. Y. Lee, K. T. Lee, S. Seo, L. J. Guo, *Sci. Rep.* **2014**, *4*, 4192.

[294] J. Lee, S. Hofmann, M. Thomschke, M. Furno, Y. H. Kim, B. Lüssem, K. Leo, *Appl. Phys. Lett.* **2011**, *99*, 073303.

[295] J. Lee, H. Cho, T.-W. Koh, C. Yun, S. Hofmann, J. H. Lee, Y. H. Kim, B. Lüssem, J.-I. Lee, K. Leo, M. C. Gather, S. Yoo, *Opt. Express* **2013**, *21*, 28040.

[296] W. H. Choi, H. L. Tam, D. Ma, F. Zhu, *Opt. Express* **2015**, *23*, A471.

[297] I. Lee, S. Kim, J. Y. Park, S. Kim, H. W. Cho, J. Ham, S. Gim, K. Kim, K. Hong, J. Lee, *IEEE Photonics J.* **2018**, *10*, 1.

[298] S. S. Kanu, R. Binions, *Proc. R. Soc. A* **2010**, *466*, 19.

[299] G.-L. Chen, *US7826704B2*, **2010**.

[300] T. Gao, B. P. Jelle, *Transl. Mater. Res.* **2017**, *4*, 015001.

[301] K. W. Hartig, S. L. Larson, P. J. Lingle, *US5557462A*, **1996**.

[302] R. J. Martín-Palma, R. Gago, M. Vinnichenko, J. M. Martínez-Duart, *J. Phys. D: Appl. Phys.* **2004**, *37*, 1554.

[303] E. Hagen, H. Rubens, *Ann. Phys.* **1903**, *316*, 873.

[304] R. E. Hummel, *Electronic Properties of Materials*, Springer, New York, NY **2011**.

[305] L. Kheifets, A. A. Afifi, R. Shimkhada, *Environ. Health Perspect.* **2006**, *114*, 1532.

[306] S. Szmigielski, *Sci. Total Environ.* **1996**, *180*, 9.

[307] F. Shahzad, M. Alhabeb, C. B. Hatter, B. Anasori, S. M. Hong, C. M. Koo, Y. Gogotsi, *Science* **2016**, *353*, 1137.

[308] O. Balci, E. O. Polat, N. Kakenov, C. Kocabas, *Nat. Commun.* **2015**, *6*, 6628.

[309] Z. Zeng, H. Jin, M. Chen, W. Li, L. Zhou, Z. Zhang, *Adv. Funct. Mater.* **2016**, *26*, 303.

[310] S. K. Hong, K. Y. Kim, T. Y. Kim, J. H. Kim, S. W. Park, J. H. Kim, B. J. Cho, *Nanotechnology* **2012**, *23*, 455704.

[311] S. Kim, J. S. Oh, M. G. Kim, W. Jang, M. Wang, Y. Kim, H. W. Seo, Y. C. Kim, J. H. Lee, Y. Lee, J. D. Nam, *ACS Appl. Mater. Interfaces* **2014**, *6*, 17647.

[312] Y. Wu, Z. Wang, X. Liu, X. Shen, Q. Zheng, Q. Xue, J. K. Kim, *ACS Appl. Mater. Interfaces* **2017**, *9*, 9059.

[313] W. Wang, Q. Zhou, K. Ni, H. Lin, *Opt. Mater. Express* **2018**, *8*, 3485.

[314] M. Hu, J. Gao, Y. Dong, K. Li, G. Shan, S. Yang, R. K.-Y. Li, *Langmuir* **2012**, *28*, 7101.

[315] J. Gu, S. Hu, H. Ji, H. Feng, W. Zhao, J. Wei, M. Li, *Nanotechnology* **2020**, *31*, 185303.

[316] H. Wang, Y. Zhang, C. Ji, C. Zhang, D. Liu, Z. Zhang, Z. Lu, J. Tan, L. J. Guo, *Adv. Sci.* **2019**, *6*, 1901320.

Cheng Zhang obtained his B.S. degree in Electrical Science and Technology from the Shandong University (China) in 2010, and Ph.D. degree in Electrical Engineering from the University of Michigan, Ann Arbor (USA) in 2016. From 2016 to 2019, he worked as a postdoctoral researcher at the National Institute of Standards and Technology (USA). He is currently a professor at the Huazhong University of Science and Technology (China), and leads a research team working on cutting-edge projects aimed at the exploitation of nanophotonic materials, devices, and fabrication techniques for novel imaging, sensing, and optical signal processing applications.

Chengang Ji received his B.S. degree in Optical Information Science and Technology from the Beijing Jiaotong University, China in 2013 and the Ph.D. degree in Electrical Engineering from the University of Michigan, Ann Arbor in 2019. He is now a chief technology officer of a startup in China. His research interests include nano- and microphotonics, plasmonics, and optoelectronics.

Yong-Bum Park received his Ph.D. degree in the Department of Electrical Engineering at the University of Michigan, Ann Arbor (USA) in 2020. His research interest includes flexible transparent conductors for large-area optoelectronic devices like organic light-emitting diodes and photodetectors. He is currently a postdoctoral research fellow at the University of Michigan.

L. Jay Guo started his academic career at the University of Michigan in 1999, and has been a full professor of Electrical Engineering and Computer Science since 2011, and also affiliated with the Applied Physics, Mechanical Engineering, Macromolecular Science and Engineering. He directs an interdisciplinary laboratory at the intersection of electrical engineering, photonics, polymer materials, and mechanical engineering. His group's research includes polymer-based photonic devices and sensor applications, organic and hybrid photovoltaics and photodetectors, structural colors and nanophotonics, nanoimprint-based and roll-to-roll nanomanufacturing technologies.